

Modelling and Contact Analysis of Planetary Exploration Rovers

Sadhbh MacMahon

Master of Engineering

Mechanical Engineering

McGill University

Montréal, Québec

April 2016

A thesis submitted to McGill University in partial fulfillment of the requirements of the degree of
Master of Engineering

©Sadhbh MacMahon, 2016

Dedicated to the loving memory of Enda Breffní Doyle

ACKNOWLEDGMENTS

Throughout the progress of this research, several groups and individuals have given support along the way, for which I am truly grateful. First of all I would like to thank the members of my team in the Applied Dynamics Group at McGill: Qing Feng Lou, Dr. Bahareh Ghotbi, and Dr. Francisco González Varela, for their continual support and assistance. I consider myself lucky to have worked with such an excellent team. Additionally Professors Angeles and Zsombor-Murray gave input and advice which was much appreciated. The role played by MacDonald Dettwiler and Associates in financial support of the research and in facilitating experimental analysis, is gratefully acknowledged. Also, the experiments were considerably enhanced with the help of several technical product and special effects shops associated with the Toronto film industry: Walter Klassen FX, Laird FX, Dwight Crane Ltd, and ACME FX, who supplied us with equipment, machined parts and machining time at their shops. A particular mention with respect to executing the experiments, goes to James McFall, for his inspiration and excellent mechanical advice. I would like to thank my brothers and my father for their support and encouragement along the way. Finally, I would like to thank my supervisor Prof. József Kövecses, who made all this possible.

ABSTRACT

Autonomous navigation is a requirement of any planetary exploration rover moving in an environment too far from Earth for efficient communication between the rover and ground control. An important feature of this autonomy is the ability of the rover to successfully negotiate obstacles that may lie in its chosen path. To accommodate this need, planetary rovers are furnished with many actively actuated or passive degrees of freedom to influence the rover configuration, and in turn, the wheel-terrain contact forces that propel the rover forth. Analysis of these contact forces can be performed with a number of tools and with a variety of methods. Most of these methods however, depend on the use of parameters which can only be ascertained with detailed knowledge of the geometry, and constitutive properties of the terrain. This can produce considerable difficulty for the analysis of systems operating in unknown or unfamiliar environments. In this thesis a performance indicator known as the “effective kinetic energy of impact”, is explored for use in planetary rover operations. The effective kinetic energy is an indicator of how system configuration at the onset of an impact, will affect the resulting contact and impact forces. This indicator requires no knowledge of constitutive properties of the system. The indicator is discussed and developed for use with a model of an existing planetary rover prototype. Simulations with the rover model are used to compare the effective kinetic energy indicator with a more traditional, continuous force model method of evaluating contact force, and to demonstrate the similar trend between the two where contact configuration is concerned. These simulations are validated experimentally with the physical model of the rover engaging in a series of impacts with an obstacle, where the configuration is systematically varied. The experimental results are discussed, and a direction for future work and experimental validation are considered.

RÉSUMÉ

La navigation autonome est essentielle à tout véhicule d'exploration planétaire se déplaçant dans un environnement trop éloigné de la Terre pour qu'une communication efficace soit possible entre le rover et le contrôle au sol. Une caractéristique déterminante de son autonomie réside donc dans l'habileté du rover à négocier avec succès les obstacles qui pourraient se trouver sur son chemin. Pour ce faire, les véhicules d'exploration planétaires sont dotés de maints degrés de liberté déclenchés activement ou passifs, qui ont une influence sur la configuration du véhicule et, par conséquent, les forces de contact roues-terrain qui propulsent le rover vers l'avant. Pour analyser ces forces de contact, il est possible de recourir à une variété d'outils et de méthodes. Cependant, la plupart de ces méthodes dépendent de l'usage de paramètres qui ne peuvent être déterminés que par la connaissance approfondie de la géométrie et des propriétés constitutives du terrain. Il peut ainsi s'avérer considérablement difficile de procéder à l'analyse de systèmes en opération dans des environnements inconnus. Le présent mémoire examine l'indicateur de performance appelé « énergie cinétique effective de l'impact » dans le contexte des opérations de véhicules d'exploration planétaire. Cet indicateur mesure l'effet de la configuration des systèmes des véhicules sur les forces exercées sur ces derniers au moment d'un impact. L'indicateur ne nécessite aucune connaissance des propriétés constitutives du système. Le mémoire porte sur l'indicateur et son développement en vue d'un usage sur un prototype de véhicule d'exploration planétaire déjà existant. Des simulations à l'aide du rover modèle permettent de comparer l'indicateur d'énergie cinétique effective à une méthode modèle de force continue d'évaluation de la force de contact plus traditionnelle, et de démontrer la tendance similaire entre les deux, lorsqu'il est question de configuration des contacts. Les simulations sont validées de manière expérimentale à l'aide d'un modèle physique de rover subissant une série d'impacts contre des obstacles, dans un contexte où l'on fait varier systématiquement la configuration. Les résultats expérimentaux seront analysés et une orientation quant aux travaux futurs et à la validation expérimentale est envisagée.

TABLE OF CONTENTS

	ii
	ACKNOWLEDGMENTS	iii
	ABSTRACT	iv
	RÉSUMÉ	v
	LIST OF TABLES	viii
	LIST OF FIGURES	ix
1	Introduction	1
2	Background and Literature Review	3
	2.1 Contact Force Analysis with Planetary Rovers	3
	2.2 Contact Background and Modelling Methods	9
	2.3 The Effective Kinetic Energy of an Impact	11
3	Introduction To Effective Kinetic Energy	14
4	Simulations with the McGill Generic Multibody Dynamics Library (GMDL)	26
	4.1 Rover Chassis Prototype (RCP)	30
	4.2 The Parametric Rover	32
	4.3 The ExoMars-Like Rover	34
5	Impact Simulations	42
	5.1 Contact Models	42
	5.2 Impact Simulations	48
	5.3 The Evaluation of Effective Kinetic Energy	51
	5.4 Modelling the Ground	56
	5.5 Simulation Results	60
6	Experiments	67
	6.1 Design of an Actuator System for Control of Normal Force Distribution	67
	6.2 Impact Experiments	72
	6.2.1 Choice of Sensor Location	73
	6.2.2 Choice of Sensors	74
	6.2.3 Construction of the Intelligent Obstacles	80

6.2.4	Impact set-up and procedure	83
6.2.5	Experimental Results	84
6.2.6	Discussion and Considerations	89
6.2.7	Modelling Grousers	91
7	Conclusions	99
7.1	Future Work	101
	References	102
	Appendices	109
A	Two-Body Calculations	110
B	Parametrizations For Effective Kinetic Energy	114
C	CAD Drawings and Force Calculations for Experimental Equipment	119
C.1	Proposed Modifications for Mounting the RCP Redundant Actuators	119
C.2	Force Analysis of Rear Mounted Sensors	119
C.3	Intelligent Obstacle Design and Future Use	122
D	Impact Experiments with an RCP bumper	125
D.1	Construction of the Bumper	125
D.2	Experimental Set-up	127
D.3	Experimental Results	128

LIST OF TABLES

<u>Table</u>		<u>page</u>
4-1	Parametrization of the RCP rover.	34
4-2	ExoMars-like rover component groups.	38
6-1	Comparison of sensor mounting locations on the intelligent obstacles.	74
C-1	Sensor rear mount parameters dependent on angle of impact plane.	121
D-1	Components of the impact bumpers.	126

LIST OF FIGURES

<u>Figure</u>	<u>page</u>
3-1 Two-dimensional model of a rover.	14
3-2 Two-mass simplification of two-dimensional rover	15
3-3 Two-mass system with normal and tangential impact coordinates.	18
3-4 Two-mass system impacting a surface with different positions of the chassis CoM.	25
4-1 Models of the RCP.	31
4-2 A selection of possible input parameters for the parametric rover	33
4-3 Components of the BEMA subassembly.	35
4-4 ExoMars rear bogie assembly.	36
4-5 McGill model of an “ExoMars-like” like rover.	37
4-6 McGill models of ExoMars-like rover parts.	38
4-7 McGill solid model of the ELR with focus on the leg assembly.	39
4-8 Illustration of transformation from Solid Works to GMDL frames.	40
5-1 Diagram of collision of bodies i and j.	42
5-2 Data flow through a typical multibody dynamics simulation using the GMDL library functions.	47
5-3 RCP Impact Simulation.	48
5-4 Contact detection.	50
5-5 Front wheel contact point reference frame.	53
5-6 A schematic representation of the SCM, RCP Jacobian.	55
5-7 Illustration of the wheel-terrain constraints for a rolling body.	56
5-8 Simulation results for impact with RCP and ELR models	61
5-9 Impact simulation results with various contact force models, and coefficients of restitution.	62
5-10 Impact simulation results with a kinematic model of the terrain.	64

5-11	Constrained directions of motion of a wheel upon impact.	65
5-12	Impact simulations with constitutive contact models of the terrain.	66
6-1	Drawings of the proposed redundant actuator assembly.	69
6-2	Redundant actuator system components.	71
6-3	The intelligent obstacles	73
6-4	Deformation from loads applied to the RCP leg.	78
6-5	CAD model of the intelligent obstacle.	80
6-6	Impact experiments.	82
6-7	Typical soft soil impact trial	83
6-8	Ideal three sensor impact curve.	85
6-9	Sample data for impact at 60°	86
6-10	Effect of friction on the angle of the contact force.	88
6-11	Experimental results.	90
6-12	Impact with grousers.	92
6-13	Contact force sensitivity to location of impact.	93
6-14	Evaluating the degree of penetration with multiple grouser contacts.	94
6-15	Impact simulations with varied grouser configurations.	96
A-1	Two-mass rover system in an impact with a flat surface.	110
A-2	Evaluating the position of the contact point C	112
C-1	Modifications to the RCP to accommodate redundant actuators.	119
C-2	Obstacle with rear mounted sensors.	120
C-3	Force analysis of impact transmitted to rear mounted sensors.	120
C-4	Intelligent Obstacle CAD drawings	122
C-5	Horizontal and step-down obstacle configurations.	123
C-6	Slope climbing obstacle configuration.	124
D-1	CAD model of bumper assembled on RCP wheel	125
D-2	Exploded view and part list of bumper model	126

D-3 Photographs of the bumpers constructed and assembled on the RCP wheel. 128

CHAPTER 1

Introduction

This thesis explores a relatively new performance indicator for impact and contact analysis of dynamic multibody systems. Past research has established this indicator, known as the effective kinetic energy of impact, as an indicator of the relationship between contact force and system configuration in a contact or impact scenario. The work in this thesis continues this development with specific applications to planetary exploration rovers. While simulations and experimental analysis discussed in this research deal mostly with impact, the work is intended to lay the foundation for extension of the indicator to analysis of obstacle negotiation and to assist with general rover mobility in unstructured terrain. The research is outlined as follows:

Chapter 2: The background and a literature survey on three topics are presented: i) the use of contact force analysis for obstacle climbing in planetary rovers, ii) some traditional methods of general contact analysis, and iii) background on the kinetic energy performance indicator itself.

Chapter 3: An introduction to effective kinetic energy is given. An example with a simple two-body system is used to show how the choice of coordinates of the system leads to development of the effective kinetic energy term. The example is applied to situations which aid in a conceptual understanding of the effective kinetic energy of a system.

Chapter 4: The platform used - the McGill Generic Multibody Dynamics Library Code (GMDL)- for simulations with a planetary rover model - the Rover Chassis Prototype (RCP) - are explained. An adaptation of the RCP model to a parametric model more suited to the simulations involving changes in system position and geometry is discussed. Details of how this adapted model was used to develop an ExoMars-like rover in preparation for the ExoMars 2018 expedition are outlined.

Chapter 5: The background on several continuous force contact models used in impact simulations with the rover models are discussed. The details of a typical impact simulation with the software are outlined. Some of the particular challenges to modelling impact and using the effective kinetic

energy performance indicator are outlined and finally the results of the simulations are presented and discussed.

Chapter 6: The experimental set-up and procedure is explained. The results of the experiments and some of the difficulties encountered in the results due to differences in the experimental and simulation set-ups are discussed. Modelling considerations regarding the simulations that reduce some of these differences are described.

Chapter 7: Conclusions of the thesis are outlined along with suggestions for future experimental validation. Some limitations of the performance indicator are considered and possible paths of research to expand the scope of the indicator beyond these limitations are proposed.

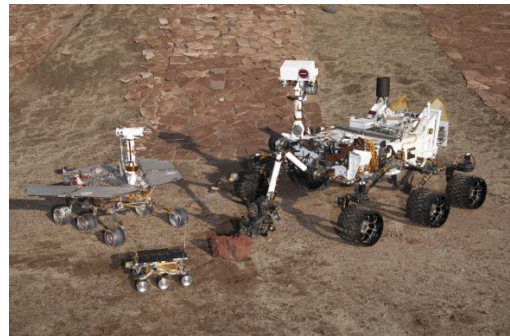
CHAPTER 2 Background and Literature Review

2.1 Contact Force Analysis with Planetary Rovers

Over the past five decades, planetary exploration rovers have been established as a highly useful element in the exploration of extraterrestrial surfaces. From the early Russian Lunokhod series of moon rovers [8, 9] in the 1970's to the most recent launch of NASA's Micro Science Laboratory (MSL) rover, Curiosity [5], rovers have allowed us to push the boundaries of our celestial understanding without compromising human safety. To date, NASA has landed four rovers on Mars, starting with the microrover flight experiment (MFEX), the Sojourner [4] in 1997, followed by the Mars Exploration Rovers (MER) Spirit and Opportunity [3] in 2003, to the MSL rover, Curiosity in 2012. Upcoming expeditions involve a collaboration between the European and Russian space agencies (the ESA and Roscomsmos) to land the ExoMars rover [10] on Mars in January 2019, and NASA plans to put another rover on the red planet in 2020 [76].



(a) ExoMars prototype at the Airbus Defense and Space Mars Yard, Stevenage, UK.



(b) JPL Rovers from largest to smallest, models of: Curiosity, Spirit and Sojourner Mars rovers.

In most cases planetary rovers must be fully autonomous where locomotion is concerned. This is due to the time delay in the relay of information between Earth and the majority of celestial destinations. Between Earth and the Moon, a signal relaying delay is just three seconds, allowing

the Lunokhod rovers to be teleoperated from Earth. Information between Earth and Mars however, takes between 3 to 22 minutes. This makes teleoperation of a Mars rover from Earth quite impractical, especially in the case of driving from one destination to another. As a consequence, most planetary rovers have to be capable of autonomous navigation in order to reach their daily destination. Navigating through the environment however also requires that the rover be able to negotiate the chosen path, which can often consist of slippery, sandy landscapes and rocky, uneven terrain. The design of autonomous rovers, that will maximize their capacity to safely cross such terrain without human input, has been a primary challenge since their first conception. Contact and impact analysis are of importance in the development of a rover design that supports the necessary degree of autonomy and endures the hazardous conditions of the voyage.

Regarding impact, since the speed of a typical planetary rover is not very extreme, usually less than 10 cm/s, most rovers are examined under the assumption of quasi-static conditions, as the dynamic effects at such low velocities are negligible [18]. In [63] however, three events in which rover impacts must be expected and designed for are listed as: 1) initial egress from the lander, 2) small, unplanned collisions occurring throughout the travels of the rover, and 3) the impact due to a planned drop-down off of an obstacle in a typical obstacle negotiation scenario. Analysis of impact forces resulting from these collisions, are typically performed using structural analysis with CAD software and finite element techniques that base the modelling of contact and impact on one of several available methods of contact analysis.

A more common vein of research involving the study of contact forces in planetary rovers, is in the aim of enhancing rover mobility. Enhancing mobility involves finding a balance between rover stability, and the ability of the rover to develop traction with the underlying terrain. To this end, planetary rover design has covered a wide spectrum involving locomotion platforms based on wheels [65], legs [2], tracks [77, 71], hopping mechanisms [38] and various other modes of propelling the rover. The most thoroughly researched designs however, follow the trend set by successful models that have proven themselves reliable on Mars or the Moon. Features of such

designs include six wheeled rovers, having some actively articulated degrees of freedom, and a passively reconfigurable suspension.

The six wheel concept was found as a compromise between low weight, and rover mobility. While the successful Russian Lunokhod moon rovers had eight wheels, modern space program weight and volume constraints make lighter, six wheeled rovers more feasible [88]. Further reduction to four wheeled rovers however, considerably reduces mobility on uneven, rocky terrain, as the rover must balance often on just the two front, or rear wheels, as the other set of wheels overcomes an obstacle.

The active articulation concept to improve mobility, has been developed by many researchers in applications involving off-road, rough-terrain vehicles. Active articulation refers to actuation of many of the degrees of freedom of the locomotion subsystem, allowing the rover to actively alter its configuration. In [82], Sreenivasan et al demonstrate that “wheel actively articulated vehicles” (WAAV) can achieve greater mobility in rough terrain applications, especially in their ability to vary their configuration to overcome obstacles. A similar conclusion is drawn in [59]. This theory has given rise to prototype rovers such as the Mars Sample Return Rover (SRR) [43], with actively articulated shoulder joints, and the GoFor rover [81] with actuated forks and wheels. In [81] Sreenivasan et al demonstrate with the GoFor microrover, how active actuation of the forks and wheels of the rover can be used to influence the contact forces developed at the wheel-terrain contact points, improving the mobility of the microrover. This can be achieved by shifting the centre of mass (CoM) of the rover to optimize weight distribution or normal force distribution over wheels which can develop more traction or provide greater stability. This concept is explored with rovers or mobile robots in [61, 27, 79]. In [30], the normal force distribution is also manipulated. Rather than controlling the normal force distribution with the CoM however, active actuation of the suspension system is used to push directly onto wheels where the extra load will optimize traction. This actively actuated kinematic suspension system is demonstrated to enhance mobility when compared to the same rover with normally passive kinematic suspension, in soft soil, slope

climbing applications. Another venue of active articulation in legged-wheeled rovers is the actuated pivoting of the legs, known as wheel walking . In [89], a four wheeled lunar prospector is used to demonstrate how traction is enhanced, by locking the rear or the front wheels. The locked joints are then used as fixed points from which to push or pull the remaining wheels against, as the pivoting legs allow the body of the rover to expand or contract accordingly. This manoeuvre is achieved with the actuation of the rover legs or forks, and produces a motion referred to as “inch worming”. The ExoMars rover will be equipped with actuators between the legs and bogies, referred to as deployment actuators, as they will deploy the rover from its stowed configuration during transport to Mars [86]. Actuation of these deployment actuators in a wheel walking context is explored in [12] where an ExoMars-like rover demonstrates the benefits of wheel walking in three likely rover scenarios: slope climbing, egress from the lander, and climbing out of entrapment in loose, dry sand.

The benefits of reconfigurability are also captured with passive suspension designs, however these passive systems also reduce some of the complexity and power demands that would occur with a fully actuated suspension. This trend was initiated with the JPL rocker bogie suspension for the Sojourner [19, 23]. The rocker bogie suspension offers the rover the advantage of maintaining contact between all six wheels and the ground, even when the rover is at high angles of inclination. This provides extra stability on sloped or uneven terrain. Additionally, the weight of the rover is distributed more evenly amongst the six wheels, ensuring that all wheels apply load to the terrain, and can consequently develop traction. The even distribution also prevents excessive wheel pressures from developing on just one or two wheels, which could be troublesome in deformable soil. The passive suspension trend is followed with the three-bogie passive suspension design for the ExoMars rover [72, 70]. The main effect these trends in planetary exploration rovers have on mobility, is that the extra degrees of freedom, and reconfigurable elements of the system, influence the wheel-terrain contact forces which propel the rover along its chosen path.

In preparation for the Mars Exploration Rover (MER) expedition in 2003, NASA established mobility criteria of minimum obstacle height and slope grade. Rovers were required to climb an

obstacle of at least 25 cm, and to traverse a slope of 16° [63]. The required slope grade was later raised to 30° when it became apparent with the experience of the MER's that this was both a feasible and necessary expectation. The obstacle height however still stands as a requirement for ExoMars rover mission prototypes [72]. In order to meet these standards with an optimal rover design, analysis of the mobility of a rover has been developed and geared towards quantifying rover performance. This analysis involves developing models for the contact forces at the wheel-terrain interface, and is more involved than it might be for a fixed configuration vehicle such as a car, since contact forces shift as the configuration of the contacting system is altered. To this end, kinematic and dynamic or quasi-static analysis are performed with a model of the rover and the underlying terrain. The equations of motion of the model can be developed with Lagrange or Newton-Euler formulations [33] and integrated to produce simulations of the behaviour of a given rover model in various types of terrain. Simulation tools with generic or specialized multibody dynamics software such as RCAST [13], SIMPACK [78] and ROAMS [74] are typically used to aid the analysis. Regarding the modelling of the terrain, for traversal and slope climbing on soft deformable ground, the field of terramechanics, pioneered by Bekker [17] and later supplemented by researchers such as Wong and Reece [91] among others, plays a large role in the evaluation of planetary rover mobility. This research provides a theoretical foundation for the analysis of the terrain reaction forces that develop at the wheel-terrain contact areas in response to the operation of the rover. The research offers a tool that can assist in predicting phenomena such as wheel sinkage and slip, which are often assumed negligible on rigid terrain. Terramechanics relationships have been applied to mobile, reconfigurable robots by researchers such as Iagnemma and Dubowsky [44], Ishigami et al [46], and Gibbesch and Schafer [31].

For hard soil and rocky terrain, the most common analysis is quasi-static analysis of the normal and tangential forces developed by the rover, with a rigid model of the terrain. Analysis similar to that in [81], where forces arising from the wheel-terrain contacts, that are required to move the rover in a desired manner are evaluated, and the configuration to best achieve these forces is determined. Additionally the wheel-terrain contact points are analyzed to assess how capable

they would be of developing the necessary normal and frictional forces. This type of analysis is particularly important in obstacle negotiation, as obstacles are usually assumed to be rigid, and some faces for wheel-terrain contact with the obstacle itself can be unsuitable for developing the amount of friction necessary to surmount it. Apostolopoulos [11], performed a quasi-static analysis of a parametrically defined rover to propose that rover design and configuration can be used to optimize the contact forces in the normal and tangential directions to assist a rover in obstacle negotiation. To maximize stable slope climbing, Jarrault et al [48] compare the capacity of a given rover configuration to develop necessary wheel-terrain contacts forces, with the resulting stability of the posture, for a range of possible configurations. The analysis is used to assess the most stable posture for successful negotiation of a given obstacle. Shifting of the CoM was used in obstacle negotiation by Skonieczny and D'Eleuterio [79], and a control algorithm using terrain angles measured relative to the inclination of the rover body was implemented, to evaluate the potential traction that a wheel-terrain contact can develop. Performance metrics or indicators are also a useful tool in mobility analysis. Thueer [85] introduces three performance metrics to compare the obstacle climbing of three different rover suspension designs. One of these metrics is the minimum friction coefficient required by the rover to maintain stability on uneven terrain. This coefficient is the ratio between the normal force and the required (tangential) frictional force developed at the wheel-terrain interface. In [73] the ratio of vehicle weight to percentage of vehicle weight loaded on a given wheel, is used as an indicator to assess the traction forces that a particular wheel-terrain contact can supply.

In this thesis, a performance indicator, relating contact forces to rover configuration in a contact or impact scenario is proposed. Since configuration is used to enhance the mobility of the rover by manipulating the wheel-terrain contact forces, knowledge of the relationship between the two is necessary to design for obstacle climbing capacity and additionally to withstand potential impacts. While this knowledge can be gained by explicitly modelling and simulating the contact process, the information required for this type of modelling is often difficult to obtain. Additionally, the process can be computationally expensive and time consuming. The proposed performance indicator

is thus presented as an alternative to contact modelling, for applications such as planetary exploration where force modelling parameters related to the extra-terrestrial environments are unknown. The indicator requires no integration of the equations of motion, making it fast and computationally economic. This feature renders the indicator useful for applications such as online computation for anticipatory behaviour. Such behaviour could include assuming an optimal posture in preparation for obstacle negotiation or for an expected impact. As contact force models are used to validate this indicator, some of the established methods for modelling of contact events in dynamic multibody systems are discussed below.

2.2 Contact Background and Modelling Methods

The study of contact is pertinent to a wide range of industrial and academic applications. High speed impact analysis in the automotive industry, the perfection of robotic grasping procedures in the robotics industry and wear and tear analysis on bearings, gears and joints in mechanical design applications are just a few of the fields benefiting from this research. Contact and impact occur when two bodies touch, or collide with each other. Impact, usually occurs over short time intervals, and involves large forces and accelerations. It is sometimes defined as the special case of contact in which the transition from separation to contact between the contacting bodies, occurs [25]. The term contact however, which is often used interchangeably with impact, is less clearly defined. In [32], Giliardi and Sharf state that “Inherently contact implies a continuous process which takes place over a finite time”. The analysis of the response of a system to contact or impact can be very complex. This is because the system response is dependent on the material and geometric properties of the contacting bodies and can lead to phenomena such as friction at the contact interface, internal dissipation of energy, wave propagation, and local and sometimes global deformation. To analyze contact and impact, a variety of methods are available and applicable depending on what the focus of the analysis is. Most of these techniques can be classified as either discrete or continuous approaches. The most traditional form of analysis, belongs to the former category, and was developed from Newton’s classical theory for central impact, between two particles. This approach models the contact as a sharp impulse that leads to jump discontinuities in the system velocities.

In this analysis the contacting bodies are modelled as rigid bodies and the duration of contact is negligible, so that the configuration of the system is assumed to remain constant, while the bodies are in contact. The balance of momentum between colliding particles at pre- and post-impact states is then used to determine the unknown variables. Typically, pre-impact velocities or momenta are known, while post impact velocities or momenta are sought. To this end, the impulse-momentum equations must be supplemented with a coefficient such as Newton's kinematic or Poisson's kinetic coefficients of restitution. These parameters relate pre- and post-impact velocities, or pre- and post-impact impulse [75] of the system, and are a mechanism by which energy loss in the contact process can be accounted for. In 1904, Newton's impact analysis was adapted by Whittaker [90] to include contact with the presence of friction, establishing an accepted approach to impact analysis for most of the 20th century. In 1984, an article published by Kane [51] pointed out that in situations involving this type of modelling, where the friction force in certain impacts switches direction, an increase in kinetic energy can result. This led to renewed attention to the problem and solutions proposed in works by Keller [52], Smith [80], Brach [20] and Stronge [83] to name a few. An extensive literature review on this material is outlined in [21]. This analysis deals only with the contact at the impulse and momentum level, and due to the discontinuities occurring in the velocities of the colliding bodies as contact is made, information about the contact forces that drive the bodies apart cannot be ascertained. For information about the contact forces themselves, the continuous, or force based approach is presented as an alternative.

The force based approach, models the contact force as a continuous force that develops as the contacting bodies deform throughout the contact process. One class of force based methods used in this thesis are penalty methods, which generally assume a global rigid body model of the system, but permit a degree of deformation in the zone of contact. This deformation is then modelled as the overlapping or penetration that would occur, were the rigid bodies superimposed over the contacting locally deformable ones. Various contact models, dependent on the degree of penetration, are then used to evaluate the resulting normal and tangential contact forces. The contact models are typically based on the Hertzian theory [40] of static contact force developed

between two contacting spheres, and have been adapted to account for dissipative effects. The general structure of a continuous force model formulation is:

$$f = k\delta^p + b\delta^n\dot{\delta} \quad (2.1)$$

where k and b are stiffness and damping parameters dependent on the geometric and constitutive properties of the system, while n and p are exponents designating the degree of non linearity particular to the each contact model. The contact force f , developed by the model is then related to the degree of indentation δ of the contacting bodies, and the associated penetration velocity $\dot{\delta}$, thus producing a smooth evolution of contact force throughout the duration of the contact event. Consequently there are no jump discontinuities in the variables such as the system velocities, and contact forces remain finite. These models can then be incorporated into the equations of motion of a multibody dynamic simulation, and integrated. Some difficulties arise when very rigid systems with little penetration are to be modelled, as the equations of motion can become stiff [54], and the system can become ill conditioned. Other drawbacks of this representation of contact are that contact forces can become tensile when relative velocities reverse their directions as the contacting bodies move apart [66]. Because the model is an idealization of the actual impact process, the accuracy of solutions using penalty methods is variable, depending heavily on the parametrization of the stiffness and damping properties of the colliding system. Each contact model is typically limited to a specific set of impact conditions such as those of low impact velocities and high coefficients of restitution. In this thesis, force based models are used to validate the proposed indicator for impact and are integrated into the equations of motion developed in a McGill written, MatLab based code for multibody dynamic simulation. Further background on the models used for this purpose is given in Chapter 5. For an extensive overview of continuous force models the reader is referred to [64, 32].

2.3 The Effective Kinetic Energy of an Impact

In the methods for the modelling of contact discussed above, specific parametrization of the system with respect to constitutive properties are required to a greater or lesser degree. The task of

obtaining the correct parameters can be formidable, and the outcome greatly affects the accuracy of the results. As an alternative, a performance indicator for impact and contact force, which doesn't rely on these parameters is proposed. This performance indicator is evaluated by partitioning the kinetic energy of the contacting system into a subspace of interest, and its orthogonal complement. The kinetic energy associated with the subspace of interest, is then evaluated at the onset of contact. The partitioning is performed with a projection or transformation of the coordinates at the velocity level onto the desired subspace of motion. For impact applications, this subspace is the subspace of constrained motion (SCM), which consists of the directions normal to the impact planes between contacting bodies within the system. Previous research that will be discussed, shows that the value of kinetic energy in the system, that is associated with the SCM, can be related to the magnitude of the impact force developed in an impact event. This portion of the total kinetic energy of the system, is found to be a useful indicator of impact intensity in an impact situation. The indicator has been termed the "effective kinetic energy of impact".

The concept of partitioning of the kinetic energy into the subspaces of constrained motion and its orthogonal complement the subspace of admissible motion (SAM) was proposed by Kövecses in [55]. Experimental analysis was performed with two, six degree of freedom (DoF), dual pantograph, robotic manipulators in [67]. This pair of manipulators simulated an impact of a robotic arm with a stiff environment. A new interpretation of the energetic coefficient of restitution, initially proposed by Stronge [84], was outlined as the ratio of the kinetic energies associated with the SCM and the SAM. Experimental results demonstrate that effective kinetic energy displayed the same trend as the maximum normal impact force, and so the new performance indicator was initially validated. As explained, the effective energy indicator does not depend on the constitutive properties of the impacting bodies but only on the configuration of a system at the instant of impact. Analysis with effective energy has since been applied to bio-mechanical systems related to impacts resulting from crutch walking, and how the posture of the test subject, can minimize fatigue, wear and tear from crutch impact [28, 22]. A more recent study by González et al [36] examines the ability of the partitioned kinetic energy as a performance indicator for two different systems undergoing an

impact: a double pendulum, and a simple planetary rover model. A variety of continuous force models with a variety of coefficients of restitution were used to evaluate the load applied to the system resulting from the impact. In all cases the value expressed by the energy indicator showed the same variation that was predicted by the force based contact models, as the configuration of the impact was altered. A primary portion of this thesis is dedicated to the investigation of the reliability of effective kinetic energy as an impact performance indicator, especially in the case of planetary rovers. A planetary rover prototype based on existing Mars rover design, which has been modelled in three dimensional space, will serve as the test platform for impact analysis throughout this thesis. In this case, the system is modelled with both redundant degrees of freedom, and redundant constraints, while dealing with a more complex linkage than previous studies have done. Simulations carried out with a multibody dynamics library code, written at McGill University will be discussed. A set of experiments which have been performed on the existing rover prototype, will also be analyzed and compared to the results achieved through simulation. Finally, some limitations on the effective energy indicator will be discussed and possible directions of future work proposed.

CHAPTER 3

Introduction To Effective Kinetic Energy

In certain cases of impact analysis, the numerical value of the impact force is less a topic of interest than the trend that this force will follow as a parameter of the system is varied. In an impact scenario with a planetary rover and an obstacle for example, if the length of a bogie, or the centre of mass of the rover is altered, information about how the impact force depends on these parameters, can aid the design of the rover. In such cases, a performance indicator for the relative intensity of impact can be found with a particular partitioning of the kinetic energy of the system.

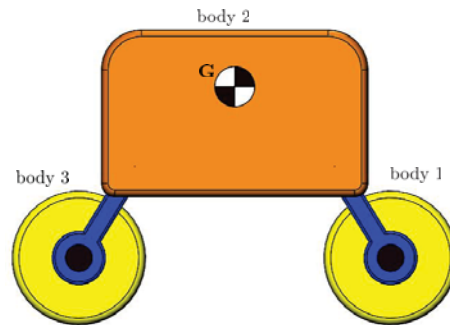


Figure 3–1: Two-dimensional model of a rover.

Consider the simple model of a two-dimensional rover shown in Fig.(3–1). The model is very similar to that used in previous rover simulations in [36], having bodies 1,2 and 3 representing the front wheel, main body with connecting links, and rear wheel of the rover respectively, with a combined centre of mass at G . For the purposes of demonstration throughout the chapter, let the two-dimensional model be further simplified into the two-body model shown in Fig. (3–2). Now the main body, rear wheel, and connecting links are all combined into the lumped mass of body 1, with a mass of m_1 and again having a combined centre of mass at G_1 . The front wheel is still represented by body 2, having mass m_2 with the centre of mass located at G_2 and connected to body 1 with a revolute joint also located at G_2 . For simplicity, when referring to this two-body

rover model, body 1 will hereafter be referred to as “the chassis” and body 2 will be referred to as “the wheel”.

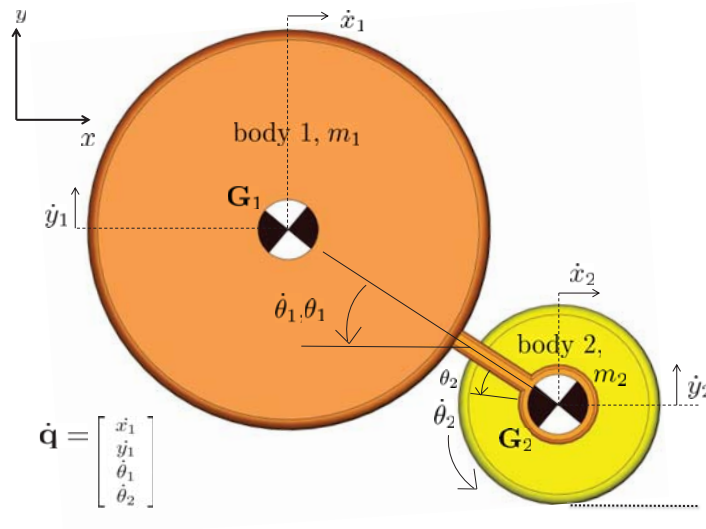


Figure 3–2: Two-mass simplification of two-dimensional rover

The two-body system, having four degrees of freedom, can now be characterized by four, independent, generalized coordinates which will compose the 4×1 array \mathbf{q} . There are many options for the choice of coordinates used to parametrize this system. However, although the dynamic behaviour of the system remains the same regardless of the parametrization used to describe it, different parametrizations can give different information. This can be useful for various applications. Consider for example that initially the generalized coordinates x_1 and y_1 , represent the x and y positions of the centre of the chassis in Fig. 3–2 with respect to the fixed frame. Additionally, θ_1 , and θ_2 represent the rotations of the chassis, and the wheel within the x - y plane. This gives the generalized coordinates and velocities, i.e, system coordinates at the configuration and velocity levels as $\mathbf{q} = [x_1 \ y_1 \ \theta_1 \ \theta_2]^T$ and $\dot{\mathbf{q}} = [\dot{x}_1 \ \dot{y}_1 \ \dot{\theta}_1 \ \dot{\theta}_2]^T$. Using the position and velocity level relationships:

$$x_2 = x_1 + l \cos \theta_1 \qquad y_2 = y_1 + l \sin \theta_1 \qquad (3.1)$$

$$\dot{x}_2 = \dot{x}_1 - l\dot{\theta}_1 \sin\theta_1 \qquad \dot{y}_2 = \dot{y}_1 + l\dot{\theta}_1 \cos\theta_1 \quad (3.2)$$

the kinetic energy of the system can then be formulated as:

$$T = \frac{1}{2}m_1(\dot{x}_1^2 + \dot{y}_1^2) + \frac{1}{2}I_1\dot{\theta}_1^2 + \frac{1}{2}m_2 \left((\dot{x}_1 - l\dot{\theta}_1 \sin\theta_1)^2 + (\dot{y}_1 + l\dot{\theta}_1 \cos\theta_1)^2 \right) + \frac{1}{2}I_2(\dot{\theta}_1 + \dot{\theta}_2)^2 \quad (3.3)$$

where m_1 , m_2 , I_1 and I_2 are the masses and second moments of inertia about the centres of mass G_1 and G_2 respectively. The distance between the chassis and wheel centres is l , and T is the total kinetic energy of the system. If we disregard the effects of gravity for the purposes of demonstration, then the system has no potential energy term and the Lagrangian reduces to just the total kinetic energy. The equations of motion can then be formulated from Lagrange's equations:

$$\frac{d}{dt} \left(\frac{\partial T}{\partial \dot{\mathbf{q}}} \right) - \frac{\partial T}{\partial \mathbf{q}} = \mathbf{f} \quad (3.4)$$

where \mathbf{f} is the array of generalized forces. The expansion of Eq. (3.4) can be found in Appendix A. The resulting dynamic equations can also be written in compact matrix form as:

$$\mathbf{M}\ddot{\mathbf{q}} + \mathbf{c} = \mathbf{f} \quad (3.5)$$

where \mathbf{M} is the 4×4 generalized mass matrix of the system, \mathbf{c} represents the 4×1 centrifugal and Coriolis term, and \mathbf{f} is the 4×1 generalized force term. The mass matrix, and centrifugal and Coriolis terms can be expressed as:

$$\mathbf{M} = \begin{bmatrix} m_1 + m_2 & 0 & -m_2 l \sin\theta_1 & 0 \\ 0 & m_1 + m_2 & m_2 l \cos\theta_1 & 0 \\ -m_2 l \sin\theta_1 & m_2 l \cos\theta_1 & I_1 + I_2 + m_2 l^2 & I_2 \\ 0 & 0 & I_2 & I_2 \end{bmatrix} \qquad \mathbf{c} = \begin{bmatrix} -m_2 l \dot{\theta}_1^2 \cos\theta_1 \\ -m_2 l \dot{\theta}_1^2 \sin\theta_1 \\ 0 \\ 0 \end{bmatrix}$$

As applied forces have not yet been considered for this example, the generalized force term \mathbf{f}

is simply $[0]_{4 \times 1}$. The kinetic energy of the system can also be written as

$$T = \frac{1}{2} \dot{\mathbf{q}}^T \mathbf{M} \dot{\mathbf{q}} \quad (3.6)$$

In many cases, a certain subspace of the motion of the system, which represents a particular mode of motion or interaction, is of interest to the analyst. A particular parametrization can isolate the dynamic behaviour of this subspace. A common example of this occurring frequently in robotics, is in the analysis and control of robotic manipulators. An intuitive parametrization of the motion of the manipulator is with the joint coordinates, which are directly controlled by joint actuators. The equations of motion of the system, are often simpler to derive from joint coordinates due to their direct relationship with the applied torques and forces of the system. In the control of a manipulator however, the motion of the end effector is typically of greater interest than the motion of the joints. This motion space of interest is referred to as the operational space and is directly parametrized by the coordinates of the end effector. Switching between joint coordinates and operational space coordinates can be achieved with the appropriate transformation Jacobian, allowing the analyst to view the motion of the system with respect to movement of interest. The operational space can fully describe the motion of the manipulator, or it can describe just a subspace of the motion of the system. The remaining motion of the system can be visualized as motion within the manipulator links that do not result in displacement of the end effector. This subspace is often referred to as the subspace of admissible motion, which is loosely based on the idea of motion that is admissible, or compatible with the system constraints. The operational space concept is discussed in detail in [53]. For a mobile robot such as a rover, not necessarily equipped with an end effector or a fixed base, an operational space is less clearly defined. In [41], this space is defined in several ways, depending on the task or subject of analysis. One such definition for example, designates as the operational space, the motion of the contact points between the rover wheels and the underlying terrain. With regard to impact analysis, the region of interest lies at the contact points between the colliding bodies. Let the motion space of any such contact points define a new operational space of motion for rovers, where contact and impact are of interest. This is depicted at point C in Fig 3–3,

which now displays the two-body rover undergoing impact with an obstacle. The plane of impact on the obstacle is inclined at an angle β . A parametrization that isolates this operational subspace

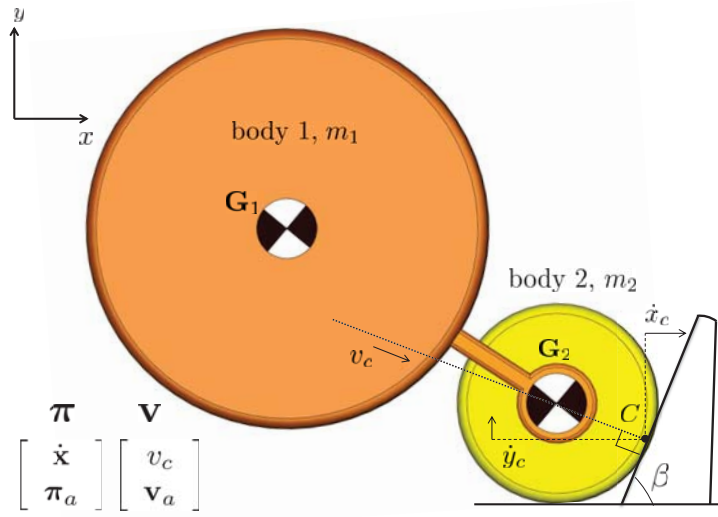


Figure 3–3: Two-mass system with normal and tangential impact coordinates.

is the velocity level parametrization $\boldsymbol{\pi} = [\dot{\mathbf{x}}, \boldsymbol{\pi}_a]$. In this parametrization, $\dot{\mathbf{x}} = [\dot{x}_c \ \dot{y}_c]^T$, where \dot{x}_c and \dot{y}_c are the velocity components, relative to the fixed frame, of the point (C) on the wheel, that comes into contact with the obstacle. Using Eq. (3.1) and Eq. (3.2) array $\dot{\mathbf{x}}$ can be written as:

$$x_c = x_1 + l \sin \theta_1 + R \sin \beta \qquad y_c = y_1 + l \sin \theta_1 - R \cos \beta \qquad (3.7)$$

$$\dot{x}_c = \dot{x}_1 - l \dot{\theta}_1 \sin \theta_1 + R \dot{\theta}_2 \cos \beta \qquad \dot{y}_c = \dot{y}_1 + l \dot{\theta}_1 \cos \theta_1 + R \dot{\theta}_2 \sin \beta \qquad (3.8)$$

Equations (3.7) and (3.8) are written out in detail in Appendix A. A partial transformation from $\dot{\mathbf{q}}$ to $\dot{\mathbf{x}}$ is given as: $\mathbf{A} \dot{\mathbf{q}} = \dot{\mathbf{x}}$ where:

$$\mathbf{A} = \begin{bmatrix} 1 & 0 & -l \sin \theta_1 & R \cos \beta \\ 0 & 1 & l \cos \theta_1 & R \sin \beta \end{bmatrix} \qquad (3.9)$$

The 2×1 array $\boldsymbol{\pi}_a$ can be considered to span the subspace of admissible motion, and contains the other two generalized velocity components necessary to make $\boldsymbol{\pi}$ a full representation of the velocity field of the system. Initially, the components represented by $\boldsymbol{\pi}_a$ can remain unspecified as

long as they satisfy this condition. It will be shown presently however, that a more specific choice for π_a is advantageous to the analysis at hand. The full transformation between the two sets of generalized velocities can be given as:

$$\mathbf{G}\dot{\mathbf{q}} = \begin{bmatrix} \mathbf{A} \\ \mathbf{B} \end{bmatrix} \dot{\mathbf{q}} = \begin{bmatrix} \dot{\mathbf{x}} \\ \pi_a \end{bmatrix} = \boldsymbol{\pi}, \quad \dot{\mathbf{q}} = \mathbf{G}^{-1}\boldsymbol{\pi} \quad (3.10)$$

where \mathbf{G} is the 4×4 Jacobian transformation matrix transforming $\dot{\mathbf{q}}$ into $\boldsymbol{\pi}$, \mathbf{A} is defined in Eq. (3.9), and the 2×4 matrix \mathbf{B} , along with π_a , will remain unspecified for now. A requirement of the operation in Eq. (3.10) is that \mathbf{G} be invertible. This however should be the case, since \mathbf{G} represents a full transformation matrix between two parametrizations of the velocity field. To transform the equations of motion, Eq. (3.5), so that they are written in terms of $\boldsymbol{\pi}$, consider the fundamental variational equation:

$$\delta\dot{\mathbf{q}}^T(\mathbf{M}\ddot{\mathbf{q}} + \mathbf{c} - \mathbf{f}) = 0 \quad (3.11)$$

where $\delta\dot{\mathbf{q}}$ represents variations at the velocity level that quantify possible modes of motion. As velocities are transformed in the same way as variations, $\delta\dot{\mathbf{q}}^T$ in Eq. (3.11) can be replaced in turn by $\delta\boldsymbol{\pi}^T\mathbf{G}^{-T}$ giving:

$$\delta\boldsymbol{\pi}^T\mathbf{G}^{-T}(\mathbf{M}\ddot{\mathbf{q}} + \mathbf{c} - \mathbf{f}) = 0 \quad (3.12)$$

Considering that $\delta\boldsymbol{\pi}$ also gives a full representation for all possible modes of motion, Eq.(3.12) leads to the dynamic equations:

$$\underbrace{\mathbf{G}^{-T}\mathbf{M}\mathbf{G}^{-1}}_{\mathbf{W}}\dot{\boldsymbol{\pi}} + \underbrace{\mathbf{G}^{-T}\mathbf{M}\dot{\mathbf{G}}^{-1}\boldsymbol{\pi}}_{\mathbf{z}} + \mathbf{G}^{-T}\mathbf{c} - \underbrace{\mathbf{G}^{-T}\mathbf{f}}_{\boldsymbol{\tau}} = 0 \quad (3.13)$$

where \mathbf{W} is the 4×4 generalized mass matrix with respect to the new generalized velocities $\boldsymbol{\pi}$, and \mathbf{z} and $\boldsymbol{\tau}$ are the 4×1 arrays corresponding to the centrifugal and Coriolis terms and the generalized

force terms. The term $\dot{\mathbf{G}}^{-1}$ refers to the time derivative of the inverse of matrix \mathbf{G} , ie $\frac{d}{dt}(\mathbf{G}^{-1})$.¹

Now $\mathbf{W} = \mathbf{G}^{-T}\mathbf{M}\mathbf{G}^{-1}$ can be also be expanded as:

$$\mathbf{W} = \begin{bmatrix} \mathbf{A} \\ \mathbf{B} \end{bmatrix}^{-T} \mathbf{M} \begin{bmatrix} \mathbf{A} \\ \mathbf{B} \end{bmatrix}^{-1} = \left(\begin{bmatrix} \mathbf{A} \\ \mathbf{B} \end{bmatrix} \mathbf{M}^{-1} \begin{bmatrix} \mathbf{A}^T & \mathbf{B}^T \end{bmatrix} \right)^{-1} = \begin{bmatrix} \mathbf{A}\mathbf{M}^{-1}\mathbf{A}^T & \mathbf{A}\mathbf{M}^{-1}\mathbf{B}^T \\ \mathbf{B}\mathbf{M}^{-1}\mathbf{A}^T & \mathbf{B}\mathbf{M}^{-1}\mathbf{B}^T \end{bmatrix}^{-1} \quad (3.14)$$

If we consider that the inverse of \mathbf{G} can be expressed as: $\mathbf{G}^{-1} = [\mathbf{C} \ \mathbf{D}]$, then the generalized mass matrix becomes

$$\mathbf{W} = \begin{bmatrix} \mathbf{C}^T\mathbf{M}\mathbf{C} & \mathbf{C}^T\mathbf{M}\mathbf{D} \\ \mathbf{D}^T\mathbf{M}\mathbf{C} & \mathbf{D}^T\mathbf{M}\mathbf{D} \end{bmatrix} \quad (3.15)$$

An interesting property of these equations is that if the subspaces of motion spanned by the rows of matrices \mathbf{A} and \mathbf{B} are mass orthogonal, then the off diagonal terms of Eq. (3.14) drop out, and the generalized mass matrix becomes decoupled. This implies that the operational subspace of motion is orthogonal to the subspace of admissible motion. For this reason π_a was left unspecified, however it is possible to choose π_a so that this condition of orthogonality is satisfied. A method to develop the sets of coordinates spanning orthogonal subspaces which together span the entire system under analysis, is outlined for the general n DoF case in [56]. This method is followed for the two-body system to develop a selection for π_a that is orthogonal to the space spanned by $\dot{\mathbf{x}}$ and is given as:

$$\boldsymbol{\pi}_a = \begin{bmatrix} \eta_1 \\ \eta_2 \end{bmatrix} = \begin{bmatrix} \dot{\theta}_1 + \frac{\dot{x}_2((m_1 + m_2)R\gamma\cos\beta + lm_1\delta\sin\theta_1)}{\alpha\delta - \gamma^2} - \frac{\dot{y}_2(lm_1\delta\cos\theta_1 - \gamma\kappa)}{\alpha\delta - \gamma^2} \\ \dot{\theta}_2 - \frac{\dot{x}_2((m_1 + m_2)R\alpha\cos\beta + lm_1\gamma\sin\theta_1)}{\alpha\delta - \gamma^2} - \frac{\dot{y}_2(\alpha\kappa - lm_1\gamma\cos\theta_1)}{\alpha\delta - \gamma^2} \end{bmatrix} \quad (3.16)$$

where, along with Eq. (3.1) and Eq. (3.2), the substitutions of:

$$\alpha = I_1 + I_2 + l^2m_1 \quad (3.17)$$

¹ This term can be evaluated with the following relationship:

$$\mathbf{G}\mathbf{G}^{-1} = \mathbf{I} \implies \frac{d}{dt}(\mathbf{G}\mathbf{G}^{-1}) = 0 \implies \frac{d}{dt}(\mathbf{G}^{-1}) = -\mathbf{G}^{-1}\dot{\mathbf{G}}\mathbf{G}^{-1}$$

$$\kappa = R(m_1 + m_2)\sin\beta \quad (3.18)$$

$$\gamma = I_2 + m_1 l R \sin(\beta - \theta_1) \quad (3.19)$$

$$\delta = I_2 + (m_1 + m_2)R^2 \quad (3.20)$$

have been made to simplify the expressions. Using this set of coordinates, the generalized mass matrix \mathbf{W} then becomes block diagonal resulting in:

$$\mathbf{W} = \begin{bmatrix} \mathbf{C}^T \mathbf{M} \mathbf{C} & 0 \\ 0 & \mathbf{D}^T \mathbf{M} \mathbf{D} \end{bmatrix} = \begin{bmatrix} \mathbf{A} \mathbf{M}^{-1} \mathbf{A}^T & 0 \\ 0 & \mathbf{B} \mathbf{M}^{-1} \mathbf{B}^T \end{bmatrix}^{-1} \quad (3.21)$$

which implies that $\mathbf{C}^T \mathbf{M} \mathbf{C}$ now equals $(\mathbf{A} \mathbf{M}^{-1} \mathbf{A}^T)^{-1}$ and $\mathbf{D}^T \mathbf{M} \mathbf{D}$ now equals $(\mathbf{B} \mathbf{M}^{-1} \mathbf{B}^T)^{-1}$. Now the subspace of interest can be considered in a form that is decoupled from the other subspace. One advantage of this is that the kinetic energy of the system can also be partitioned into kinetic energy associated with each individual subspace. The kinetic energy associated with each of the subspaces of operational and admissible motion can be formulated as:

$$T_{op} = \frac{1}{2} \dot{\mathbf{x}}^T (\mathbf{A} \mathbf{M}^{-1} \mathbf{A}^T)^{-1} \dot{\mathbf{x}} \quad T_a = \frac{1}{2} \boldsymbol{\pi}_a^T (\mathbf{B} \mathbf{M}^{-1} \mathbf{B}^T)^{-1} \boldsymbol{\pi}_a \quad (3.22)$$

where T_{op} is the kinetic energy associated with $\dot{\mathbf{x}}$, and T_a is the kinetic energy associated with $\boldsymbol{\pi}_a$.

The total kinetic energy of the system is the sum of the two giving:

$$T = T_{op} + T_a \quad (3.23)$$

As mentioned in Chapter 2, in the study of impact, a subspace of particular interest is the subspace of constrained motion (SCM), which is characterized by the generalized velocities that represent directions normal to the surfaces subject to impact. A transformation of the system coordinates, similar in concept to the operational space transformation, can be performed to produce a parametrization that isolates these directions of constrained motion. In Fig. 3–3 the direction labelled v_c , running normal to the impact plane between the obstacle and the wheel, is the direction of constrained motion for the two-body example. This direction can be described with a rotation of the coordinates \mathbf{x} . To transform $\boldsymbol{\pi}$ into the constrained velocities the 1×4 transformation Jacobian

\mathbf{R}_c is used as follows:

$$\mathbf{R}_c \boldsymbol{\pi} = v_c, \quad \mathbf{R}_c = \begin{bmatrix} \sin\beta & -\cos\beta & 0 & 0 \end{bmatrix} \quad (3.24)$$

A direct transformation from the original set of velocities $\dot{\mathbf{q}}$ is given as follows:

$$\underbrace{\mathbf{R}_c \mathbf{G}}_{\mathbf{J}_c} \dot{\mathbf{q}} = v_c, \quad \mathbf{J}_c = \begin{bmatrix} \sin\beta & -\cos\beta & -l\cos(\beta - \theta_1) & 0 \end{bmatrix} \quad (3.25)$$

While v_c , which happens to be a scalar value for this example, now parametrizes the subspace of constrained motion of the two-body rover, the subspace of admissible motion consists of the velocities of the contact point C that are parallel to the impact plane, and the remainder of the motion space independent of motion at point C . The set of coordinates containing the v_c and \mathbf{v}_a parametrizations shall be referred to as \mathbf{v} , giving the full transformation from $\dot{\mathbf{q}}$ to \mathbf{v} as:

$$\begin{bmatrix} \mathbf{J}_c \\ \mathbf{J}_a \end{bmatrix} \dot{\mathbf{q}} = \begin{bmatrix} v_c \\ \mathbf{v}_a \end{bmatrix} = \mathbf{v} \quad (3.26)$$

Here \mathbf{v}_a is the 3×1 array of velocities parametrizing the SAM, and \mathbf{J}_a is the 3×4 array now transforming $\dot{\mathbf{q}}$ into \mathbf{v}_a . The kinetic energy of the system can now be partitioned into T_c , the kinetic energy associated with SCM and T_a the kinetic energy associated with the SAM, as was done with the operational and admissible spaces in Eqs (3.22) and (3.23). The performance indicator, the effective kinetic energy of impact, described in the preceding chapter, is the kinetic energy associated with the SCM, discussed here as T_c . The general expression for effective kinetic energy of impact of a system of n bodies can then be expressed as:

$$T_c = \frac{1}{2} \dot{\mathbf{q}}^T \mathbf{J}_c^T (\mathbf{J}_c \mathbf{M}^{-1} \mathbf{J}_c^T)^{-1} \mathbf{J}_c \dot{\mathbf{q}} \quad (3.27)$$

where \mathbf{M} is the $n \times n$ generalized mass matrix, $\dot{\mathbf{q}}$ is the $n \times 1$ array of generalized independent velocities, and \mathbf{v}_c is the $s \times 1$ array of s velocities spanning the SCM. The transformation matrix bringing the set of velocities $\dot{\mathbf{q}}$ into the constrained velocities \mathbf{v}_c is the $s \times n$ matrix \mathbf{J}_c . The kinetic energy associated with the SAM is not of interest to the topic at hand, and so the parametrization \mathbf{v}_a

need not be determined explicitly. This is particularly convenient given the complexity of a typical parametrization that is contrived to be orthogonal to a subspace of interest, as is evident in Eqs (3.16) to (3.20). By virtue of the process outlined in [56], the knowledge that this parametrization exists, is enough to justify the use of Eq. (3.27), the formulation for kinetic energy associated with a subspace of interest.

In previous research [36], [28], [67], involving the kinetic energy associated with the SCM, a simple system of just a few rigid bodies, and two to six degrees of freedom was described in independent coordinates. The work of this thesis will deal with a system having 28 bodies with a varying number of degrees of freedom. Unlike the examples given above, the coordinates used will be dependent, and therefore constraint equations defining the connections between bodies are explicitly considered. Dependent coordinates are a useful feature to explore with respect to effective kinetic energy, as the use of independent coordinates in generalized multibody dynamics software is often difficult to implement, and dependent coordinates can accommodate a simpler implementation. While conceptually the development of the effective kinetic energy from a set of dependent coordinates is the same as the effective kinetic energy developed with independent coordinates, some technical details that involve the construction of the appropriate transformation matrix differ, and will be discussed in Chapter 5.

The evaluation of T_c that has been outlined above, relies on the transformation of the generalized velocities. An alternate expression for T_c is with the use of mass orthogonal projectors. While the concept remains the same, the technical process differs slightly in that the generalized velocities of the system are projected onto the SCM and SAM, rather than transformed from one set of velocities to another. For this expression of T_c , the Jacobian, \mathbf{J}_c , that transforms the generalized velocities $\dot{\mathbf{q}}$, into the constrained velocities \mathbf{v}_c , is used to generate the projection operator \mathbf{P}_c and its orthogonal complement \mathbf{P}_a . The mass matrix \mathbf{M} is used in both cases as a scaling matrix and acts as the metric or inner product matrix [55]. The projectors \mathbf{P}_c and \mathbf{P}_a can be determined as follows:

$$\mathbf{P}_c = \mathbf{M}^{-1} \mathbf{J}_c^T (\mathbf{J}_c \mathbf{M}^{-1} \mathbf{J}_c^T)^{-1} \mathbf{J}_c \quad \mathbf{P}_a = \mathbf{I} - \mathbf{P}_c \quad (3.28)$$

In many mechanisms, redundant constraints are present for either physical stability of the system or for ease of development of the numerical model. This typically produces a rank deficient constraint Jacobian, which prevents computation of the effective mass matrix $(\mathbf{J}_c \mathbf{M}^{-1} \mathbf{J}_c^T)^{-1}$ in Eq. (3.27). This issue can be resolved with the use of a pseudo-inverse to evaluate the rank deficient effective mass term. Introduction of a pseudo-inverse however, can sometimes imply physically meaningless operations, especially when the terms involved carry units, as is the case with the foregoing equations. A physically meaningful method of dealing with these redundant constraints is explained in [55]. This method produces a metric for the basis of the tangent space of the system with the product $\mathbf{J}_c \mathbf{L}^{-1}$ where \mathbf{L} is the Cholesky decomposition of the mass matrix. The projection operator \mathbf{P}_c is then determined as follows:

$$\mathbf{P}_c = \mathbf{L}^{-1} (\mathbf{J}_c \mathbf{L}^{-1})^\dagger \mathbf{J}_c \quad (3.29)$$

where \dagger symbolizes the Moore-Penrose generalized inverse or pseudo-inverse.

The effective kinetic energy can be expressed using the projection matrices as:

$$T_c = \frac{1}{2} \mathbf{v}^T \mathbf{P}_c^T \mathbf{M} \mathbf{P}_c \mathbf{v} = \frac{1}{2} \mathbf{v}_c^T \mathbf{M} \mathbf{v}_c, \quad \text{where } \mathbf{v}_c = \mathbf{P}_c \mathbf{v} \quad (3.30)$$

An illustration of how effective kinetic energy alters as the impact configuration of a system alters, is given here to facilitate a conceptual understanding of T_c . In Fig. 3–4, the two-body system is shown in impacts with two different impact configurations. In each case the difference in impact configuration pertains to the location of the CoM of body 2. Other than their different configurations, the impacts are identical. In Fig. 3–4, a graphical representation of the SCM and SAM for each body is illustrated with the axes described by the unit vectors \vec{e}_{a_i} and \vec{e}_{c_i} . In the vector notation, c and a refer to constrained and admissible, and i , having values of 1 or 2, specifies with which body the unit vector is associated. For body 2, the wheel, in both cases the constrained direction is the direction normal to the impact plane. The constrained direction of body 1, the

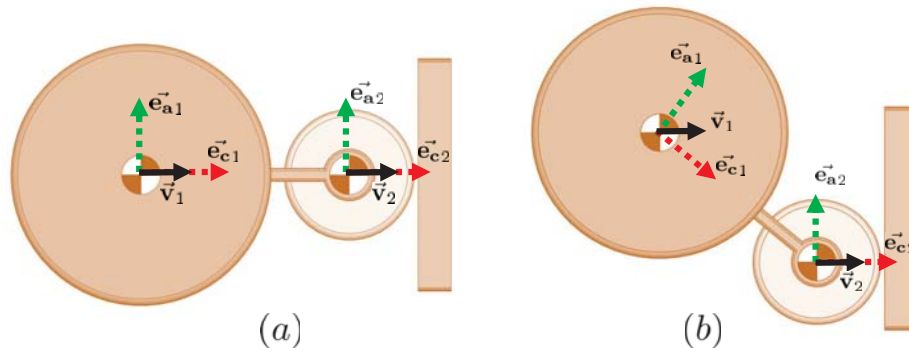


Figure 3–4: Two-mass system impacting a surface with different positions of the chassis CoM.

chassis however, is in the direction of the link that connects the two bodies. This direction is different for each CoM configuration, and so the total SCM of the system differs depending on the impact configuration. By inspection, it can be seen that the velocity, and therefore momentum of the system in case (a) belongs entirely to the SCM, *i.e.* both bodies move in a direction along their respective constrained axes. In case (b) however, the velocity of the chassis, \vec{v}_1 , has components belonging to both subspaces of constrained and admissible motion for body 1. Consequently, in case (a), the momentum of the system belongs completely to the SCM, and therefore the entire kinetic energy of the system is associated with the SCM, and will be absorbed and/or dissipated upon impact. In case (b), some kinetic energy in the system is associated with the SAM, and so will remain in the system upon impact. The simulations and experiments in this thesis demonstrate how different impact configurations such as the varied CoM position in Fig. 3–4 can effect the kinetic energy associated with the SCM, and that this effect is qualitatively related to the maximum contact force developed within the system as the impact takes place.

CHAPTER 4

Simulations with the McGill Generic Multibody Dynamics Library (GMDL)

To further explore the uses of the effective kinetic energy performance indicator, analysis with an existing prototype of a rover is discussed throughout the remainder of this thesis. The analysis can be considered to be a development of the work in [36], where an example based on a planetary rover model impacting a planar surface was used to demonstrate the relationship between effective kinetic energy and peak impact force. The system was modelled in two-dimensional space using independent coordinates, and had five degrees of freedom. The impact and terrain were modelled with constitutive relationships, and impact with a range of coefficients of restitution, and various contact force models was explored. For each simulation, the continuous force models were used to profile the impact force throughout the compression of the impact. At the point during the compression phase that the maximum impact force was achieved, the value was recorded and compared to the value of effective kinetic energy for the system with the given impact configuration. With this method, the values for maximum impact force and effective kinetic energy were compared over a range of variation for a given configuration parameter. Four ways in which the current analysis extends this work to a more general and potentially a more realistic case are: 1) the complexity of the rover model used which will be discussed presently, 2) the use of dependent coordinates instead of independent ones to model the system, 3) the development and discussion of the effects of the terrain on which the rover drives, and 4) experimental validation of the simulated results. The platform for all simulations used in this thesis, is a generic multibody dynamics library, coded by members of the Applied Dynamics Group at McGill University. The library was intended to be used as a simulation tool for the design of planetary rovers and evaluation of rover performance in unstructured environments. There are a number of general multibody dynamics packages available that could be used for this type of modelling. ADAMS [1], Vortex [87] and

MatLab SimMechanics [6] for example are commercially available products which build numerical models of a system and typically supply tools for contact detection, terrain modelling and modelling of vehicle components such as joints and actuators. ROAMS [74] is a package used at JPL built specifically to deal with the modelling of various designs of planetary rovers. A key requisite of the the GMDL software however was that easy access to entities such as the mass matrix, constraint Jacobian, force, centrifugal and Coriolis terms for example, be granted to the user, at any time-step throughout the time integration of a simulation. While it was built for a very specific purpose, the software is generic and can work with any rigid multibody system. For an extensive overview of the structure of the library, the reader is referred to [29]. An overview of some of the pertinent features in the code however, are discussed here.

Each body entered as part of a system that will undergo simulation, is specified with inertial properties such as mass and moments of inertia. A local frame for each body is also defined. The position and orientation of the body with respect to the global frame of the simulation environment are recorded, as are the initial velocities of the body. The array of generalized coordinates at the position level for any given body in the system, \mathbf{q} is composed of as follows:

$$\mathbf{q}_i = \begin{bmatrix} x_{Gi} \\ y_{Gi} \\ z_{Gi} \\ e_{0i} \\ e_{1i} \\ e_{2i} \\ e_{3i} \end{bmatrix} \quad (4.1)$$

These seven coordinates consist of the three translational displacements x, y, z of the centre of mass G , of body i , in the global frame, along with four Euler-Rodriguez parameters consisting of the vector \vec{e} and the scalar e_0 for which the reader is referred to [39, 69]. The vector \vec{e} can be expressed with respect to a frame as the algebraic vector $[e_1, e_2, e_3]^T$. The generalized velocities however consist of the three translational velocities of the CoM $[\dot{x}_G, \dot{y}_G, \dot{z}_G]$, and three angular

velocities $[\omega_x, \omega_y, \omega_z]$, of each body. The relationship between the derivative of the position level coordinates and the generalized velocities is then:

$$\begin{bmatrix} \dot{x}_{Gi} \\ \dot{y}_{Gi} \\ \dot{z}_{Gi} \\ \dot{e}_{1i} \\ \dot{e}_{2i} \\ \dot{e}_{3i} \\ \dot{e}_{0i} \end{bmatrix} = \underbrace{\begin{bmatrix} \mathbf{I}_{3 \times 3} & \mathbf{0}_{3 \times 3} \\ \mathbf{0}_{4 \times 3} & \frac{1}{2} \begin{bmatrix} e_{0i} \mathbf{I}_{3 \times 3} + \tilde{\mathbf{E}}_i \\ -\mathbf{e}_i^T \end{bmatrix} \end{bmatrix}}_{\mathbf{N}_i} \begin{bmatrix} \dot{x}_{Gi} \\ \dot{y}_{Gi} \\ \dot{z}_{Gi} \\ \omega_{xi} \\ \omega_{yi} \\ \omega_{zi} \end{bmatrix} \quad (4.2)$$

where \mathbf{I} is the identity matrix, \mathbf{e} is the algebraic vector (array) $[e_1 \ e_2 \ e_3]^T$ and $\tilde{\mathbf{E}}$ is the crossproduct matrix of \mathbf{e} . The bodies composing the system, are connected via any of a number of possible kinematic constraints predefined in the library code, such as revolute and prismatic joints for example. The local frames of each body are key tools for specifying the location of these joints on each respective body. The constraints are expressed in the library code at the velocity level as:

$$\mathbf{\Gamma}(\mathbf{q})\dot{\mathbf{q}} + \mathbf{b}(\mathbf{q}, t) = 0 \quad (4.3)$$

where $\mathbf{\Gamma}$ is the $m \times n$ constraint Jacobian for a system with n degrees of freedom and m constraints, and \mathbf{b} is the $m \times 1$ array of time dependent constraint terms. For an overview of the mathematical expression of these types of constraint relationships, the reader is referred to [69]. With these parameters defined, the forces that will act on the system throughout the simulation are initialized, so that they may evolve as the simulation progresses. With this information, the dynamic equations of motion can be assembled. The GMDL offers a number of possible formulations to accommodate this part of the simulation. Options include direct solution of the equations of motion, solution of the equations of motion using Lagrange multipliers with Baumgarte stabilization [14], penalty formulations [15, 37], the augmented Lagrangian formulation [15], the augmented

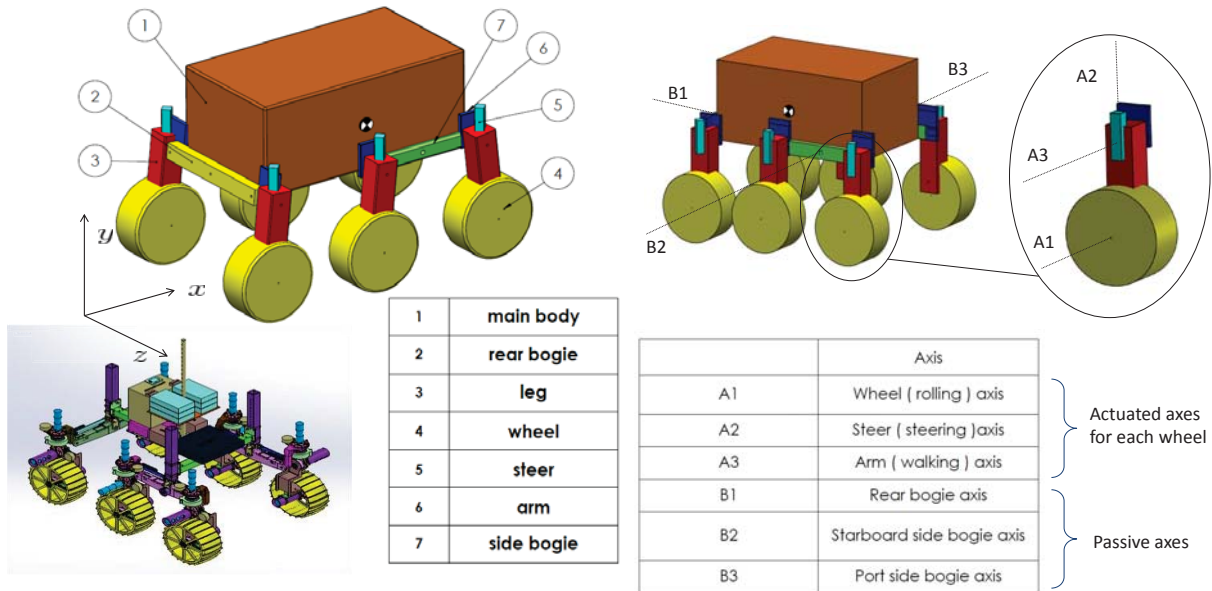
Lagrangian formulation with mass orthogonal projections [16] and a formulation involving a projection method of solution [57]. Most of these formulations and their implementation into time discretized algorithms for numerical solution, are described in [24]. The dynamic equations are then integrated using one of either the forward Euler, or trapezoidal schemes [68]. The data of interest is then stored for examination, and graphical representation of the results. Certain features of a simulation are automatically provided. For example, a body representing the ground is predefined in each program. For wheeled systems, interaction with the ground can be expressed with kinematic constraints referred to as “wheel-terrain” or “wheel-ground” constraints. These constraints, which can be interpreted as a type of mechanical joint between the rolling body and surface beneath, enforce contact with the simulated ground so that no sinking and or slipping of the wheel is permitted. Another interpretation of the terrain is achieved with the modelling of contact forces such as the normal and tangential forces developed by wheel-terrain interaction. Such forces can be developed with continuous force models, some of which will be discussed in the next chapter. As modelling of rovers in unstructured soft-soil terrain is an important element of the library code, several terramechanics models are also available for use when modelling terrain with different constitutive properties. Once the system properties, initial conditions, constraint relationships and applied forces are assembled, the system of dynamic equations is constructed, and can be solved with whichever of the integration schemes, and multibody formulations best suit the analysis. For the simulation of impact discussed in this thesis, a contact detection algorithm was developed and added to the library. The details of this algorithm will be discussed in Chapter 5. The test subject for most of these impact simulations is a model of the existing rover prototype built by the robotics and automation division of MacDonald Dettwiler and Associates (MDA), the Rover Chassis Prototype (RCP). The RCP was also the subject for a set of experiments discussed in Chapter 6 and Appendix D, used to validate simulations with the numeric model described in Chapter 5. The development of a parametric rover model for the library code, which better accommodates change of the geometric parameters, configuration and position of the system, is also discussed and compared to the RCP.

4.1 Rover Chassis Prototype (RCP)

The RCP was built by MDA in approximately 2005 as a test platform for planetary rover mobility and performance evaluation, and as a possible prototype for the European Space Agency's (ESA) planned mission to put the ExoMars rover on Mars. It consists of a main body suspended on six wheels through three passively rotating bogies. The bogie suspension system is similar to the characteristic JPL rocker bogie style of suspension, which allows the rover increased stability in obstacle climbing and rough terrain, by permitting more wheels to maintain contact with the uneven ground. The three bogies were originally linked with a pantograph linkage in a design classified as the RCL-E suspension system described in [86, 58]. At the time this linkage had been considered to be the optimal passive suspension design, but due to stability issues occurring on terrain sloped beyond a certain angle, that were observed later on, the linkage was later disabled. The RCP has a footprint of 1 m long by 0.9 m wide. It has actuators facilitating six-wheel-drive and six-wheel-steer capabilities. A third mode of locomotion involves articulation of all six legs in a wheel-walking motion. The walking option also provides a reconfigurable suspension, but actively controlled in this case. An advantage of this is the ability to shift the centre of mass of the rover and also to aid with inducing traction between the wheels and terrain in soft, low cohesion material such as sand. This concept is explored in [89]. The RCP is equipped with six force-torque sensors located in each of its legs. These sensors read the force and moment about the three orthogonal axes of the local leg frame. Encoders are located on each of the wheels, steering drives, and walking drives. Force, torque and angular velocity measurements can be recorded, along with the voltage and current drawn by each of the motors, so that a time history of the kinematic and dynamic behaviour of the rover can be profiled.

The model of the RCP was developed as a subject for experimental analysis with the McGill library code, in 2013. The mass and geometric properties were drawn from a CAD solid model of the RCP supplied by MDA. For simplification, the complex solid model was represented as 28 distinct, rigid bodies. The 28 bodies consist of the main body of the rover, three bogies rotating passively about the main body, six "steers" on which the steering actuators were based, six "arms"

which incorporate the “walking” rotation, six “legs” which hold the wheel driving actuators and six wheels. Axes of rotation of the model are depicted in Fig. 4–1b. To define all relevant aspects



(a) Top: the MatLab model of the RCP with individual bodies listed. Bottom: the Solid Works model of the RCP, courtesy of MDA.

(b) The MatLab model of the RCP with joint and locomotion axes depicted.

Figure 4–1: Models of the RCP.

of the rover, the model of the RCP was defined in two MATLAB scripts that are a part of the GMDL. The first script defined the physical properties of the rover such as: the inertial properties of each of the 28 bodies, the global positions of each centre of mass and the local positions of the joints on each body that connected it to successive components of the system. To transfer data efficiently from the Solid Works CAD model to the GMDL model, the local frame of each body corresponds to its counterpart in the CAD model. The second script defines the nature of the mechanism, or more specifically, the types of joints that connect the bodies of the system together. These joints are modelled as kinematic pairs for which the mathematical relationships used to represent them follow the methods described in [69]. For the rover models, these consisted mostly of revolute joints between rotating bodies such as wheel axles, that produce articulation and motion in the rover. Constraints such as the wheel-ground constraints described above, are implemented separately, as they do not describe constraints that are part of the rover mechanism, but rather a

relationship between the rover and its environment. These two scripts provide an initial state that is standard for a typical simulation with the RCP. They are then passed on to the main script of the program for numerical integration of the dynamic equations of motion. Naturally if alterations to the RCP, such as changes to its geometry or initial orientation and position are required, some changes in the initial scripts will be necessary. Since for the purposes of expedience and fidelity to the CAD model of the RCP, each position and orientation was hardcoded into the defining scripts, changes to positions or dimensions in the model can require extensive alteration to the input scripts. A change in the length of the side bogies for example would require a stretching of the rover, which would potentially shift the positions of the front wheels, legs, arms and steering joints, as well as the side bogies themselves. This limitation gives rise to the need for a parametrically defined rover, where the positions of the majority of the bodies are defined based on a select few parameters.

4.2 The Parametric Rover

Since the impact simulations required that various parameters of the rover be altered systematically, using the RCP model for this proved to be a cumbersome task due to the inflexible format of the input scripts. An additional incentive to model a rover more suited to quick changes in dimension and linkage, arose when MDA assumed responsibility for building the electro-mechanical subsystem (chassis) for the upcoming ESA ExoMars rover mission tentatively scheduled for launch in 2018. The ExoMars rover in the design phase had a design similar to the RCP. Since the ExoMars design was still underway, and features were changing as the design evolved, a rough outline of the rover could easily be set up using the parametric rover model, leaving the finer points to be filled in once these details were more concrete. To parametrize the RCP, any number of relationships between the bodies of the system can be used, and based on a few select input parameters. In Fig. 4-2, a diagram illustrating the parametrization of the rover model, some commonly chosen input parameters are displayed at the top of the figure. These consist of the walking angle, the wheel base, and the wheel track. The walking angle θ , is the angle at which the leg is rotated with respect to the bogie of the rover. The wheel base is the centre to centre distance between the front and rear wheels, when the walking angle is zero. The wheel track is the distance between the outer faces

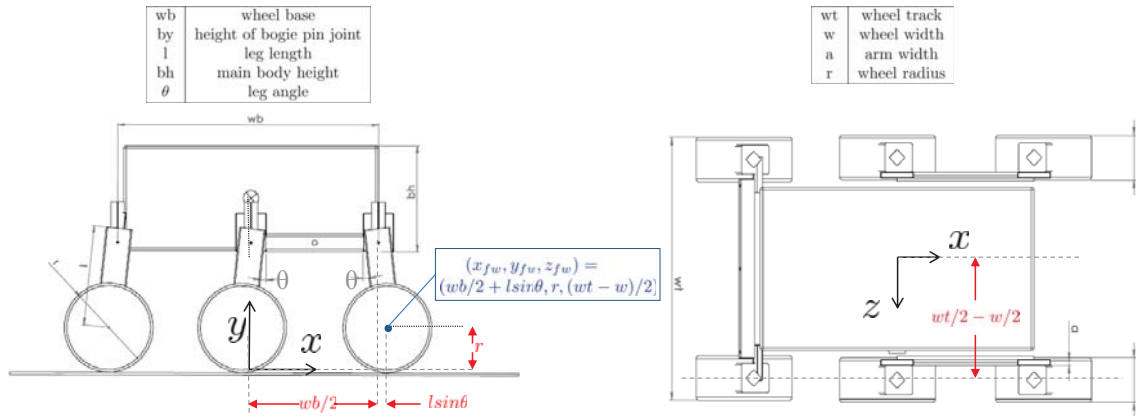


Figure 4–2: A selection of possible input parameters for the parametric rover

of the wheels on each side of the rover. Along with these entries, the wheel width and radius, the width of the rover arm, and global y coordinate of the bogie joint when the walking angle is zero are also chosen as input parameters. An example of a simple parametrization for simulation using these parameters, is given in Table 4–1 (only the starboard half of the rover is listed for simplicity).

The first column in the table lists the CoM of the body that is being parametrized. The middle column lists the numeric values of the global x, y, z coordinates of the corresponding CoM, as it is input into the scripts of the RCP rover model. The last column lists the same position (approximately), but in parametric form. The position is only approximate in order to keep the parametric relationship simple and general, so the parametric rover model is a rough estimate of the exact RCP model. Entries in black denote the input parameters, blue entries are values based on parametric equations of the input parameters and/or other blue entries. The values in red correspond to the red values in Fig. 4–2, as an example of how the given set of parametric equations are derived. The fidelity of the parametric equations to the actual model, can be developed to a greater or lesser degree as the user wishes, at the cost of simplicity in the parametric relationships.

Table 4–1: RCP body position vectors and corresponding parametric rover parameters.

	Body	RCP	Parametric rover
		CoM Location (x,y,z)	CoM Location (x,y,z)
1)	front wheel (<i>fw</i>)	(0.5349, 0.175, 0.4552)	$(wb/2 + l\sin\theta, r, (wt - w)/2)$
2)	middle wheel (<i>mw</i>)	(0.0, 0.175, 0.4552)	$(-l\sin\theta, r, (wt - w)/2)$
3)	rear wheel (<i>rw</i>)	(-0.5381, 0.175, 0.4552)	$(-wb/2 - l\sin\theta, r, (wt - w)/2)$
4)	front leg (<i>fl</i>)	(0.5349, 0.2214, 0.3872)	$(x_{fw} - l\sin\theta/2, y_{fw} + l\cos\theta/2, z_{fw})$
5)	middle leg (<i>ml</i>)	(0.0053, 0.2214, 0.3872)	$(x_{mw} + l\sin\theta/2, y_{mw} + l\cos\theta/2, z_{mw})$
6)	rear leg (<i>rl</i>)	(-0.5307, 0.2214, 0.4506)	$(x_{rw} + l\sin\theta/2, y_{rw} + l\cos\theta/2, z_{rw})$
7)	front steer (<i>fs</i>)	(0.5391, 0.4711, 0.4662)	$(x_{fl} - l\sin\theta, by, z_{fl})$
8)	middle steer (<i>ms</i>)	(0.0046, 0.4711, 0.4662)	$(x_{ml} + l\sin\theta, by, z_{ml})$
9)	rear steer (<i>rs</i>)	(-0.5423, 0.4711, 0.4662)	$(x_{rl} + l\sin\theta, by, z_{rl})$
10)	front arm (<i>fa</i>)	(0.5279, 0.06200, 0.4091)	$(x_{fs}, by, z_{fs} + (a - w)/2)$
11)	middle arm (<i>ma</i>)	(0.0070, 0.6200, 0.4091)	$(x_{ms}, by, z_{ms} + (a - w)/2)$
12)	rear arm (<i>ra</i>)	(-0.5315, 0.6200, 0.4030)	$(x_{rs}, by, z_{rs} + (a - w)/2)$
13)	side bogie (<i>sb</i>)	(0.2671, 0.4499, 0.3290)	$((x_{fa} + x_{ma})/2, by, z_{mw})$
14)	rear bogie (<i>rb</i>)	(-0.5385, 0.4501, 0.0)	$(x_{ra}, by, 0)$
15)	Main Body (<i>mb</i>)	(-0.0014, 0.8246, 0.0)	$(x_{mw} + l\sin\theta/2, by + bh/2, 0)$

4.3 The ExoMars-Like Rover

The ExoMars rover is part of a project commissioned by the ESA to explore Mars for signs of ancient life. The rover is tentatively scheduled to leave for Mars in 2018, following the launch of a trace gas orbiter in 2016. The orbiter's mission will be initially to search for pockets of methane and other trace gasses that would possibly arise from the decomposition of organic matter, and then to support communications for the ExoMars rover. The ExoMars rover will land at a location where the probability of finding ancient life is high, and the engineering risks involved in landing are low. At the time of writing the proposed destination is Oxia Planum. Equipped with a variety of scientific instruments, known as the Pasteur scientific sweet, ExoMars will be capable of drilling for subterranean samples at a maximum depth of two meters [10]. As with other Mars rovers, full autonomy with respect to navigation and negotiation of unstructured terrain is necessary. The model of ExoMars is very similar to that of the RCP. The main design differences other than differing overall dimensions, are that the order of locomotion, namely the walking and steering actuators, are reversed. In the ExoMars rover, the steering actuators are mounted on the walking

actuators, and thus move with the walking angle of the leg. The ExoMars rover also has a simpler bogie system called the three bogie suspension system which was the successor after the RCL-E suspension model used with the RCP was demonstrated to be unstable on steeper slopes. The three bogie model has proven in test situations to be as effective and as stable as the traditional JPL rocker bogie system but with the added advantage of being slightly lower in mass [72]. A final difference between ExoMars and past rovers in general is the addition of flexible wheels. These wheels with outer and inner stiffness given by folded bands of metal in the wheel hub, will assist the three bogie system with maximizing traction by maintaining a larger contact patch between the wheel and the terrain [26, 47]. As the ExoMars rover was still in the design phase at the time of writing, only certain proposed component designs were available to the McGill rover team for the purposes of the modelling of an “ExoMars-like” rover. Components that had been developed were part of what was referred to as the Bogie Electro Mechanical Actuation (BEMA) assembly. The BEMA assembly consisted of the wheels, the rear and side bogies, two brackets to house the actuators and a model of the actuator used for all 18 driven degrees of freedom. These images are listed in Fig. 4–3 where in all except for number 7 (the actuator), the named component within its assembly, is highlighted in yellow. Data available to the McGill team along with these images,

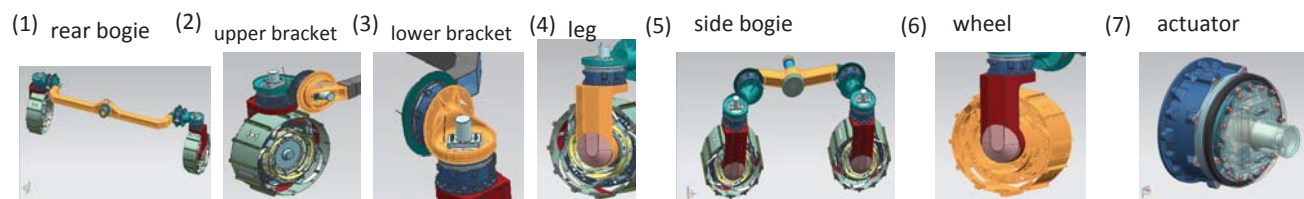
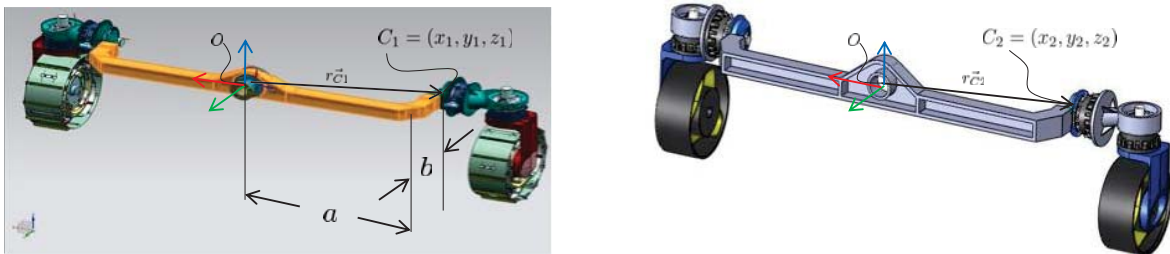


Figure 4–3: Components of the BEMA subassembly.

were some inertial properties and some position vectors. From this, the locations and dimensions of the bodies had to be ascertained, in order to produce a full model for simulation with an ExoMars-like rover (ELR). For the purposes of documentation, a description of the development of the ELR model will be outlined in the remainder of this section.

To begin with, each of the components illustrated in the available BEMA images were initially modelled in Solid Works based solely on the visual properties of the corresponding component images. While the dimensions of the components were not explicitly available, some inertial properties and centre of mass (CoM) positions accompanied the component images with respect to a visible Solid Works origin marked on the rear bogie assembly image. The dimensions of the components could then be estimated roughly by matching the CoMs of the ELR solid model with corresponding CoM data from available BEMA images. As an example of these estimations, consider Fig. 4–4a which shows the complete BEMA rear bogie assembly. The image consists of: one rear bogie frame, two upper brackets, two lower brackets, six actuators, two leg frames and two wheels.



(a) BEMA rear bogie assembly proposed for the ExoMars rover. (b) McGill representative solid model of the proposed BEMA rear bogie assembly

Figure 4–4: ExoMars rear bogie assembly.

The origin provided is depicted with red, green and blue axes, at the centre of the rear bogie frame denoting the x,y and z axes respectively. The components modelled for the ELR were then assembled in the same manner in Solid Works, with a coincident origin. The x,y and z components of the position vectors for one of the upper brackets for example (image two in Fig. 4–3) were given in millimeters as: $[-548, -248, -28]^T$. This location is shown at point C_1 in Fig. 4–4a. Dimensions such as “a” and “b” however were unspecified. To determine these dimensions the ExoMars-like bodies were assembled in the same manner, so that the centre of mass for the ELR

upper bracket (shown at C_2 in Fig. 4–4b) could be evaluated using Solid Works. More specifically, once the rear bogie is modelled approximately in Solid Works, the coordinates of any point on the model can be retrieved from the program, which is how C_2 is determined. The rear bogie would then be stretched or shrunk to align the x component of this centre of mass (x_2) so that it would be close to the corresponding centre of mass (x_1) in the supplied data. After some trial and error, when the CoMs correspond to within a reasonable tolerance, the dimension “a” could be evaluated in the solid model of the assembly. A similar process could be performed with the y component of the CoMs of the bracket and dimension “b”. Since in most cases the position of local origins of individual components were not provided, the moments of inertia were used to determine the most likely orientation of the local axes of each part. Finally some dimensions such as the wheel radius available from [72] were used to stand in where the data couldn’t be reliably conjectured from the information supplied. In this manner, the ExoMars-like rover was modelled for the purposes of dynamic simulation with the generic multibody dynamic library code. The full solid model of the ELR is shown in Fig. 4–5 with a main frame that connects the bogie assemblies drawn into the model to represent components to be built and designed by other contractors participating in the ExoMars rover mission.

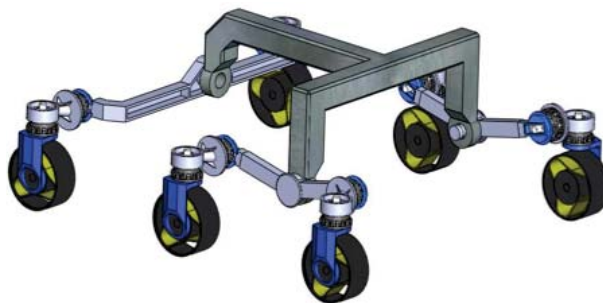


Figure 4–5: McGill model of an “ExoMars-like” like rover.

With the solid model of the ELR finalized, some reorganization of the data was necessary to transfer the information from the Solid Works environment into the Matlab based environment in which the GMDL global frame is defined. Initially, all components in the solid model had to be regrouped and organized as bodies for the kinematic chain. The individual inertial properties of

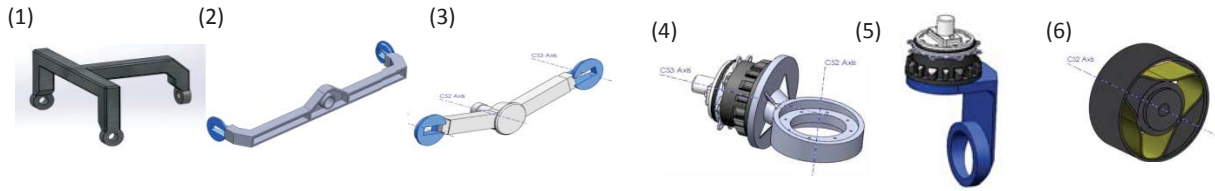


Figure 4–6: McGill models of ExoMars-like rover parts.

Table 4–2: Grouping of bodies for the numeric ExoMars-like model.

1)	main body	1 main body
2)	rear bogie	1 rear bogie and 2 upper brackets
3)	side bogie	1 side bogie and 2 upper brackets
4)	arm	1 lower bracket and 1 actuator
5)	leg	1 leg and 1 actuator
6)	wheel	1 wheel and 1 actuator

each component were combined to form six categories of bodies for the ELR dynamic simulation model, namely: the main body, the rear bogie, the side bogie, the arm, the leg and the wheel. These are essentially the same as the bodies used for the RCP excluding the steer which, for the ELR linkage, was eliminated for simplicity. Images of these assemblies are shown in Fig. 4–6, and Table 4–2 lists the components that make up each assembly.

The combined mass properties of each of these components were then transformed from the Solid Works global frame to the the GMDL local frame. This required that transformations be performed on moments of inertia provided in the original BEMA Solid Works frames to bring them into the Matlab orientations. It was decided that for ease of comparison of information, it would be useful to have the local frames of the ELR coincide with the corresponding RCP body fixed frames. To this end, the BEMA data had to be transformed so that it was expressed with respect to the correct frame. Where data was unavailable, conjectured data developed in the Solid Model of the ELR was used to fill in missing gaps in the information. An example of the transformations performed on each body to relate the BEMA data to the current ExoMars-like GMDL model, is outlined below using the ELR leg to demonstrate.

According to Table 4–2, the leg assembly consists of one actuator and one leg bracket, for which the individual, centroidal moments of inertia had been provided. These components had to

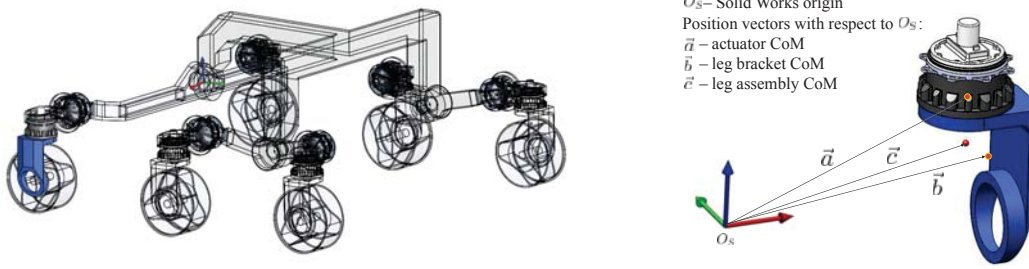


Figure 4-7: McGill solid model of the ELR with focus on the leg assembly.

be combined to produce the moments of inertia of the leg assembly for the Matlab model of the leg. The position vector of each component with respect to the total centre of mass of the assembly is found referring to the vectors \vec{a} , \vec{b} and \vec{c} in Fig. 4-7 such that:

$$\vec{r}_a = \vec{a} - \vec{c} \quad \vec{r}_b = \vec{b} - \vec{c} \quad (4.4)$$

These individual centroidal moments of inertia, now had to be evaluated with respect to the CoM of the full leg assembly. The evaluation of the data can be expressed with the coordinate free notation of Steiner's theorem [33] shown below.

$$\hat{\mathbf{I}}_{leg} = \hat{\mathbf{I}}_a + m_a[(\vec{r}_a \cdot \vec{r}_a)\hat{\mathbf{E}}_3 - \vec{r}_a \otimes \vec{r}_a] + \hat{\mathbf{I}}_b + m_b[(\vec{r}_b \cdot \vec{r}_b)\hat{\mathbf{E}}_3 - \vec{r}_b \otimes \vec{r}_b] \quad (4.5)$$

where $\hat{\mathbf{E}}$ is the identity tensor. The subscripts a and b represent in this case, the actuator and leg bracket respectively. The terms m_i and $\hat{\mathbf{I}}_i$ and are the mass and inertia tensor of the i^{th} component, where i refers to either a or b . $\hat{\mathbf{I}}_{leg}$ is the desired output of the moments of inertia of the full leg assembly. The difference between Solid Works and GMDL frames is illustrated in Fig. 4-8. The figure shows the orientation and position of the frames in each environment with the red, green and blue colours again denoting the x,y and z axes respectively. The position vector of any point P is \vec{p}_1 when originating from O_S , and \vec{p}_2 when originating from O_G , where O_S and O_G are the origins of frames S and G respectively, and are joined by the vector \vec{r} . Then translation from one vector to the other is

$$\vec{p}_2 = \vec{p}_1 - \vec{r} \quad (4.6)$$

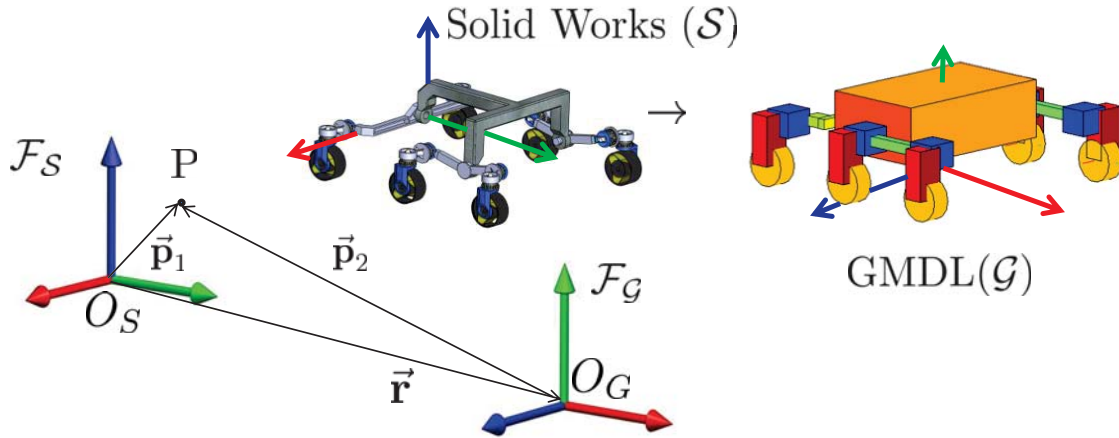


Figure 4–8: Illustration of transformation from Solid Works to GMDL frames.

To transform a vector expressed in Frame \mathcal{S} to coordinates expressed in Frame \mathcal{G} , a rotation tensor $\hat{\mathbf{R}}$, having the relationships

$$\vec{\mathbf{e}}_{s1} = \hat{\mathbf{R}}\vec{\mathbf{e}}_{g1} \quad \vec{\mathbf{e}}_{s2} = \hat{\mathbf{R}}\vec{\mathbf{e}}_{g2} \quad \vec{\mathbf{e}}_{s3} = \hat{\mathbf{R}}\vec{\mathbf{e}}_{g3} \quad (4.7)$$

can be used. In Eq. (4.7), $\vec{\mathbf{e}}_{s1}$, $\vec{\mathbf{e}}_{s2}$ and $\vec{\mathbf{e}}_{s3}$ express the unit vectors of the axes of Frame \mathcal{S} , and $\vec{\mathbf{e}}_{g1}$, $\vec{\mathbf{e}}_{g2}$ and $\vec{\mathbf{e}}_{g3}$ express the unit vectors of the axes of Frame \mathcal{G} . The transformation can then be expressed with respect to the relevant frames as:

$$\mathbf{p}_2^{(g)} = \mathbf{R}^{(s)T} \mathbf{p}_2^{(s)} \quad (4.8)$$

where $\mathbf{p}_2^{(g)}$ is the algebraic vector expressing $\vec{\mathbf{p}}_2$ in terms of the GMDL frame and $\mathbf{p}_2^{(s)}$ expresses $\vec{\mathbf{p}}_2$ in terms of the Solid Works frame. The combined moments of inertia for each body can undergo this same coordinate transformation, plus an additional transformation between the GMDL global and local frames. This can be done with an additional transformation matrix \mathbf{L} which is specific to the coordinate frame of each body. Both transformations are expressed below separately for clarity as:

$$\mathbf{I}_{leg}^{(g)} = \mathbf{R}^{(s)T} \mathbf{I}_{leg}^{(s)} \mathbf{R}^{(s)} \quad \mathbf{I}_{leg}^{(l)} = \mathbf{L}^{(g)T} \mathbf{I}_{leg}^{(g)} \mathbf{L}^{(g)} \quad (4.9)$$

Here the superscripts “s” and “g” indicate whether the matrix is expressed with respect to the Solid Works (s) or the GMDL global (g) frames, while “l” indicates specifically the GMDL local frame. The 3×3 matrix \mathbf{L} represents the transformation matrix bringing the moments of inertia of each body expressed in the GMDL global frame to expression in the GMDL local frame.

The final MATLAB model of the ExoMars-like rover has 22 bodies: a main body, 3 bogies, 6 arms, 6 legs and 6 wheels. The wheel base and wheel track dimensions were listed in [72] as 1.26 m by 1.31 m respectively. Using the supplied BEMA data, the solid model of the ExoMars-like rover shows a wheel track of closer to 1.45 m. The wheel base dimension was difficult to estimate with the information provided, but was scaled upwards to maintain the same proportion to the wheel track. The standard simulations run with the ELR such as step climbing, obstacle negotiation and impact, show results fairly similar to that of the RCP due to their similar construction and dimensions. Some simulation results are displayed in Chapter 5.

CHAPTER 5 Impact Simulations

Before discussing the specifics of the impact simulations performed with the rover models and the library code, some background on contact, continuous force models, and a description of the contact models included in the library is outlined here.

5.1 Contact Models

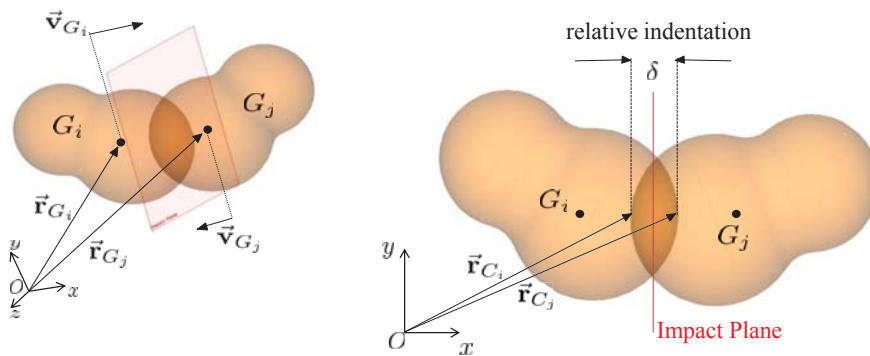


Figure 5–1: Diagram of collision of bodies i and j .

Consider the two colliding bodies in Fig 5–1 travelling with centre of mass velocities \vec{v}_{G_i} and \vec{v}_{G_j} with respect to the fixed frame. The position vectors on each body of the expected initial contact points are denoted \vec{r}_{C_i} and \vec{r}_{C_j} . At the instant that these contact points meet, the impact (or contact) plane, is the plane tangential to both the surfaces of body i and body j , and coincident with the point of contact. Realistically, the bodies will compress and deform about this point with no interpenetration, and the contact points on each body, will not pass through the impact plane. This deformation increases through what is termed the compression phase, until the maximum point of compression is reached. The contact can be modelled however, by considering the bodies to be undeformed and evaluating the degree of indentation, or overlapping (δ as depicted in Fig. 5–1) that would occur if interpenetration were permitted instead. If this model is used, at the onset of contact, the contact points C_i and C_j have non-zero relative velocity in the direction normal to

the impact plane. This velocity is referred to as the relative velocity of indentation. The bodies continue to approach each other until the end of the compression phase, known as the instant of maximum approach, is reached and deformation of the bodies stops. At this instant, the relative velocity of indentation, which is the time derivative of δ , becomes zero. The bodies then begin to recede, and the degree of indentation reduces. This phase is known as the phase of restitution, in which the bodies regain a relative velocity of indentation as they recede from the contact. This continues until separation between the bodies occurs and contact is lost. In order to evaluate the post impact state of the system, a momentum or energy balance of pre- and post-impact values can be performed. In most cases, some energy in the system will be lost, due to phenomena such as internal damping and vibration of the contacting bodies. The evaluation of exactly how much energy is lost is a difficult task, requiring an intricate knowledge of the system constitution and geometry. A parameter frequently used to supplement the available information however, so that exiting velocities can be determined, is the coefficient of restitution e , which was initially defined by Newton as the ratio of the relative indentation velocity at the instant of separation, to the relative indentation velocity at initial contact. Empirically derived values for a material dependent constant, α , were developed by Goldsmith [34] to approximate e in the following relationship:

$$e = 1 - \alpha \dot{\delta}^{(-)} \quad (5.1)$$

where $\dot{\delta}^{(-)}$ is the relative velocity of indentation the instant before impact occurs. Equation 5.1 has been shown to hold with reasonable accuracy for low impact velocities, and a coefficient of restitution close to unity. Other definitions of the coefficient of restitution such as that proposed by Poisson [75] for example, which relates pre- and post-impact impulse, have been defined. Stronge [84] targets energy loss directly with an energetic coefficient of restitution that measures the square root of the ratio of the elastic strain energy released during the restitution phase, to the energy, absorbed during the compression phase with the deformation of the contacting bodies. Using the coefficient of restitution, the degree of indentation, and its time derivative, various models that characterize the contact force applied to body i by body j and vice versa, have been proposed. Such

modelling is referred to as continuous force modelling. The simplest of these is the Kelvin-Voight model [34], a linear visco-elastic model of the form:

$$f_{KV} = k\delta + b\dot{\delta} \quad (5.2)$$

where f_{KV} is the contact force produced, δ and $\dot{\delta}$ are the degree of relative indentation and its time derivative, and k and b are spring and damping constants related to the material and geometric properties of the system. Hunt and Crossley argued in [42] that this linear visco-elastic model didn't accurately reflect the nonlinear nature of a general contact force. Instead they based the contact on the founding work of Hertz [40, 50], who studied the forces developed between two spheres in static contact and developed the foundation for contact theory with the contact force model:

$$f_{Hz} = k\delta^p \quad k = \frac{4}{3\pi(h_i + h_j)} \left[\frac{R_i R_j}{R_i + R_j} \right]^{1/2} \quad h_m = \frac{1 - \nu_m^2}{\pi E_m} \quad (5.3)$$

Here the exponent p is related to the geometry of the bodies in contact, found by Hertz to be $3/2$ for two contacting spheres. The variable m takes values of either i or j , and parameters ν and E are Poisson's ratio and Young's modulus of bodies i and j . This contact model was extended to account for dissipative effects and defined the form on which many succeeding visco-elastic models are based as:

$$f = k\delta^p + b\delta^n\dot{\delta} \quad (5.4)$$

As the stiffness coefficient, k , and the coefficient of restitution, can be determined either analytically or experimentally [34, 50], most of these models are characterized by their definition of b the damping factor of the system. A comparison of the different models of the damping factor for many of the contact models discussed here is covered in [92]. The method of determining b developed by Hunt and Crossley [42], and used later by Lankarani and Nikravesh [60] in a similar model, was achieved with work-energy principles, by integrating about the hysteresis loop described by the contact force as a function of displacement, to determine the energy loss of the impact. The validity of several assumptions made by these two models depend on the conditions of

low impact velocities, and a coefficient of restitution close to unity. The nonlinear contact models are expressed as:

$$f_{HC} = -k\delta^p \left[1 + \frac{3(1-e)}{2} \frac{\dot{\delta}}{\dot{\delta}_i^{(-)}} \right] \quad (5.5)$$

$$f_{LN} = -k\delta^p \left[1 + \frac{3(1-e^2)}{4} \frac{\dot{\delta}}{\dot{\delta}_i^{(-)}} \right] \quad (5.6)$$

where f_{HC} and f_{LN} are the contact forces developed by the Hunt and Crossley [42], and the Lankarani and Nikravesh [60] models respectively, e is the coefficient of restitution described by Eq. (5.1), and $\dot{\delta}_i^{(-)}$ is the velocity of relative indentation at the onset of contact. As an alternative to the use of the work-energy principle, Lee and Wang [62] developed a contact model that solves for the damping factor through the solution of the equation of motion:

$$m_{eff}\ddot{\delta} + b\delta^n\dot{\delta} + K\delta^p = 0, \quad m_{eff} = \frac{m_i + m_j}{m_i m_j} \quad (5.7)$$

where m_{eff} is the effective mass of the two-particle model, and m_i and m_j are the masses of bodies i and j respectively. The Lee and Wang [62] contact model is:

$$f_{LW} = -k\delta \left[1 + \frac{3(1-e)}{4} \frac{\dot{\delta}}{\dot{\delta}_i^{(-)}} \right] \quad (5.8)$$

Finally, another model included in the library that solves for b through the solution of Eq. (5.7) introduced by Gonthier et al [35], defines the damping coefficient b as:

$$b = \frac{kd}{e_{eff}} \quad \frac{1 + d/e_{eff}}{1 - d} = e^{d(1+1/e_{eff})} \quad (5.9)$$

The variable d introduced in this formulation, is solved for in the second expression of Eq. (5.9), using a bisection algorithm, and the value e_{eff} is distinguished as the effective coefficient of restitution in the event that the colliding bodies are of different materials. The effective coefficient of restitution is given by the relationship $e_{eff} = -\dot{\delta}^{(+)} / \dot{\delta}^{(-)}$, where $\dot{\delta}^{(-)}$ and $\dot{\delta}^{(+)}$ are the relative indentation velocities before and after impact. In this work, the contact model and the damping

factor are found to be:

$$f_G = -k\delta^p \left(1 + \frac{d}{e_{eff}} \frac{\dot{\delta}}{\dot{\delta}^{(-)}}\right) \quad b = \frac{kd}{e_{eff}\dot{\delta}^{(-)}} \quad (5.10)$$

where f_G is the contact force developed by the Gonthier et al [35] contact model. This model has been shown to produce accurate results for a greater range of coefficients of restitution than the Hunt and Crossley [42], and the Lankarani and Nikravesh [60] models.

For impact simulations with the RCP and Exomars rover models, the velocities were low, and the coefficient of restitution was usually close to one. The Hunt and Crossley [42] model was most commonly used as the contact model of choice for the impact simulations that are described in the remainder of the chapter. A comparison between simulations with different coefficients of restitution and different continuous force models at the end of this chapter however, demonstrates the validity of this choice for the purposes of this thesis.

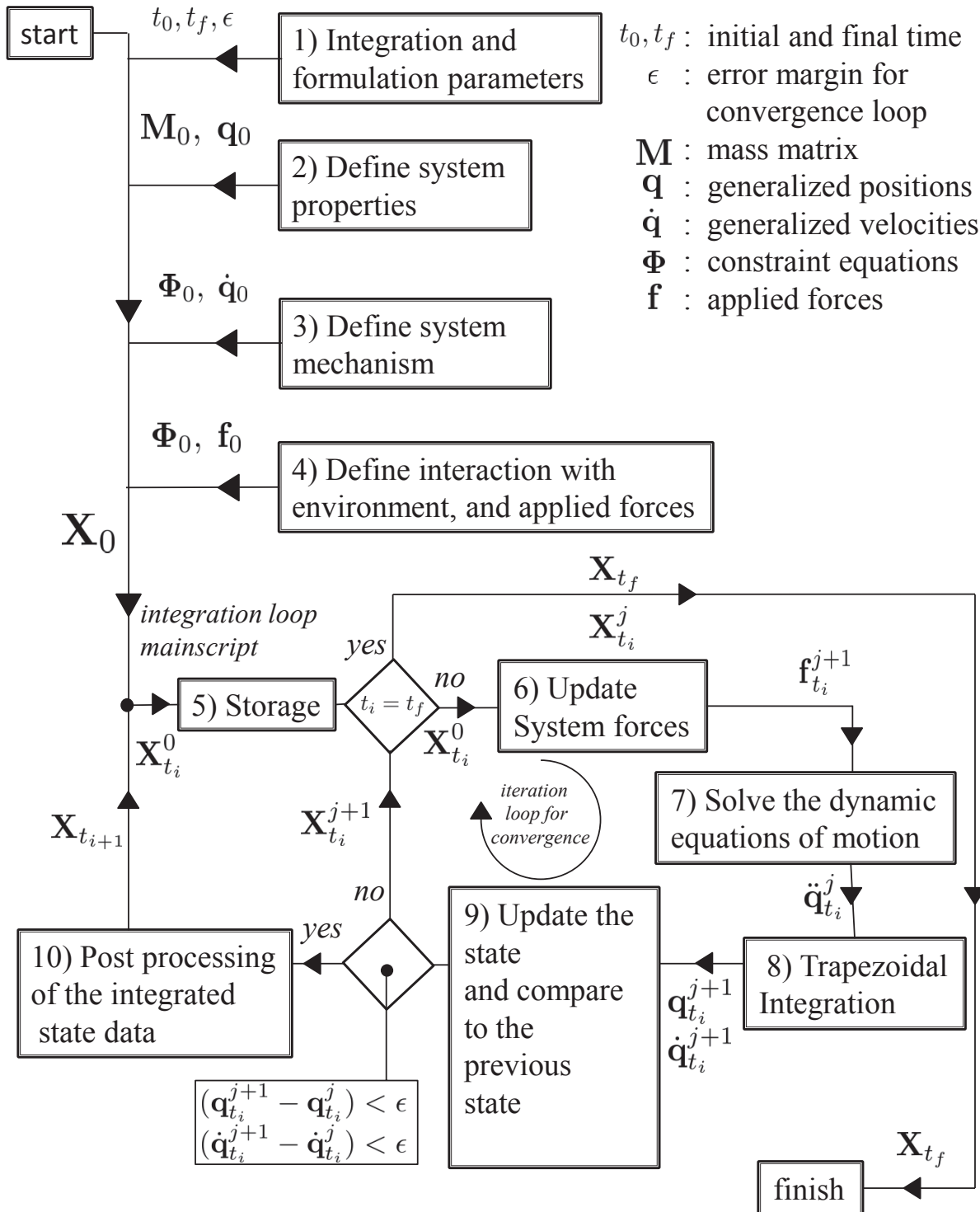


Figure 5–2: Data flow through a typical multibody dynamics simulation using the GMDL library functions. $\mathbf{X}_{t_i}^j = t_i, \mathbf{q}_{t_i}, \dot{\mathbf{q}}_{t_i}, \Phi_{t_i}, \mathbf{f}_{t_i}, \mathbf{M}_{t_i}$ among other state and program variables and parameters. Index “j” is the iteration index for a given time step of index “i”.

5.2 Impact Simulations

For the analysis of impact and the validation of the effective kinetic energy performance indicator, the generic multibody dynamics library was used in conjunction with one or other of the rover models (RCP or Exomars) to run a variety of impact simulations. While the full explanation for the dynamic simulation is given in [29], an explanation of the code sections pertinent to the impact simulations is given here. The simulations consist of the rover approaching and contacting an obstacle, modelled as a plane, located at a given position and rotated to a given angle (β) of inclination with respect to the fixed frame. In all simulations, the contacting bodies of the rover

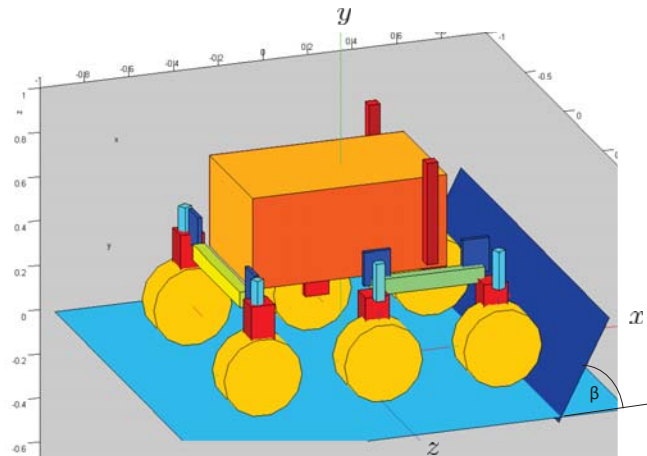


Figure 5–3: RCP Impact Simulation.

system are the front wheels. Each simulation consists of three phases: a free motion phase, a compression phase and a restitution phase. The first phase includes the rover as it moves freely through its environment; a flat surface representing the terrain beneath the rover, modelled either with kinematic or dynamic relations depending on the particulars of the impact analysis. A contact detection algorithm detects when contact has been made between the rover and the plane. At the instant of contact, the effective kinetic energy is determined, and the contact model is activated to develop a full profile of the contact force as the rover moves through the successive phases of

compression and restitution. At the end of the compression phase, the time step of maximum approach is reached, and the maximum contact force throughout the force profile is recorded. This maximum contact force does not necessarily fall at the deepest part of the impact, as when dissipation is included in the contact model, the force is dependent on the relative indentation velocity as well as the relative indentation. The maximum force does however fall at or before the point of maximum approach. The restitution phase then begins and the simulation may be terminated at any point from this point on, or be used to double check that the data produced is feasible. This simulation is run for a range of values for β to see how this impact configuration effects impact force and effective kinetic energy. Figure 5–2 shows a schematic of the flow of data throughout the course of a typical simulation using the library programs. Each numbered block specifies a particular function or group of functions called in a typical simulation, and the details of these blocks specific to impact simulations are listed below.

1) Program Integration and Formulation Parameters. The initial part of any multibody simulation with the GMDL determines various parameters associated with integration and the solutions of the equations of motion. For a typical impact simulation the trapezoidal scheme for numerical integration was used for its simplicity and accuracy sufficient for the purposes of these simulations. The chosen formulation for solving the equations of motion was the augmented Lagrangian with mass orthogonal projections.

2,3) Define system properties and define mechanism: As discussed in Chapter 4, these programs have been built into the library for dealing with the RCP and parametric rovers. They outline the physical, inertial and kinematic properties of the pertinent rover system.

4) Define interaction with the environment: This portion of the code initializes forces and external constraints that will act on the system. For example, in most rover simulations the force of gravity is defined here. In the case of impact, the contact forces that will be applied to the two front wheels of the rover upon impact with the obstacle, are initialized. As the simulation begins with the rover moving in the “free motion” stage, this impact force is set to zero, and is activated once contact is made with the impact surface. The wheel-terrain interaction, whether it is represented

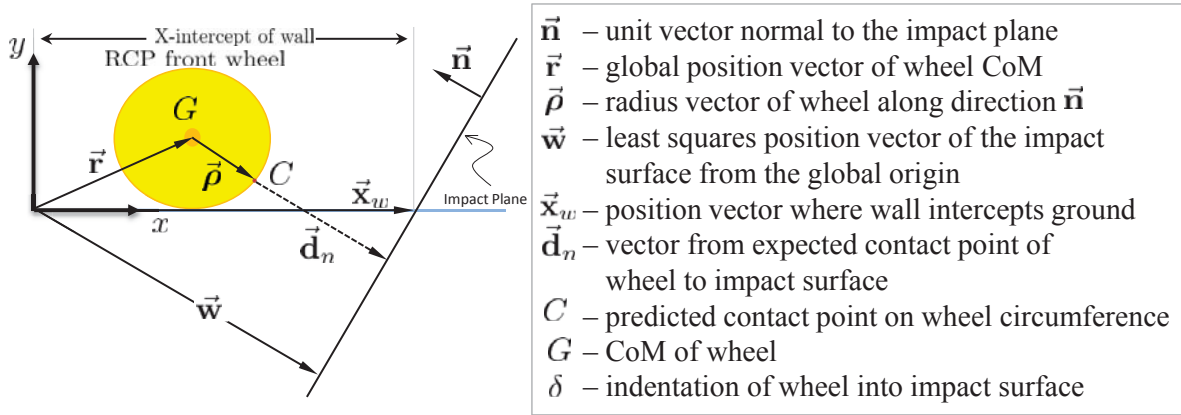


Figure 5–4: Contact detection.

with kinematic constraints, or with constitutive force models, is also initialized in this section. For impact simulations, both these representations were explored, and will be discussed further later on in the Chapter.

One last feature of this environmental interaction code block with respect to impact simulations, is the definition of the location and rotation of the impact surface. The impact surface is defined through the point at which it intersects the ground, (x_w in Fig. 5–4) and an angle of rotation about the z axis (since for these simulations motion of the rover was confined mostly to the x-y plane). This data is saved in a structure, which facilitates the impact detection algorithm coded in the Update Forces function.

6) Update Forces: This block of code updates forces and constraints that have been initialized in block four. For impact simulations the Update Forces function is where the impact detection algorithm is implemented. The algorithm projects the position vector of the front wheels of the rover onto a line that is normal to the impact surface and intersects the global origin shown as vector \vec{w} in Fig. 5–4. The relative indentation of the wheel into the impact surface δ is determined as follows:

$$\vec{d} = \vec{w} - (\vec{r} + \vec{\rho}) \quad (5.11)$$

$$\vec{d}_n = (\vec{d} \cdot \vec{n})\vec{n}, \quad \delta = \vec{d}_n \cdot \vec{n} \quad (5.12)$$

where \vec{r} is the position vector of the wheel with respect to the global origin and \vec{n} is the unit vector directed normal to the impact surface. The vector $\vec{\rho}$ has the magnitude of the wheel radius, and originates from the centre of the wheel. It is directed along the line normal to the impact plane as shown in Fig. 5–4. Vector \vec{w} connects the global origin with the impact surface intercepting the surface at 90° . The vector \vec{d}_n joins the predicted contact point on the wheel (C), with the impact plane also intersecting at 90° . The scalar value δ has the magnitude of \vec{d}_n and goes from negative to positive as wheel moves from the free motion phase (where wheel and impact plane are separate) to the compression phase of the impact. During each calling of the Update Forces function, the value δ is re-evaluated and fed into a continuous force model, typically the Hunt and Crossley model, to produce f_{HC} in Eq. (5.5). The contact force produced is evaluated independently for each wheel and then directed along \vec{n} , originating from the contact point C in Fig. 5–4. Once the updated forces and contact points have been determined, various sub-functions in the library arrange the resulting forces and moments on each body of the rover in the applied generalized forces array. These are used to solve the system of dynamic equations represented by block 7 in Fig. 5–2). Additionally, by monitoring δ for each iteration, a conditional loop within the Update Forces function evaluates the effective kinetic energy once contact has been made. This event occurs when the value δ transitions from a negative to positive.

The remaining blocks of code displayed in Fig. 5–2 are generic and have no specific features related to the impact simulations. Once the simulation is complete, the values of interest are the maximum contact force, and the effective kinetic energy value determined upon impact.

5.3 The Evaluation of Effective Kinetic Energy

In Chapter 3, the expression for effective kinetic energy for a system of n bodies was given as:

$$T_c = \frac{1}{2} \dot{\mathbf{q}}^T \mathbf{J}_c^T (\mathbf{J}_c \mathbf{M}^{-1} \mathbf{J}_c^T)^{-1} \mathbf{J}_c \dot{\mathbf{q}} \quad (5.13)$$

This can also be expressed as:

$$T_c = \frac{1}{2} \mathbf{v}_c^T (\mathbf{J}_c \mathbf{M}^{-1} \mathbf{J}_c^T)^{-1} \mathbf{v}_c \quad (5.14)$$

with the relationship $\mathbf{J}_c \dot{\mathbf{q}} = \mathbf{v}_c$. For the two-body example, the SCM was parametrized by \mathbf{v}_c the velocity of the contact point of the front wheel moving in a direction normal to the impact plane. The SCM however is also augmented by the constraints of the system such as those arising from mechanical joints that connect the bodies of the system together. Because the two-body model was described with independent coordinates, information about these constraints is included implicitly within the mass matrix and the equations of motion. In the case of the RCP however, the system is described with a set of dependent coordinates introduced at the beginning of Chapter 4. The 28 bodies each described with 6 coordinates at the velocity level result in a 168×168 mass matrix. The velocities of the contact points, in this case the contact points on the two front wheels, can be achieved with the transformation

$$\mathbf{\Lambda} \dot{\mathbf{q}} = \mathbf{v}_c \quad (5.15)$$

where $\dot{\mathbf{q}}$, the velocities of each of the 28 bodies of the RCP in this case, can be written as:

$$\dot{\mathbf{q}} = \begin{bmatrix} \dot{\mathbf{q}}_{fs} \\ \dot{\mathbf{q}}_{fp} \\ \dot{\mathbf{q}}_r \end{bmatrix} \quad \dot{\mathbf{q}}_f = \begin{bmatrix} \dot{x}_f, \dot{y}_f, \dot{z}_f, \dot{\theta}_{x_f}, \dot{\theta}_{y_f}, \dot{\theta}_{z_f} \end{bmatrix}^T \quad (5.16)$$

The subscripts fs and fp refer to the front starboard and front port side wheels, which comprise the first 12 velocities in the array of 168 entries, and are generalized to the subscript f for either front wheel. The angular velocities of the wheel about each of the x , y and z axes are denoted by $\dot{\theta}_x$, $\dot{\theta}_y$ and $\dot{\theta}_z$ respectively. The subscript r refers to the remainder of the bodies of the system that are not involved in the transformation of Eq.(5.15). The matrix $\mathbf{\Lambda}$ is derived from the relationships:

$$\begin{aligned} \dot{x}_{C_f} &= \dot{x}_{G_f} - R\dot{\theta}_{C_f} \sin\theta_{C_f} \\ \dot{y}_{C_f} &= \dot{y}_{G_f} + R\dot{\theta}_{C_f} \cos\theta_{C_f} \end{aligned} \quad (5.17)$$

$$v_{C_f} = \dot{x}_{C_f} \cos\theta_{C_f} + \dot{y}_{C_f} \sin\theta_{C_f} = (\dot{x}_{G_f} - R\dot{\theta}_{C_f} \sin\theta_{C_f}) \cos\theta_{C_f} + (\dot{y}_{G_f} + R\dot{\theta}_{C_f} \cos\theta_{C_f}) \sin\theta_{C_f} \quad (5.18)$$

In Eqs (5.17) and (5.18) the subscripts G and C represent respectively: the centre of mass location, or the location of the point on the wheel which contacts the impact plane, as is depicted in Fig.

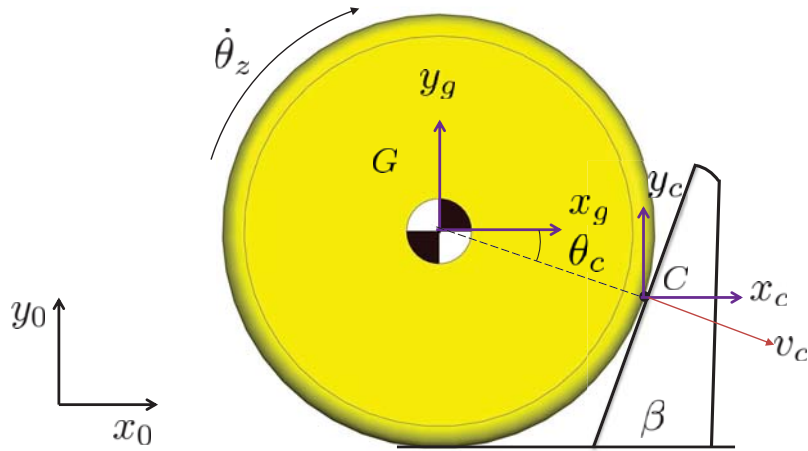


Figure 5–5: Front wheel contact point reference frame.

5–5. The subscript f signifies that the relationships exist for both front starboard and front port side wheels. These relationships are analogous to the transformations with \mathbf{G} and \mathbf{R}_c in Chapter 3. In this case, a full transformation by \mathbf{G} from $\dot{\mathbf{q}}$ into the intermediate set of coordinates π is not determined, as only the parametrization for the SCM need be defined for the evaluation of effective kinetic energy. With the substitution of the kinematic relationships:

$$\theta_{C_f} = -(90 - \beta), \quad \dot{\theta}_{C_f} = \dot{\theta}_{z_f} \quad (5.19)$$

where β is the angle of inclination of the impact plane in degrees, the coordinates of \mathbf{v}_C can then be written as:

$$v_{C_f} = (\dot{x}_{G_f} + R\dot{\theta}_{z_f}\cos\beta)\sin\beta - (\dot{y}_{G_f} + R\dot{\theta}_{z_f}\sin\beta)\cos\beta = \dot{x}_{G_f}\sin\beta - \dot{y}_{G_f}\cos\beta \quad (5.20)$$

Here v_{C_f} represents the two identical constraints for the front starboard and port side wheels. Thus the final form of $\mathbf{\Lambda}$ can be written as :

$$\mathbf{\Lambda} = \begin{bmatrix} \sin\beta & -\cos\beta & 0 & 0 & 0 & 0 & \mathbf{0}_{1 \times 6} & \mathbf{0}_{1 \times 156} \\ & \mathbf{0}_{1 \times 6} & \sin\beta & -\cos\beta & 0 & 0 & 0 & \mathbf{0}_{1 \times 156} \end{bmatrix} \quad (5.21)$$

The constraints however that tie the whole system together are in this case expressed with explicit constraint equations which were given in Chapter 4, Eq (4.3) as:

$$\mathbf{\Gamma}(\mathbf{q})\dot{\mathbf{q}} + \mathbf{b}(\mathbf{q}, t) = 0 \quad (5.22)$$

In many cases, and in the case of the impact simulations with the RCP, the constraints are scleronomous, and so the time dependent term drops out, reducing the equation to:

$$\mathbf{\Gamma}\dot{\mathbf{q}} = \mathbf{0} \quad (5.23)$$

For the sake of clarity, it is worth distinguishing at this point between the subspace of motion that is constrained by relationships inherent in the system, and the SCM, as the similar nomenclature can be confusing. The first subspace is spanned by the vectors of the constraint Jacobian $\mathbf{\Gamma}$. For a generic system described by the library code, a system of n bodies will result in $6n$ dependent velocities, with m constraints. The matrix $\mathbf{\Gamma}$ will be of dimension $m \times 6n$. Since there is no motion associated with this subspace, there is also no kinetic energy associated with this subspace, as motion in these directions is prohibited by the physical connections (such as mechanical joints) of the system. The second subspace, the SCM, is a subspace that has been isolated, being of interest to the analyst. This subspace in impact situations is a subspace in which motion is constrained by the presence of impact surfaces on bodies external to the system, or colliding bodies within the system. Such impacts impede the motion of the system in these “constrained” directions. The energy associated with these subspaces however, is typically not zero. To accommodate the evaluation of effective kinetic energy with dependent coordinates, one method of constructing the SCM Jacobian transformation matrix \mathbf{J}_c is to compose it as follows:

$$\mathbf{J}_c = \begin{bmatrix} \mathbf{\Gamma} \\ \mathbf{\Lambda} \end{bmatrix} \quad (5.24)$$

The evaluation of the effective kinetic energy where dependent coordinates are used can now be expressed as:

$$T_c = \frac{1}{2} \dot{\mathbf{q}}^T \begin{bmatrix} \mathbf{\Gamma}^T & \mathbf{\Lambda}^T \end{bmatrix} \left(\begin{bmatrix} \mathbf{\Gamma} \\ \mathbf{\Lambda} \end{bmatrix} \mathbf{M}^{-1} \begin{bmatrix} \mathbf{\Gamma}^T & \mathbf{\Lambda}^T \end{bmatrix} \right)^{-1} \begin{bmatrix} \mathbf{\Gamma} \\ \mathbf{\Lambda} \end{bmatrix} \dot{\mathbf{q}} \quad (5.25)$$

In the event that Eq.(5.23) is true, the equivalence of the evaluation of effective kinetic energy with and without the use of the constraint Jacobian depending on what type of coordinates are used is discussed in Appendix (B).

For the RCP the size of \mathbf{J}_c varies depending on the nature of the simulation, as the number of constraints expressed in $\mathbf{\Gamma}$ depends on how the terrain is modelled. The structure of \mathbf{J}_c is illustrated in Fig. 5–6 where rows 1 to 238 constitute the rows of the RCP constraint Jacobian $\mathbf{\Gamma}$, and rows

1 – 24	[{Wheels to ground :	<i>6 sets of 4 wheel – terrain constraint equations</i>
25 – 54		{Wheels to legs :	<i>6 sets of 5 revolute joint constraint equations</i>
55 – 84		{Legs to steers :	<i>6 sets of 5 revolute joint constraint equations</i>
85 – 114		{Steers to arms :	<i>6 sets of 5 revolute joint constraint equations</i>
115 – 144		{Arms to bogies :	<i>6 sets of 5 revolute joint constraint equations</i>
145 – 159		{Bogies to body :	<i>3 sets of 5 revolute joint constraint equations</i>
160 – 238		{All :	<i>26 sets of revolute joint lock constraint equations</i>
239 – 240		{Front wheels :	<i>2 sets of 1 equation for direction normal to impact plane</i>

Figure 5–6: A schematic representation of the SCM, RCP Jacobian \mathbf{J}_c .

239 and 240 constitute the rows of $\mathbf{\Lambda}$ the Jacobian for the direction of interest. The majority of the relationships in $\mathbf{\Gamma}$ represent the revolute joints between bodies, such as the steering and the walking joints. A revolute joint between two bodies is described by five constraint equations [69, 29]. Additionally, locking constraints (which are described with one or three equations depending on the type of constraint), are available for each of the revolute joints in the case where the relative motion of the revolute joint is not desired. Throughout most of the impact simulations for example, the wheel walking and steering joints remain locked. Another set of constraints corresponding to the kinematic constraints introduced in Section 4.1 and are used in some simulations to model the wheel-ground interaction. These constraints are described with four equations and comprise the first 24 rows of $\mathbf{\Gamma}$. The size of the constraint Jacobian depends on whether or not these constraints

are active, as will be discussed in the following sections. As a result, the constraint Jacobian Γ usually has between 214 to 238 rows, and 168 columns.

5.4 Modelling the Ground

A manner in which this thesis extends the research in [36], is with the exploration of different methods for representing the terrain beneath the rover in simulations with the RCP. The two main models for wheel-terrain interaction that were explored, implemented either constraint relationships or constitutive contact force models. The first of these methods is kinematic, whereas the second attempts to model contact forces developed between the terrain and the wheels of the rover. The second method can be achieved using any of a number of available contact models which may or may not consider the presence of friction. The methods are described below and results are displayed in Section 5.5.

Kinematic Constraints: In Fig. 5–6, the first 24 equations of the constraint Jacobian for the RCP impose relationships between the six wheels of the rover and the underlying terrain, that characterize the unilateral relationship between each wheel and the ground (or the rolling surface) beneath it. The constraints used are a set of generic constraints from the GMDL library, which can con-

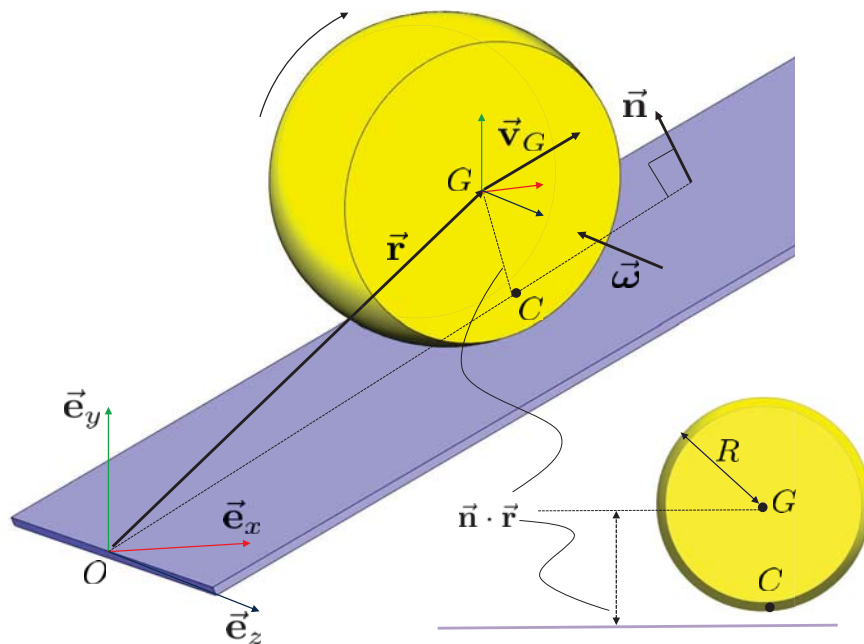


Figure 5–7: Illustration of the wheel-terrain constraints for a rolling body.

strain a rolling body to roll on a defined plane without sinking into it or lifting away from it. This is illustrated in Fig. 5–7, where the geometric vector $\vec{\mathbf{n}}$ represents the unit vector normal to the surface on which the body rolls, and the vector $\vec{\mathbf{r}}$ represents the position vector of the CoM of the rolling body with respect to the global frame originating at O . The dot product $\vec{\mathbf{n}} \cdot \vec{\mathbf{r}}$ gives the magnitude of the component of $\vec{\mathbf{r}}$ that is in the direction of the rolling surface normal $\vec{\mathbf{n}}$. This product is constrained to equal the distance between the CoM of the rolling body (G), and the expected rolling plane contact point on the surface of the body (C), which in the case of the RCP wheel is R the wheel radius. This condition is modelled with the holonomic constraint Φ , expressed below with its time derivative $\frac{d\Phi}{dt}$ as:

$$\Phi = \mathbf{n}^T \mathbf{r} - R = 0 \quad (5.26)$$

$$\frac{d\Phi}{dt} = \frac{\partial\Phi}{\partial x} \dot{x} + \frac{\partial\Phi}{\partial y} \dot{y} + \frac{\partial\Phi}{\partial z} \dot{z} + \frac{\partial\Phi}{\partial t} = n_x \dot{x} + n_y \dot{y} + n_z \dot{z} = 0 \quad (5.27)$$

In Eq.(5.26), the arrays \mathbf{n} and \mathbf{r} are the algebraic vectors containing the scalar components of the vectors $\vec{\mathbf{n}}$ and $\vec{\mathbf{r}}$ respectively. The constraint is scleronomic implying that the term $\partial\Phi/\partial t$ is equal to zero. Additional to maintaining the contact without sinkage between the rolling body and the rolling plane, the wheel-terrain constraints also maintain rolling without slip on the rolling surface. The constraint, being generic, will constrain rolling about any axis parallel to the rolling surface. This model is appropriate for the simulation of rolling with the RCP wheels, as the wheels are domed and so have a curvature allowing a rolling motion about more than one axis. In the case of the impact simulations with the RCP however, rolling about any axis other than the axis of the wheel shaft is never generated, thus in Fig. 5–7, the angular velocity vector $\vec{\omega}$ is shown to be parallel to the wheel axis, which for the impact simulations remains parallel to the global z axis. To regulate rolling, three non-holonomic relationships are used to relate the translational velocity of the CoM of the rolling body, ($\vec{\mathbf{v}}_G$ in Fig. 5–7), to the angular velocity ($\vec{\omega}$) of the body. If the generalized velocity vector $\dot{\mathbf{q}}_i$ of the rolling body i , is decomposed into translational and angular velocity components such that $\dot{\mathbf{q}}_i = \left[\dot{x}_G \quad \dot{y}_G \quad \dot{z}_G \quad \omega_x \quad \omega_y \quad \omega_z \right]^T = [\mathbf{v}_G^T \quad \boldsymbol{\omega}^T]^T$, then the three

velocity level rolling constraint equations can be expressed as:

$$\mathbf{v}_G + R\tilde{\mathbf{N}}\boldsymbol{\omega} = \mathbf{0} \quad (5.28)$$

Here \mathbf{v}_G and $\boldsymbol{\omega}$ are the algebraic vectors containing the scalar components of vectors $\vec{\mathbf{v}}_G$ and $\vec{\boldsymbol{\omega}}$, and $\tilde{\mathbf{N}}$ is the crossproduct matrix formed from the scalar components of $\vec{\mathbf{n}}$. With the GMDL, the ground is represented by the x - z plane. In this case $\mathbf{n} = [0, 1, 0]^T$, and the three kinematic constraints of Eq. (5.28) enforcing rolling without slip at the velocity level appear as:

$$\mathbf{J}_w \dot{\mathbf{q}}_i = \begin{bmatrix} 1 & 0 & 0 & 0 & 0 & R \\ 0 & 1 & 0 & 0 & 0 & 0 \\ 0 & 0 & 1 & -R & 0 & 0 \end{bmatrix} \begin{bmatrix} \dot{x}_G \\ \dot{y}_G \\ \dot{z}_G \\ \omega_x \\ \omega_y \\ \omega_z \end{bmatrix} = \begin{bmatrix} 0 \\ 0 \\ 0 \end{bmatrix} \quad (5.29)$$

where \mathbf{J}_w is the wheel-ground constraint Jacobian for one wheel. Equation (5.27), the time derivative of Eq. (5.26), is already expressed by Eqs. (5.28). The purpose of Eq. (5.26) however, is to constrain the motion of the body at the position level, or drifting of the position from the rolling surface can occur.

Like all the constraints represented by the full constraint Jacobian, the wheel-ground constraints expressed above are also used to model bilateral constraints, and will act as bilateral constraints if they remain active throughout the simulation. While this implies that the wheel cannot sink into the rolling surface beneath, it also means that it cannot lift away from it. The unilateral nature of the contact is achieved with the activation and deactivation of these constraints depending on the state of the wheel concerned. The constraints are active while the wheel remains in contact with the rolling surface, preventing any sinkage below the surface. Conversely, if the wheel lifts away from the surface or acquires a velocity that will move it away from the surface, the constraint

is deactivated. This process modifies Eq. (5.26) so that it effectively acts as:

$$\Phi = \mathbf{n}^T \mathbf{r} - R \geq 0 \quad (5.30)$$

throughout the simulation. For the impact simulations, these wheel-terrain constraints are all initially active, and either remain active or deactivate upon impact, depending on the angle of inclination of the impact plane. Simulation results involving the use of the wheel-ground constraints are displayed and further discussed in section 5.5.

Constitutive Modelling of Contact Forces: An alternative to the use of kinematic constraints was to model the ground with contact force models similar to those described in Section 5.1. Contact force models are more typically used to model rigid terrain, with some degree of compliance and damping depending on the material constitution involved. For soft soil, terramechanics provide a more appropriate model of the wheel-terrain interaction, however some of the characteristics of a soft terrain can also be approximated with contact force models, without introducing the extra factors of excessive dissipative effects and friction. While these factors must eventually be considered for the full evaluation of effective kinetic energy as a performance indicator for planetary rover contact situations, their direct effect on the performance indicator is beyond the scope of this thesis and is left for future research. To implement the contact force models, the position of the six rover wheels were tracked with respect to the plane representing the terrain surface, and the degree of penetration δ of each wheel into the surface was used to determine the opposing normal force. Since the RCP is initially positioned with its wheels sitting on the surface of the underlying terrain, a transient period where a degree of penetration representing sinkage of the rover wheels into the terrain must be established over the ensuing time steps, in order to elicit any reaction force from the terrain contact model. The stiffness constant of the contact model will effect the value of this sinkage that the rover will achieve in the terrain, and will produce oscillations in the vertical direction about the equilibrium sinkage position. The damping coefficient influences how quickly these oscillations will decay, and how fast the steady state response is achieved. Once the rover is rolling over the terrain in steady state, the impact simulation can proceed. Initially the contact

model chosen was the Kelvin-Voight linear visco-elastic model described in Section 5.1, giving the contact force f as:

$$f = k\delta + b\dot{\delta} \quad (5.31)$$

where k and b are stiffness and damping coefficients, and δ and $\dot{\delta}$ are the degree of penetration between the wheels and the ground, and the corresponding velocity of penetration. As pointed out previously, the Kelvin-Voight model is criticized for not correctly characterizing the nonlinear nature generally exhibited in the forces generated by contacting bodies. Another shortcoming in this model is that the half sine curve that is achieved by the model as the impact progresses through the compression and restitution phases of contact, implies that the instant before contact is made, a tensile force could be applied to the contacting bodies, which is not a realistic scenario. To improve the contact representation, nonlinear models of the ground were also used. The general nonlinear format as given in Section 5.1 is:

$$f = k\delta^p + b\delta^n\dot{\delta} \quad (5.32)$$

where n and p are both taken to be $3/2$ following the nonlinear contact models based on [42]. The values of k and b were varied to simulate ground composed of a variety of materials with different stiffness and damping characteristics.

5.5 Simulation Results

Simulation results demonstrating the similar trends between effective kinetic energy, and maximum impact force for varied impact configurations, are displayed in here for different simulations. In all plots the velocity of the rover upon impact is 7cm/s. For the preliminary simulations, kinematic constraints were used to model the terrain, however all constraints were removed at the instant of impact. While this is not a realistic simulation of the impact of the rover with an obstacle, it does give some insight into consequences of the collision that are not a result of the forces applied by the underlying terrain. This understanding is useful for later analysis of a more accurate representation of the impact.

The dependence of the two indicators on the angle of impact, and the location of the centre of mass of the rover are shown in Fig. 5–8 for both RCP and ExoMars-like models. In these

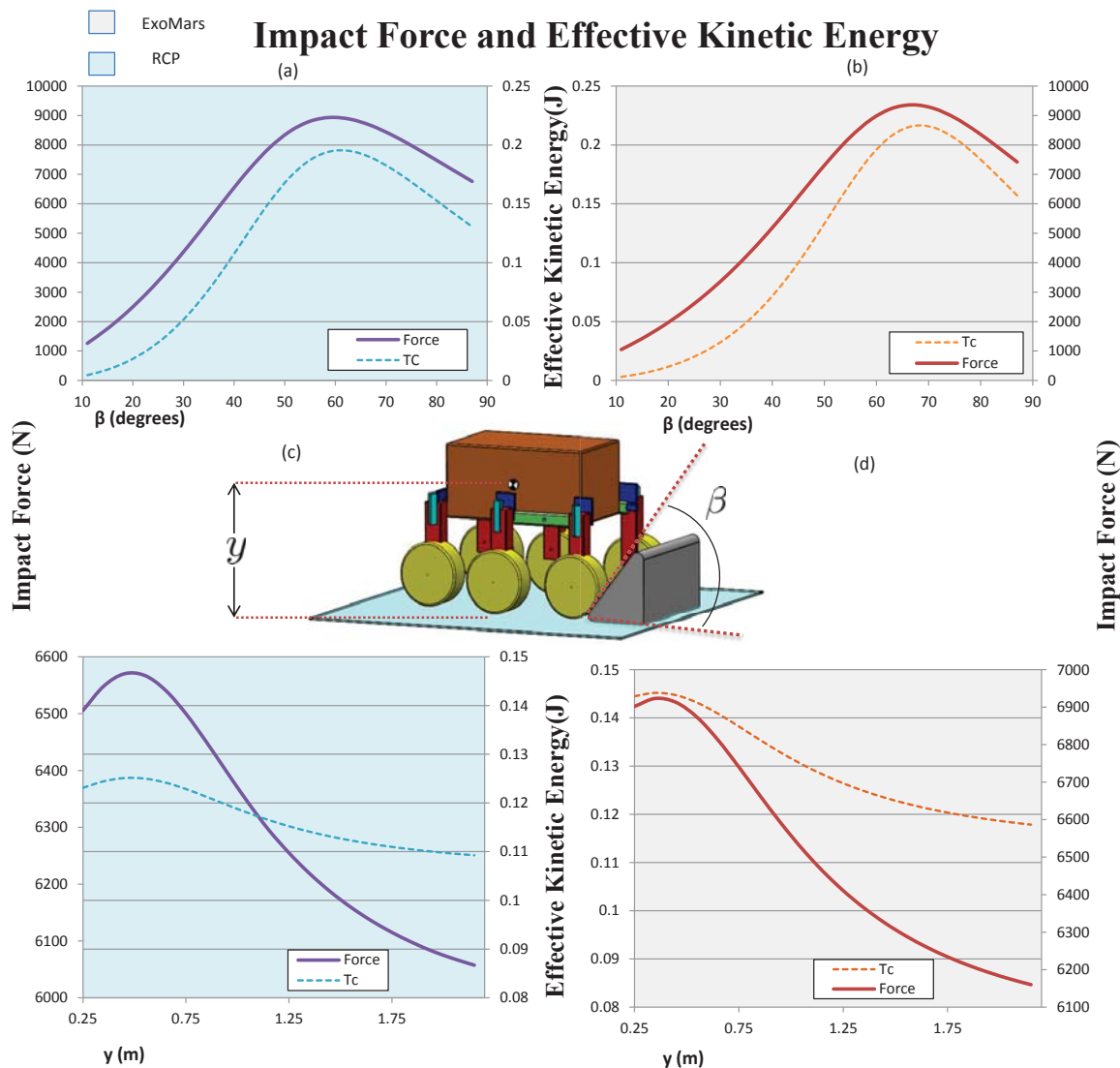


Figure 5–8: Top: RCP (a) and ExoMars-like (b) rover model plots of maximum impact force and effective kinetic energy plotted for a varying angle of impact (β). Bottom: RCP (c) and ExoMars-like (d) rover model plots of maximum impact force and effective kinetic energy plotted for a varying vertical position of centre of mass (y).

simulations, the angle of impact (β), was varied from 10° to 90° . A maximum value for both impact force and effective kinetic energy is achieved at about 60° for the RCP and 70° for the ExoMars-like rover. Differences are a result of the slightly different geometries of the two rover models such as the respective positions of the CoM, and of the pin joints of the bogies. The relationship between maximum impact force and effective kinetic energy with the vertical position of the CoM of the rover (y), is also plotted. In both plots, energy and force indicators are given separate axes

to display their separate values and units. The similar trend between the two indicators, is apparent in all four plots.

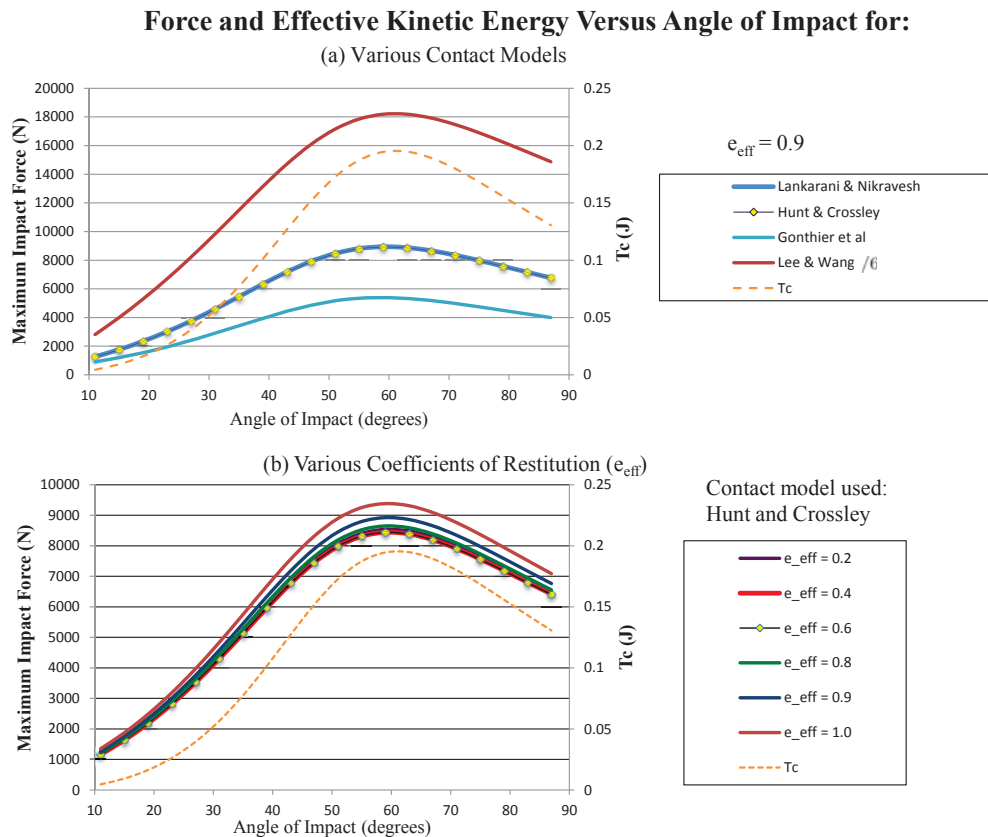


Figure 5–9: a) Effective kinetic energy and maximum impact force plotted using different contact models. b) Effective kinetic energy and maximum impact force plotted for a varying coefficient of restitution (e_{eff}).

Typically simulations were run with the well established Hunt and Crossley [42] contact model described in Section 5.1, for its simplicity and ease of implementation. This model works well for a coefficient of restitution close to unity. Plot (a) in Fig. 5–9 however, shows results with three alternative contact models also described in Section 5.1. The different contact models give varying magnitudes for maximum impact force related to each angle of impact. The trend of the curves however, remains the same. For most simulations the coefficient of restitution is kept close to unity, however varying the coefficient of restitution also does not alter the trend of the maximum impact force, as illustrated in Fig. 5–9, plot (b). Only the magnitude varies with the coefficient of restitution. In conclusion from these results, the effective kinetic energy is still a good predictor for

the trend displayed by the impact force as impact configuration is varied, regardless of the contact model or coefficient of restitution involved.

The implementation of the wheel-terrain relationship into the impact simulations, can change the results of the simulation depending on the properties of the terrain that is modelled. As discussed in Section 5.4, the terrain was represented both with kinematic constraints, and with contact force models. Results for modelling of the ground with kinematic relationships are displayed in Fig. 5–10. The plot shows the results of effective kinetic energy and impact force, plotted without interaction with the ground, as was displayed in Fig 5–8. Results with a kinematic model of the ground through the use of activating and deactivating wheel-terrain constraints as required however, are also displayed. The six constraints prohibiting penetration of the wheels into the ground, are switched on or off automatically depending on whether the wheels of the rover are lifting off the ground, or pushing into it throughout the simulation. Once the wheel-terrain constraint is activated, only a deviation of the wheels from the ground of close to machine precision is permitted, implying that the ground is perfectly hard, having an extremely high stiffness. The table in Fig. 5–10 displays how the constraints were altered at the onset of impact for different angles of impact plane inclination. This table shows how the constraints of each of the six wheels are behaving within 20 time steps (about 0.0002s) after impact occurs for impact angles from 10° to 90° . This delay allows some time for constraints which do not react immediately to the impact. For higher angles of 60° and up, the front wheels are pushing into the ground and so the constraints for these wheels are active, where as for lower angles, the front wheel constraints are inactive. The constraint activity for lower angles shows a similar trend to simulations where the ground is not modelled, implying that the contact force is not greatly affected by these middle and rear wheel-terrain relationships for this simulation set-up. For higher angles however, greater than 60° , the impact force is affected by the degree of mobility of the front wheels. With the front wheels almost immobilized by the presence of the wheel-terrain constraints, the contact force and consequently effective kinetic energy remain consistently at the maximum value, instead of dropping as the angle increases as in the case illustrated in Fig. 5–8. This behaviour can be viewed from the perspective of the effective

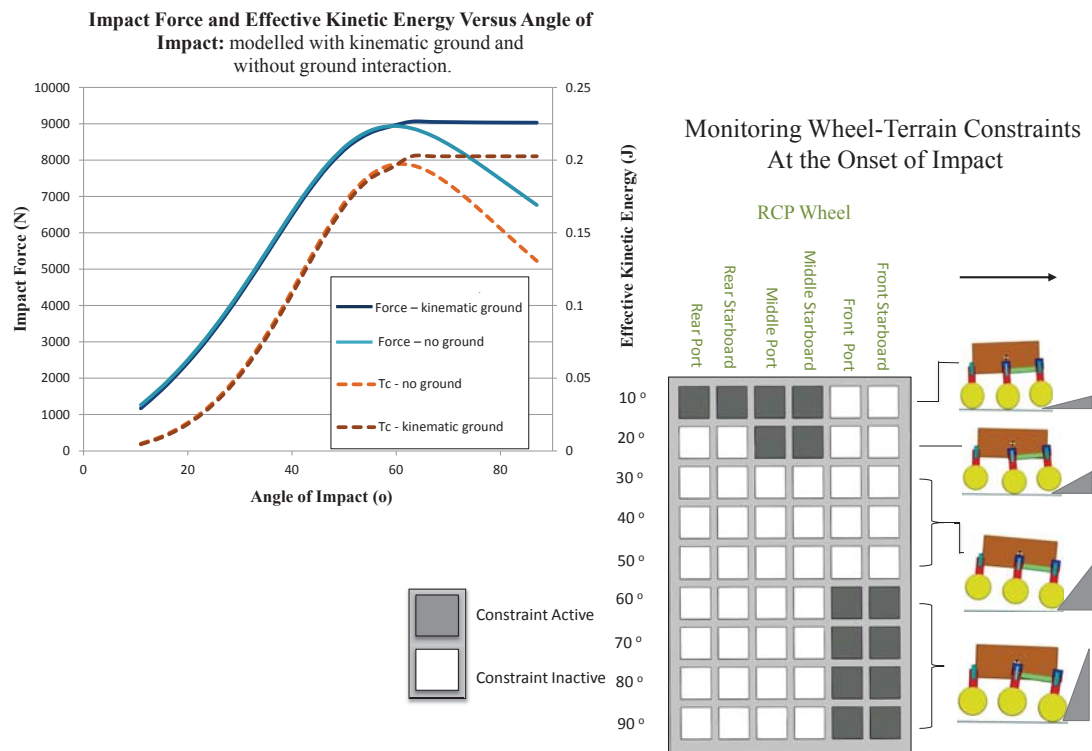


Figure 5–10: Activity of the kinematic, wheel-terrain constraints on each of the six wheels for a range of impact angles. A black square indicates the constraint for the corresponding wheel at the corresponding angle of impact, is active.

kinetic energy for these impact configurations. Consider the two-body model in Fig. 5–11, where impact with the front wheel and a planar surface occur at an angle of impact β . For each value of β , the effective kinetic energy will be different. The concept behind this was illustrated in Chapter 3, where impact for two-body systems having two different CoM positions were compared. In Fig. 5–11 the red arrows indicate the directions of constrained motion. Arrow (a) is a direction of constrained motion due to the impact surface, while arrow (b) is a direction of constrained motion due to the active wheel-ground constraint. The constraint equations representing these directions span the constraint space of the wheel and since they are linearly independent, they form a basis for the plane to which they both belong. Consequently, at the point of impact, all directions of the wheel in the plane of motion are constrained, and all of its kinetic energy will belong to the SCM. This will occur regardless of the angle β of the impact plane, as long as it is an angle which induces an active wheel-terrain constraint. Consequently, the effective kinetic energy value for all impact

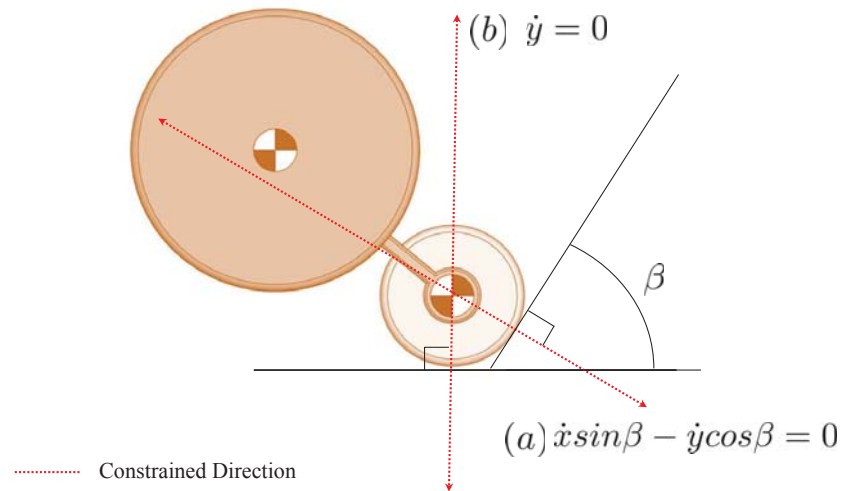


Figure 5–11: The constrained directions of the two-body system front wheel, impacting on an angled plane with wheel-ground constraints.

angles at which the contacting wheels have active wheel-terrain constraints at the onset of impact, will remain constant. In the case of the RCP, the front wheels are constrained in the same manner as the two-body example, and so impact simulations with the full model of the rover, produce a constant effective kinetic energy for angles of impact greater than or equal to 60° . This explains the flat shape of the curve of Fig. 5–10 for higher angles of impact. The impact force however, follows the same trend, and so both indicators are still in agreement regarding impact on perfectly stiff terrain.

Impact with constitutive models of the ground are shown in Fig. 5–12, with results from the linear visco-elastic model illustrated in plot (a), and the nonlinear visco-elastic model illustrated in plot (b). The stiffness coefficient k , of the ground is varied in plot (a), ranging from stiffness typical of rubber to stiffness in the range of steel. As the stiffness coefficient is increased, the data moves from the limiting condition equivalent to having no ground modelled at all, to the opposite limiting condition of having a perfectly stiff ground modelled with kinematic constraints. This reinforces the results in Fig. 5–10. Similarly, the same trend is seen in plot (b) in which the damping coefficient b , is varied through a range which produces a range in magnitude of the

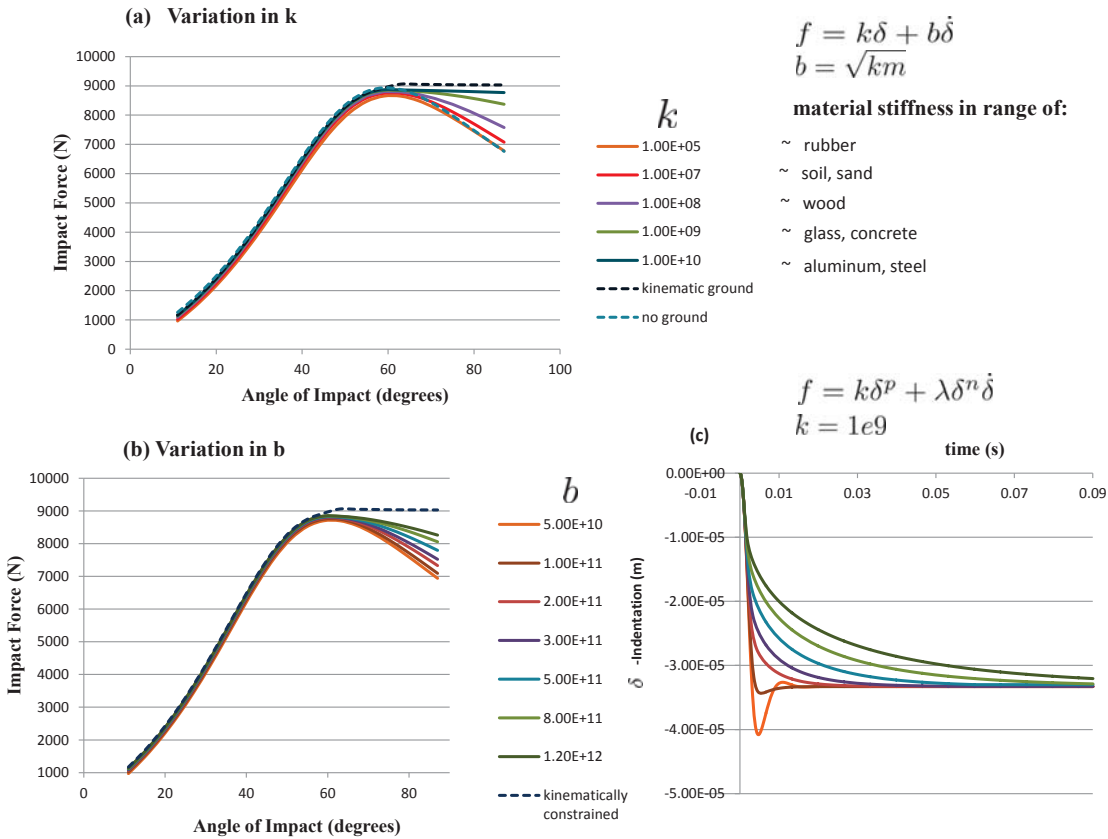


Figure 5–12: a) Impact force plotted with a linear constitutive contact model of the ground for different values of the stiffness coefficient k . (b) Impact force plotted with a nonlinear constitutive model of the ground with different values of the damping coefficient b . (c) Penetration of the ground by the front wheels as the rover reaches steady state rolling, corresponding to the simulations in plot (b).

contact force f , from the ground as the impact progresses. As explained in Section 5.4, to run an impact simulation appropriately when the ground is modelled with a contact force, the steady state rolling must first be achieved before the impact occurs. The relative indentation of the wheels of the rover into the ground, as they transition from their initial position with zero sinkage, towards their steady state rolling with a degree of sinkage δ , is shown in plot (c) for corresponding values of b in plot (b). This is done to illustrate the degree of damping for each value of b .

CHAPTER 6

Experiments

Simulations in the last chapter show the trend between force and energy indicators in impact situations. In order to experimentally verify these results, a set of impact experiments with the RCP were proposed and carried out. They were performed in the Mars Dome belonging to the University of Toronto, Institute for Aerospace Studies (UTIAS). The facility was equipped with ample space to work and had both sandy and concrete surfaces available for testing. The impact experiments would coincide with similar experiments also involving the RCP and research topics of three other members of our group. Consequently the set-up and execution of the experimental process was a team effort with each member playing a leading role in the design, set-up and execution of experiments pertaining to his or her particular field of research. One such set of experiments, dealing with the subject of rover mobility is part of the research work described in [29, 30]. The proposed set of experiments required an additional actuation system to be designed and installed on the RCP. Due to contributions by the author of this thesis, in the design and implementation of this actuation system, the following section discusses this design before returning to the particulars of impact experiments.

6.1 Design of an Actuator System for Control of Normal Force Distribution

Normal force distribution refers to the distribution of normal forces developed on each of the rover wheels due to factors such as: external loading, mass distribution, and configuration of the rover. These forces are illustrated by the purple arrows below the RCP wheels in Fig. 6–1 (a). Simulation studies have shown that the total traction force that a rover can develop, can be maximized by modifying the normal force distribution. In the proposed set of experiments, the RCP was to be driven on sandy terrain, and the drawbarpull would be measured as the normal force distribution was varied, in order to verify this theory experimentally. Manipulation of the distribution of normal forces was to be achieved through repositioning of the centre of mass (CoM) of the rover

using weights mounted in different locations. Complete control of the normal force distribution through re-location of the CoM however is not possible. The practical difficulty of redistributing the inertia of the components of the rover, poses an obvious problem to CoM relocation. Another issue however is that the popular feature of passive suspension in the design of planetary rovers means that full control of the normal force distribution is not possible. This is because the shifting bogies will apply load on the supporting wheels according to the bogie configuration. Since this configuration shifts continually according to the terrain, load on each of the wheels shifts, and thus the distribution of forces, shifts also regardless of position of the CoM. This is especially true in unstructured terrain. To supplement the control of the normal force distribution by redistribution of the mass, the option of actuating the passively moving bogies was explored. In this manner, loads on each of the six wheels can be altered by applying a torque about the joints connecting bogies to body as is illustrated in Fig. 6-1 (a). To achieve this, actuators, referred to as ‘redundant actuators’, had to be selected and positioned according to a set of specifications described below. This process required some thought in order to effectively drive the bogies without risking damage to the RCP, and limiting the range of mobility.

Specifications for the actuators of both a functional and a physical nature limited the choice of candidates for the task at hand. From a functional point of view the actuators while in operation, would require force or torque control. This is so that the torque applied to the bogies could be monitored and adjusted by the operator while the experimental trial was underway. While not in operation, the actuators would be required to remain passive, allowing the bogies to act as they would naturally, without any actuation. This meant that any resistance to motion of the actuator when power was not being applied, had to be eliminated or reduced to an acceptable level. Specifications such as the range of torque or force necessary to drive the bogies, were determined using simulations performed with the GMDL. The maximum desired torque to be applied to each of the bogies was found to be 60 Nm. Physical restrictions on actuator size and weight would apply depending on the location of choice, so as not to incur damage to the rover due to mounting or

operation of the actuators. The options described below are considered for the purposes of a proof-of-concept experimental set-up. The implementation of this type of actuation in a rover destined for planetary exploration would have a different set of design constraints and requirements. Two

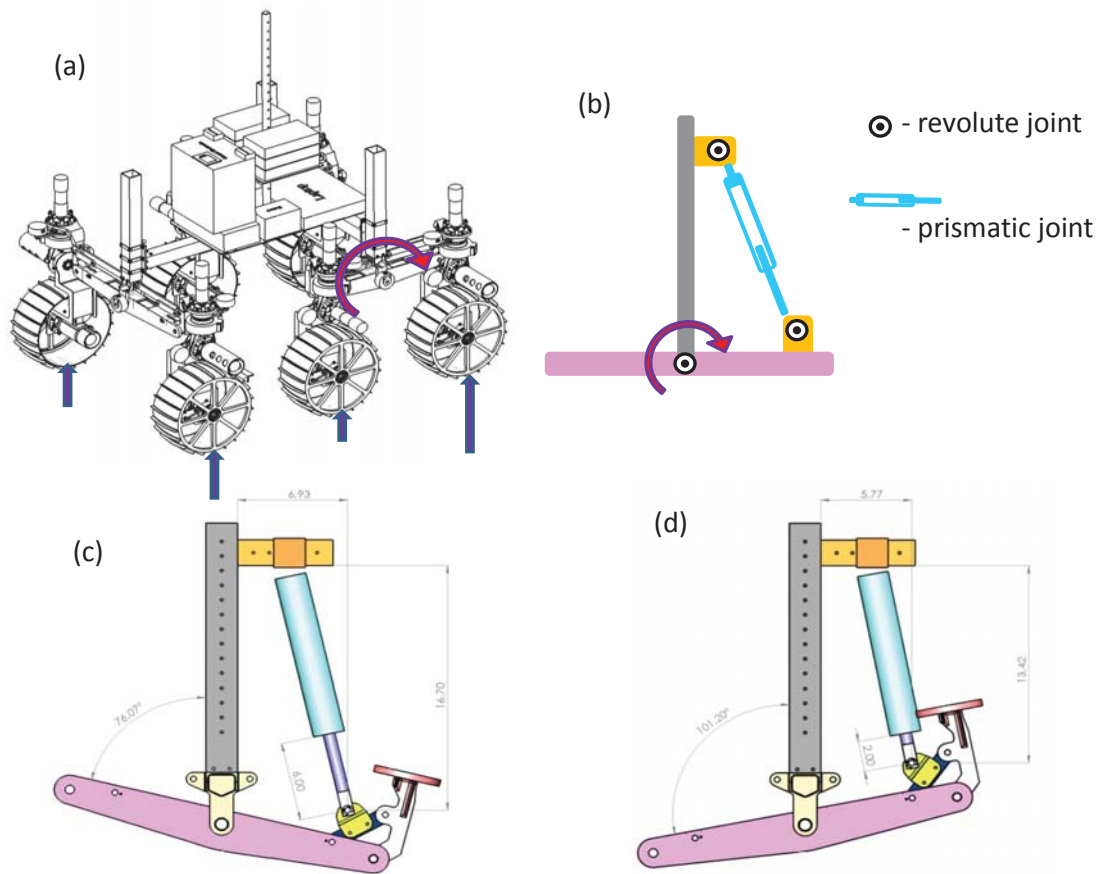


Figure 6–1: a) Applying a moment to the bogies can readjust the normal force distribution. b) A kinematic representation of the actuator-bogie mechanism. c),d) Drawings of the extended and retracted cylinder with attachments and side bogie.

options presented themselves as likely candidates for actuation of the rover prototype. The first was to use a motor to drive the bogie about the revolute joint that connected it to the main body of the RCP. Execution of this installation would involve removal of the press-fit bogie bearings, and installing a motor in their place. This task while not insurmountable, was not a trivial one, and would require considerable time on the part of MDA staff. This was undesirable. Additionally, the necessary torque of 60 Nm would have required a bulky motor and gearbox combination which were unsuited for the structural integrity of the associated mounting location. A gear box

would have increased the resistance to relative motion between the bogies and body of the rover when in the passive mode of operation of the experiments. Unless a mechanism for disengaging the actuator mid-operation was designed and implemented, passive motion of the bogies would not be achieved with this proposed set-up. Alternatively, a torque could be applied about the bogie joints by applying a force to the ends of each of the side bogie links. The forces could be applied with prismatic joints attached appropriately between the RCP body, and the side bogies. The kinematic representation of this actuator mechanism is shown in Fig. 6–1(b). The prismatic joints could be achieved with the use of linear actuators which, if optimally located, would not be required to apply a very large force. This option seemed to be more feasible especially as integration of this design with the RCP would be as simple as drilling holes into the bogies to mount the actuator attachments. The same issue of resistance to back driving of the system however is also posed with electro-mechanical linear actuators. Additionally, the majority of electric linear actuators within the budget of the project were position controlled, rather than force controlled, which would considerably complicate the operation of the experiment.

A solution to these issues was to use pneumatically or hydraulically driven cylinders as actuators. The cylinders would be driven with an appropriate fluid and regulated to a certain pressure. One advantage of a pneumatic system over a hydraulic one is that on top of consisting of lighter, more cost effective components, the pneumatic system will not require active compression of the fluid within. Instead motivation of the cylinders can be achieved with a tank of compressed gas. This pressure could be translated into force by calibrating the pressurized cylinders and a linear relationship between pressure and force could be expected. Through proper valving, when actuation was unnecessary, the ports to both ends of the cylinders could be opened to the surrounding atmosphere, allowing air to pass freely in and out of either end of the cylinder as the motion of the bogie would dictate. A schematic of the system is shown in Fig. 6–2, and the numbers are explained below.

1) Nitrogen cylinder: Compressed nitrogen was used to motivate the air cylinders. Nitrogen is a cheap, plentiful gas, more compressible than air, that is readily available for rental in various size

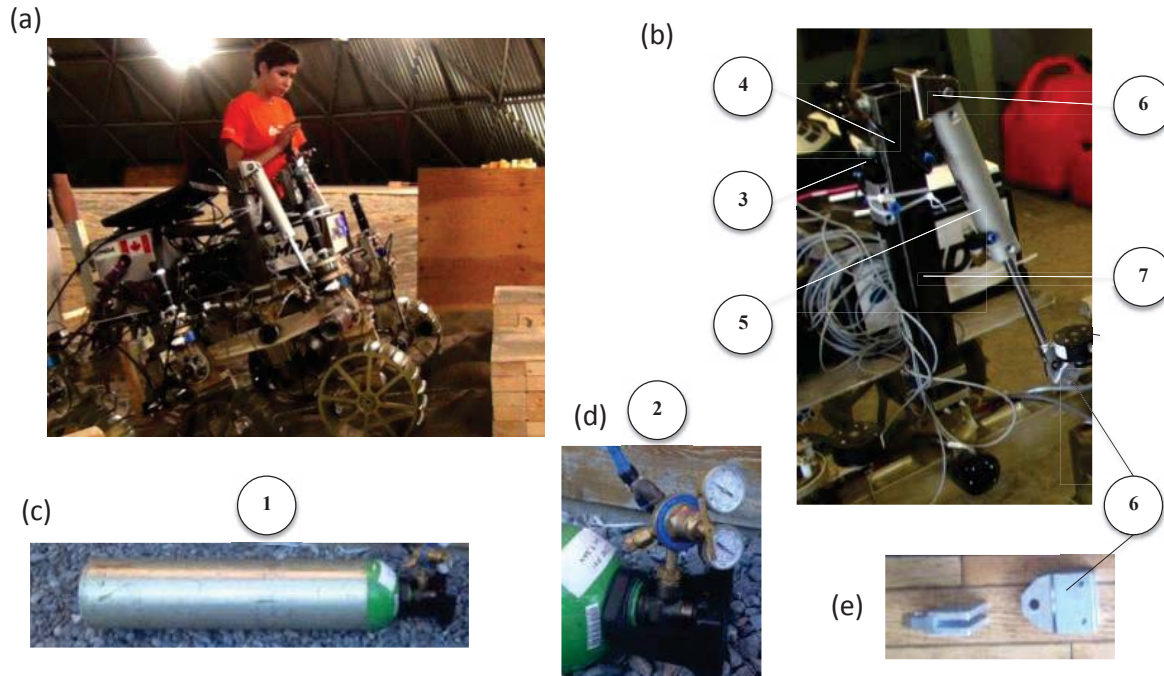


Figure 6–2: a) Rover in obstacle climbing operation with redundant actuation system installed. b)-e) Components of the actuation system.

pressure vessels. Being a noble gas, it is fairly non-reactive and so will not carry moisture or the contaminants carried by air which can cause irregularities in the expansion rate of the gas, as well as being corrosive or damaging to other components in the system.

2) Regulator and gauge: The pressure is regulated at the mouth of the tank with the regulator, and both tank and operating pressure are indicated with the gauge. The tank pressure was initially about 1800 psi, and the operating pressure fell within the range of (0 to 30) psi throughout the experiments.

3) Valving: The valves were electrically driven “Festo” valves that hook up to an electric “normally open” switch. When no power is fed to the valves they allow the cylinders to operate in passive mode. Air is allowed to flow freely in and out of the top and bottom ports in the cylinder with the motion of the rover. When power is supplied to the valves (ie the switch is closed), air is pushed into the top or the bottom part of the cylinder depending on how the airlines have been configured. Connection to the upper port in the cylinder (this is the case in the right image of

Fig. 6–2) directs incoming air to push the piston and extend the cylinder. Conversely, if airlines are connected to the bottom port, the piston is pushed from the bottom and the cylinder retracts. The physical modification of the pneumatic circuit that switched from extension to retraction of the actuators had to be performed when the system was not operating, which was acceptable for this set of experiments. This kept the valving simple and the number of airline branches to a minimum.

4) Air lines: The air lines used were 1\4 " plastic air tubes manufactured to be compatible with quick “push-to-connect” style air fittings for easy connecting and disconnecting of air supply to the cylinders.

5) Cylinders: McMaster Carr cylinders of 1.5" inner bore diameter and 6" stroke length were chosen for being light, strong and cost effective. They were rated for an operating pressure of 100 psi (~6.9 KPa) which would supply ample force necessary to apply the 60 Nm torque to the bogies.

6) Attachments: Manufactured mounting attachments were purchased for attachment to both ends of the cylinders. One clevis per cylinder was custom made to fit the cylinders closely to the RCP, so that they moved inline with the bogies and avoided exerting undesirable side loads that might twist and damage the structure of the rover.

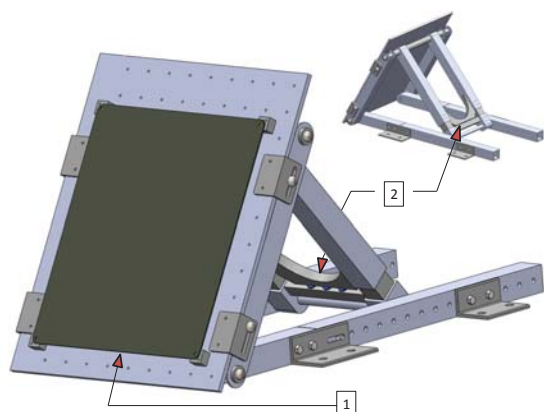
7) Support Posts: The aluminum posts on the RCP that would support the upper end of the cylinders were simply replaced with steel tube of the same dimension. The steel gave more structural integrity than the aluminum would have done, in resisting flexing from the forces applied by the actuators.

While the cylinders were being selected, machining necessary for the attachment of the cylinders to the RCP was performed by technicians at MDA. CAD drawings of the proposed modifications are included in Appendix (C). Figure 6–1 (c) and (d) show CAD drawings of the cylinder attachment.

6.2 Impact Experiments

Returning to the impact experiments, the set-up for these would involve the rover crossing hard and soft terrain, and impacting the surface of a fixed obstacle in its path. The obstacle which became known as the “intelligent obstacle”, was to be built such that the impact surface would

have an adjustable angle of inclination between 0° and 90° . The impact surface would sit on sensors mounted on the intelligent obstacle so that the impact force could be profiled and recorded for the duration of each impact. The main challenges were to choose the correct sensors for the task and to decide where to locate them on the obstacle to optimize the quality of the measurement for all experimental configurations.



(a) CAD model of the intelligent obstacle



(b) Intelligent obstacles shown with protective shield (left) and sensors exposed (right)

Figure 6–3

6.2.1 Choice of Sensor Location

Two practical locations for the mounting of the sensors on the obstacle were proposed, and are indicated as locations (1) and (2) of Fig. 6–3a. Location (1) involves a direct measurement of the impact force as the sensors would be mounted directly on the impact surface, sandwiched between the impact plate and a shield to protect them from the aluminum wheels of the rover. At the time that the experiments were planned it was thought that the RCP wheels, all having grousers about the wheel circumference, would be replaced with smooth wheels for the purpose of the experiments. Unfortunately this was not the case, and so the shield was also necessary to protect the sensors from being torn off by the grousers as the spinning wheel came to rest. The second possibility, location (2), was to mount the sensors in the rear supporting legs of the obstacle. This position would not lead to direct measurement of the impact, and so some loss of information may

	Front Sensor Mount (1) in Fig. 6–3a	Rear Sensor Mount (2) in Fig. 6–3a
Sensitivity to Vibration	<i>High</i> : due to proximity to impact	<i>Low</i> : due to proximity to impact
Loss of information	<i>Low</i>	<i>High</i> : due to absorption of impact by obstacle and ground
Repeatability of measurement	<i>Low</i> : due to high sensitivity to impact location	<i>High</i> : due to low sensitivity to impact location
Complexity of fabrication	<i>Low</i>	<i>High</i>

Table 6–1: Comparison of sensor mounting locations on the intelligent obstacles.

occur. Appendix (C) shows a planar model the obstacle, composed of three members, and how the force is distributed throughout each member as a result of an impact. The predicted loss, which would involve force that would not pass through the supporting rear legs, is estimated to vary with the angle of impact, as a percentage of the maximum force. An advantage of the rear mounting however, is that the quality of the sensor readings would be less affected by the position of each impact force. Additionally the sensor in this location, would not be as sensitive to vibration or noise from the impact, as a sensor located nearer to the zone of contact. Prior to the experimental process, predicting how repeatable the experiments would be was a challenge, as the RCP had been known to veer off course in previous experiments. Table 6–1 lists the advantages and disadvantages of both sensor mounting configurations. It was decided that the obstacle should be built with the option of moving the sensors into either location to accommodate all possibilities. For this set of experiments however, due to time and budget constraints, the rear mounting installation has been designed, but is left for a future set of experiments, and the front mounting position was chosen for ease of manufacture and to capture all available force information.

6.2.2 Choice of Sensors

Given the permissible budget for the experiments, a range of different force measurement methods were available. Strain gauges could be used to determine flex in the obstacle links and

frame, and force could possibly be derived from this data. Pressure sensors could be used to cover a broad area of the obstacle impact surface to measure pressure applied by the wheels to the impact surface. Force sensors could be used to directly measure the impact force at the impact plate, or indirectly measure impact force if positioned within the supporting frame of the obstacle. Of the force sensors, options included load cells of analogue or digital type, and piezoelectric force and impact sensors.

The sensors had two main requirements other than to be economically viable. The first was that they fit within the expected force range resulting from the rover impacting on planes angled between 0° to 90° , while being sensitive enough to detect force differences between impact trials as the angle of impact was adjusted. According to the simulated results, maximum force varies by less than 5% per 10° variation in the angle of impact. Consequently, the sensors would require this type of resolution to be sensitive enough for the purpose of the experiment. A common resolution for force sensors is 1% of the documented force range, so the sensor range needed to be relatively close to the maximum impact force. Estimating this sensor range would be difficult for a number of reasons. The main reason was that the flexibility of the rover was not documented and would require a separate series of experiments to properly model and estimate an effective stiffness to incorporate into impact simulations. In simulations the RCP had been modelled as a system of rigid bodies impacting a rigid plane with a degree of compliance considered only locally, and based on the constitutive properties of only the contacting bodies. As shown in Fig. 5–8, the resulting maximum impact force was in the range of 1000 N-10000 N. In reality, the RCP is a system of flexible links with some clearance and backlash in some of the joints that result in a considerably lower impact force which had to be estimated. Finally, if the sensors are mounted in the front of the obstacle, the most stable configuration is to have three sensors forming a triangle (“the sensing triangle”) on the impact plate, for the purpose of mechanical stability. Ideally, the rover would contact the impact plate in the same location for each consecutive impact and this contact point would be located at the centre of the sensing triangle. Realistically however, the difficulty of manoeuvring the rover effectively and consistently had to be considered. In any given

experimental trial, if the rover veered to one side of the plate, then only one of the three sensors would take the load of the impact. Since two obstacles were to be built and share the load of the impact evenly between them, this meant that the sensors had to be capable of sustaining about half the full impact of the rover, but still have a sufficient resolution to read forces in the range of one sixth the maximum impact force of the rover. Many sensors have a maximum permissible load of about 150 - 250 % of the rated load, so erring on the low end of sensor ranges could result in damaging the sensors.

The second criteria concerning the choice of sensors was that the data sampling frequency be high enough to pick up the maximum force for the expected duration of the impact. Typically, impact requires a high sampling frequency due to the short duration of the event. Using the impact simulations as a guide, any time step of less than 10 000 cycles per second begins to degrade the results noticeably, so a sampling frequency of at least 10 KHz was desirable.

Additional assets were that the sensors could be mounted in an easy and versatile manner so that any changes in the apparatus could be accommodated during the experimental process. Finally, a sensor from a company who would support the integration of their product with appropriate data acquisition, signal conditioning and signal amplification elements of the data circuit was indispensable, as no member of the team was very experienced in this area. Along the same lines, technical support and product literature to aid with trouble shooting of any unforeseeable problems during and after the experimental period, was also desirable.

Strain Gauges: Strain gauges were among the candidates proposed for the sensor choice, as they are an economic option and mechanically easy to install on any location on the obstacle. With further analysis however, deciphering impact force directly from the resulting strain measurements would pose a challenge. The strain of the obstacle would be in several directions, as the links would bloat, twist and flex with the impact to the obstacle. Predicting how the strain gauge would interpret each of these deformations and how direct impact force independent of the location of the impact on the plate was to be deciphered seemed an unnecessary complication. Instead of serving as the primary sensor, strain gauges were considered as back up indicators of force intensity if time

and budget permit.

Pressure sensors: Since the force is distributed over a very small contact area, the use of pressure sensors has little benefit over that of force sensors. One benefit would be if the impact region could be fully covered with pressure sensing film the problem of repeatability of impact location throughout the experiments would be alleviated. Unfortunately, pressure sensing films of appropriate size, with adequate signal frequency, and sensitivity were not available within the expected budget.

Force sensors: Since the quantity of interest was the maximum impact force which would be applied to a small zone, it seemed that choosing force sensors for direct measurement would be the simplest option. Due to the sampling frequency constraints, the option of piezoelectric force sensors were optimal for the application at hand. The sensors chosen were PCB piezoelectric impact sensors. These sensors use quartz crystals to produce a charge when a force or pressure is applied. The sampling frequency of these particular sensors was 30 000 Hz which falls well above the necessary range for clear and accurate simulated results. A notable characteristic of piezoelectric sensors is that they are not suitable for static load measurement as there is a decay in the charge over a given period depending on a time constant associated with the piezoelectric material and the accompanying electronics. The PCB sensors known as ICP type sensors are equipped with built in signal conditioning and amplifying electronics which alleviated any concerns over the assimilation of appropriate electrical components necessary for preserving the clarity of the signal. Finally, a National Instruments data acquisition unit with input channels specifically equipped for the ICP type sensors, was used to process and communicate the impact signals. A National Instruments Labview program was constructed to convert the signal to units of force and appropriately display and direct the data. More information about the piezoelectric effect, ICP sensors and PCB electronics can be found at [7]

An important task at this point was to choose the correct range of force for the sensors. The PCB 208 series of impact sensors come in ranges from 0 – 2 lbf (0 – 0.8 N) on the lower end and go

up to a range of 1000 – 5000 lbf (4450 – 22200 N). The resolution is about 1 % of the total value, and the sensor incurs damage at about 150 % of its maximum rated load. Consequently, to achieve the correct range for the best resolution of the data, without risking the sensors, needed some analysis. As explained the flexibility of the rover had not been analyzed, and would involve its own fully independent experimental analysis to model it with any accuracy. A quick estimate however came from rocking the rover back and forth to determine the amount of deflection in the body. The compliance in the rover comes primarily from the legs which are constructed with a u-shaped bend in them to accommodate proper placement of the wheel and steering motor. The resulting structure however is extremely flexible when compressed from above, as well as being prone to torsion and bending from side loading. Figure 6–4 illustrates the flexible nature of the geometric form of the legs with displacement diagrams generated in SolidWorks. For this particular simulation a 200 N force was applied and produced a range of deflection in the direction of the applied force shown from blue (low deflection) to red (high deflection) for each diagram. The green arrows applied to the lower face of the leg indicate where the leg is fixed, and the pink arrows display the direction of the applied force and surface of application. The maximum deflection is about 4 mm and occurs with the force application demonstrated on the far right figure.

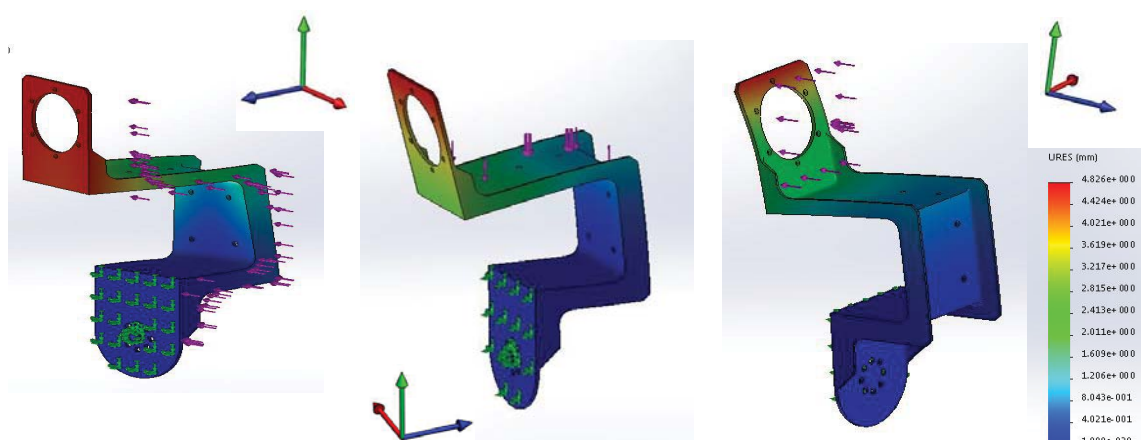


Figure 6–4: Left: head on force applied to leg. Centre: force applied to leg from above. Right: side force applied to leg . The axes in each figure have the same orientation as the global frame in RCP simulations with red, green and blue representing the x, y and z axes respectively.

These added degrees of freedom in each of the six legs combine to produce significant displacement of the rover body with little force applied. On top of this, a degree of play is present in many of the joints that is difficult to model, but contributes to the overall flexing and displacement of the rover when force is applied to it. For a rough estimate of this deflection the rover was rocked back and forth along different axes. A displacement of as much as 4 cm was viewed at the top of the rover with light pushing from the side, before the structure's resistance to pushing became noticeable. Applying force to the front produced a displacement of the body of the rover of about three millimeters, after which any more displacement required considerably more force.

As an estimate, this deflection was divided in half to average the deflection of the top of the rover (3 mm) and the bottom of the rover (0 mm). This estimate of 1.5 mm was to be considered the expected displacement of the rover due to its effective stiffness. With respect to the impact simulations the deflection is represented by the degree of penetration permitted the contacting bodies by the contact forces. In simulations with the RCP, an angle of impact of 60° (which yields the highest impact force developed for angles between $0^\circ - 90^\circ$) would yield a maximum degree of penetration of the rover into the impact plane in the range of 0.03 mm. To estimate the maximum contact force developed for the actual RCP rover, simulations were run with the rigid body model of the rover and the contact force was evaluated using the contact model as was done in a typical rigid body simulation. The contact force value however, was reduced, before being passed on to the set of applied forces that are used to solve the equations of motion. Consequently, a greater penetration of the rover into the impact plane occurred.

This degree of penetration was compared to the expected deflection of the rover of 1.5mm discussed above. The process was repeated with increased reduction of the contact force until the simulated and expected deflections were found to be equal. This occurred when the maximum impact force was 210 N for an angle of 60° . The simulation is referred to as the "reduced contact force model simulation". To estimate the force range for the sensors, this value was divided by six as one sensor would ideally take one third of the impact applied to each obstacle. This gave an

expected force in the range of 8 lbf (35 N) for each sensor, with the need to withstand a full force of 24 lbf (154 N) applied to the obstacle by the rover, in the event that just one sensor is hit.

Two possible sensor ranges available in sensors manufactured by PCB were possible candidates for the sensor choice, one with a range from 0 to 10 lbf and one from 10 lbf to 100 lbf. The expected force value fell very close to one of the extremities of each of these ranges which could pose problems either in damaging a low range sensor with an over loading impact force, or losing information through too low a resolution with the higher range sensors. It seemed however, that since the calculations were based on a very rough estimate, that erring on the side of caution and purchasing the tougher, higher range sensors was wise. Additionally, if the force applied by the rover was on the low side, weights could be added to the rover to shift the range upwards to a certain degree into the sensor range. The final choice of PCB piezoelectric sensors was the ICP 208 C02 model with force range of 10 – 100 lbf, (45 – 445 N).

6.2.3 Construction of the Intelligent Obstacles

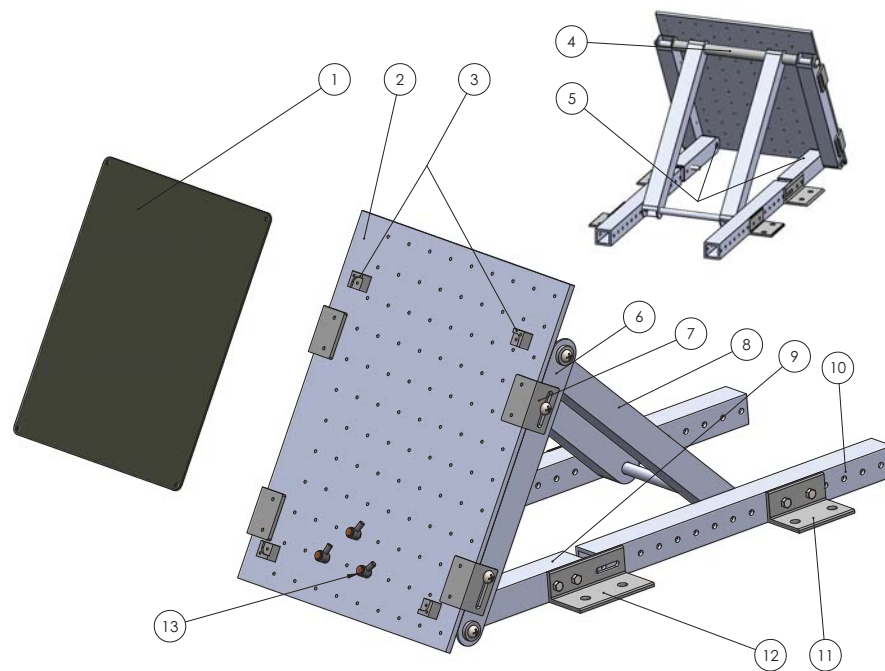


Figure 6–5: CAD model of the intelligent obstacle.

Though not a highly complex component of the experiments, the intelligent obstacles presented a few design challenges that required some thought. Their primary function was to resist the impact force, while providing a variable location for the impact sensors which would shield them from direct contact with the rover. They were built with the hopes of using them for future experiments involving impact, obstacle and slope climbing, and so they are made to sustain greater loads than the predicted impact loading from experiments with the RCP described in this thesis. Possible configurations for future experiments with the obstacles are shown in Appendix(C) along with more detailed CAD drawings. Figure 6-5 displays the parts of the obstacle with numbers, which will be referred to in brackets in the following text. The main part of the obstacle is the impact plane, which consists of two plates: the shield and the mounting plate, (1) and (2) in Fig. 6-5 respectively. The mounting plate, $3/8 \times 20 \times 24$ " aluminum, is the base onto which the sensors attach with a single machine screw. The plate has rows and columns of 96 holes, 2" apart to accommodate a wide range of sensor positioning and is heavy so as to sustain impact without much flexing or deformation. The shield is a steel $1/8 \times 18 \times 16$ " plate intended to protect the sensors from being scratched or torn off, by the grousers of the rover. It rests on the sensors (13), and on four stand-offs (3) of the same height which screw to the support plate. The shield must not absorb any of the impact from the rover, but transmit it to the sensors. Ideally it would slide freely as the pressure from the rover wheels pushed it, but the logistics of fabricating a sliding frame to allow this, on time and within the budget made this feature impractical. As a close approximation, the shield was allowed to slide on shoulder bolts fixed to the four corner stand-offs, rather than to bolt it securely in place. Originally a more compact sized, precision ground shield, had been fitted over the sensors, (Fig. 6-6 (a)) but the difficulty of hitting a smaller target repeatedly with the RCP made the choice problematic. The larger shield (mild steel and not ground flat due to budget constraints) was kept thin, so that it would bend easily if any inherent deformation prevented it from sitting perfectly on the sensors. Fig. 6-6 (b) shows the impact shield not sitting on all three sensors evenly. The impact support plate rests on a frame of $1/8 \times 2 \times 2$ " aluminum tube (6), and is fixed through slotted brackets bolting to the side of the frame (7). The slots allow for finer adjustment

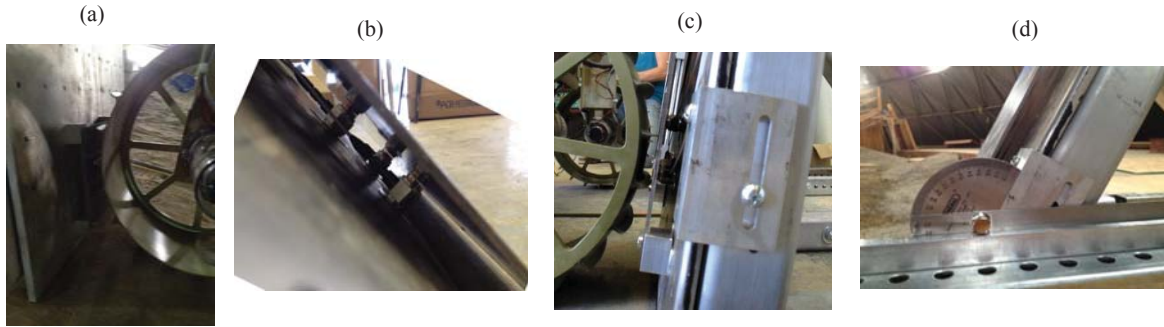


Figure 6–6: Left to Right: a) Compact sensor shield. b) Slight warp in shield prevents it from resting evenly on the sensors. c) Measuring the angle of the obstacle. d) Sensing triangle lifted to meet expected contact point of wheel.

of the height of the sensors, so that they can be precisely aligned with the expected contact point of the wheel. The frame then hinges at top and bottom (4)(5), to the rear supporting legs (8)(9), of the same stock size aluminum. The lower rear legs (9) attach to lengths of “telus bar”, steel tube with pre-fabricated holes every inch (10). The upper legs bolt into which ever holes in the telus bars roughly accommodate the desired angle. Angle iron brackets (11) and (12) attach to the supporting legs and fix the obstacle to the ground or a plywood base. Bracket (12) connecting the lower legs to the telus bar, is milled with a fine tuning slot to more precisely achieve the desired angle. As shown in Fig. 6–6 (d), the angle was achieved within one to two degrees for each configuration. Shorter versions of the supporting legs (9), were made to accommodate lower angles of impact ranging from 0° to 30° . This angle however poses difficulty for the planned impact configuration, in which the rover drives into the impact plane, as the contact point between the rover wheels and the obstacle is so close to the ground. The angle is more suited to a drop-down impact which involves the rover driving off a ledge or step and impacting a surface beneath it at different angles. This drop-down configuration series of experiments however, was not achieved during the experimental period due to the limited time available in the experimental location, and so is left for a future analysis.

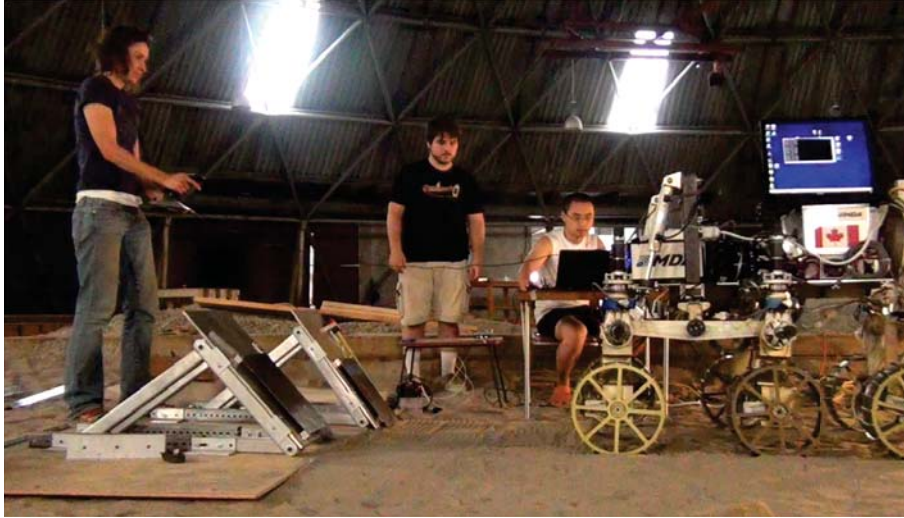


Figure 6–7: Typical soft soil impact trial

6.2.4 Impact set-up and procedure

Two sets of impact experiments were performed in the Mars Dome: one on hard soil (concrete) and one on soft soil (sand). For both tests the obstacles were placed at angles ranging from 40° to 90° and experimental trials were performed at increments of 10° . As previously mentioned, the angles ranging from 0° to 30° were left for a future set of experiments, these angles were too shallow to practically measure impact with the available set-up. Sensors were located in a triangular configuration on the obstacle impacted by the starboard side of the rover. For each configuration of the angle, the sensors were located on the impact planes in triangular form so that the centre of the sensing triangle would be located exactly at the height of impact point of the wheel. This impact point was the predicted impact point for a smooth wheel impacting an angled plane (point *C* in Fig. 5–4), and of course was not necessarily the point of initial contact in many of the impact trials due to the presence of grousers. This position however was the centre of the range in which grousers would make initial contact with the plate. This impact point shifts as the angle of impact shifts and the location of the sensing triangle must be shifted at each angle to match the contact point. This alignment of the sensors and the contacting RCP wheel can be seen in Fig. 6–6(c). Low noise cables from the sensors ran from the obstacles to the data acquisition and a computer to the side of the obstacle set-up. The rover was located at a position of approximately one meter from

the expected impact, and driven manually by joystick control towards the obstacle. The distance preceding the obstacle was necessary just to ensure that the rover reached its maximum velocity before impact occurred. Before sending power to the motors of the rover via joystick command, a certain initiation procedure was followed for each trial. The sensor readings of the RCP's force and torque sensors had to be zeroed for every trial which involved rebooting the RCP computer each time. During this period, the joints in the rover were manually "destressed" by lifting the rover, and allowing the flexible legs to fall into a natural position before zeroing the force sensors. This was necessary as the legs swayed in various directions while the rover was driving, resulting in atypical loads on the sensors. Once the sensors were zeroed and the rover was "destressed", two cameras, one giving an overall view, and one giving a close up of the impact, were set to start recording. The joystick control option was initialized, and the rover was driven towards the obstacles. Upon impact, the operator would release the joystick and the power to the rover was cut. After an initial test was performed, the impact force was found to be just within the range of the force sensors. To shift the impact force intensity further into the sensor load range, two 25 lb weights were placed, one on either end of the rover. The resulting force ranges fell at about 150 to 200 N which was acceptable for all probable situations, giving a good resolution for standard trials, but not so high that a heavy load on one side of the obstacle would overload the receiving sensor. In total, 51 trials were performed over the range of angles for both hard and soft soil combined, each angle having on average about four repeated trials, to gain sufficient data for all six angle configurations.

6.2.5 Experimental Results

Ideally, from a simulation with three sensors instead of just one, the impact of the rover would produce three smooth curves, one for each sensor, with approximately $1/2$ the total force applied on the top sensor, and approximately $1/4$ the total force applied on each of the right and left lower sensors (due to the geometry of the $2'' \times 2''$ hole pattern on the impact surface for mounting sensors). The signals would be simultaneous, relatively continuous and all peak at the same time as illustrated in Fig. 6–8. An ideal situation in an experimental set up is very unlikely. However, due

Ideal Elastic Impact Force Profile For A 'Smooth Wheel' Rover Distributed Over Three Impact Sensors

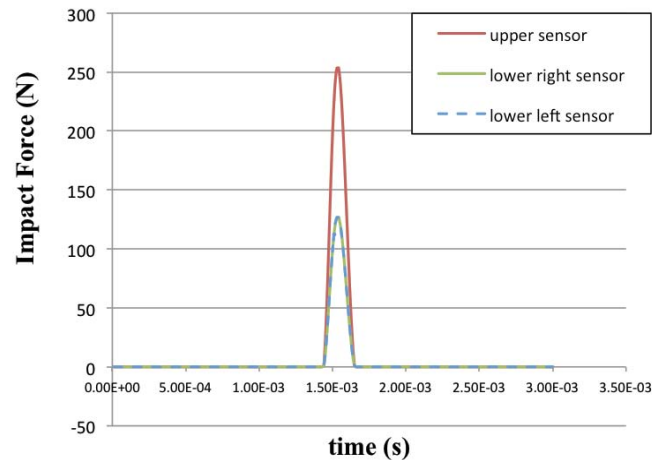


Figure 6–8: Ideal three sensor impact curve.

to several non-ideal circumstances in the set up, the list of deviations of the experimental setup from the simulated one is considerable. Fig. 6–9 below shows a sample of a typical experimental impact plot for either hard or soft soil. The numbers on the graph correspond to unplanned phenomena present in the experimental data, and the blue rectangle in the top right-hand corner is a diagram of the intelligent obstacle with the blue, red and green dots representing the three sensors. The colours of the data series are associated with the sensor in the location indicated by the corresponding dot colour.

1) Vibration: Throughout the graphs, oscillations of several frequencies disturb the data, the most distinct being an approximately 20 Hz oscillation when contact is first made. This was primarily due to the steel shield cover which was particularly susceptible to such vibration given its thin, flat geometry, made specially to bend. Other frequencies of vibration due most likely to vibration of the obstacle and rover structures can also be seen in the data. Additional noise due to friction of the wheels sliding and slipping against the impact surface also create some of the disturbances apparent in the plot. While the ideal plot shown in Fig. 6–8 would allow the analyst

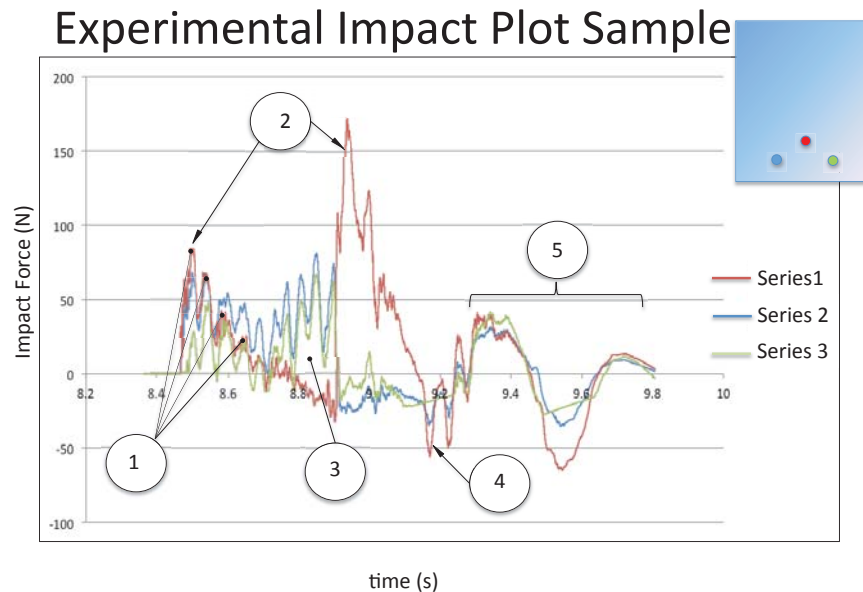


Figure 6–9: Sample data for impact at 60° .

to add the three signals together and choose the maximum total value, the fluctuations in the experimental plot render this method of analysis inaccurate. Varying frequencies in the data due to the multiplicity of vibration also make signal filtering a complicated task.

2) Grousers: Each of the series in the plot shows multiple peaks instead of one single peak for the duration of the impact. This was due to the presence of grousers on the wheels. While the RCP is equipped with a set of smooth wheels, these were unavailable at the time that the experiments took place, and the effects of these disturbances on the impact profile, had been unplanned for. At the point of impact, the first impacting grouser created a peak typically touching the top sensor (Fig. 6–9, red series) and rolling down to the lower sensors (Fig. 6–9, green and blue series). During the deceleration of the rover, the wheels continued to spin for a short duration, and so a second grouser typically impacted the surface of the obstacle. Although grousers are a useful and common feature on a rover wheel, used to increase traction and assist the mobility of the rover, with respect to the impact experiments they introduce a series of more complex events, which should be studied independently to better understand them. As well as the presence of multiple peaks, peaks from the same grouser impact occur at different times due to the staggered location of the sensors, and the

moving grouser. This makes the choice of where the maximum impact occurs unclear. Throughout the 51 plots, the distribution of these peaks varies considerably, adding an additional variable to the impact upon which the maximum total impact is dependent.

3) Distribution of momentum: Depending on the grouser configuration upon impact, impact may be absorbed in a low magnitude force over a longer duration or a high magnitude force over a short duration. This can be seen in Fig. 6–9 where number (3) points to the signals of the blue and green series which absorb impact force over a longer duration than the red signal, but attain a lower maximum peak. This sensitivity to grouser configuration will affect the value of the maximum force for otherwise identical trials. This topic will be expanded upon in the next section.

4) Negative Values: As previously mentioned, the piezoelectric sensors come with a time constant that determines the rate of decay of the applied force. The ICP 208 C02 sensors have a time constant of 500s, however the electronics set to treat impact pulses rather than longer duration loads, reduce that time signal considerably to about 0.5 seconds. This produces negative values when the load is released from the sensor, and the decaying signal drops below zero in reaction to removal of the force.

5) Flexibility: As previously mentioned, the flexibility of the rover was a concern, primarily for the task of determining the sensor range, but also due to the effects that the flexible structure of the rover would have on the data, and impact results. The effects of the flexibility in the rover can be seen in the data in these lower frequency oscillations that occur at the end of each impact. The frequency of these oscillations match with the visible shaking seen by the rover on camera after the wheels come to rest. Grousers on the rover made driving on hard soil especially difficult as the impenetrable nature of the concrete would not absorb the tips of the grousers in the way that soft soil does, creating a vertically applied impulsive force on the wheels. Consequently the springy shape of the legs and the rest of the flexible linkage experienced and increased wobble on hard terrain. Due to the compliant nature of the RCP, and its swaying motion throughout the impact trials, each impact is subject to a range of possible impact configurations for the same impact angle, adding

yet another possible variable in the set-up.

Other complications were the fact that driving the rover in a straight line was quite challenging once again due to flexing in the legs and swaying of the body. This issue affects the repeatability of each impact trial, which was consequently quite low. Operator error in releasing the joystick control at the same moment of impact each time changed the energy with which the rover drove into the obstacle to some degree. Finally the presence of grouzers has the effect of increasing the friction in the impact, which introduces a tangential force, shifting the resultant impact force from its usual direction, normal to the angle of impact. The degree of shift in the angle of the resultant contact force is dependent on the coefficient of friction between the wheel and the impact plane. This phenomena is depicted in Fig. 6–10, where the images on the right hand side of the

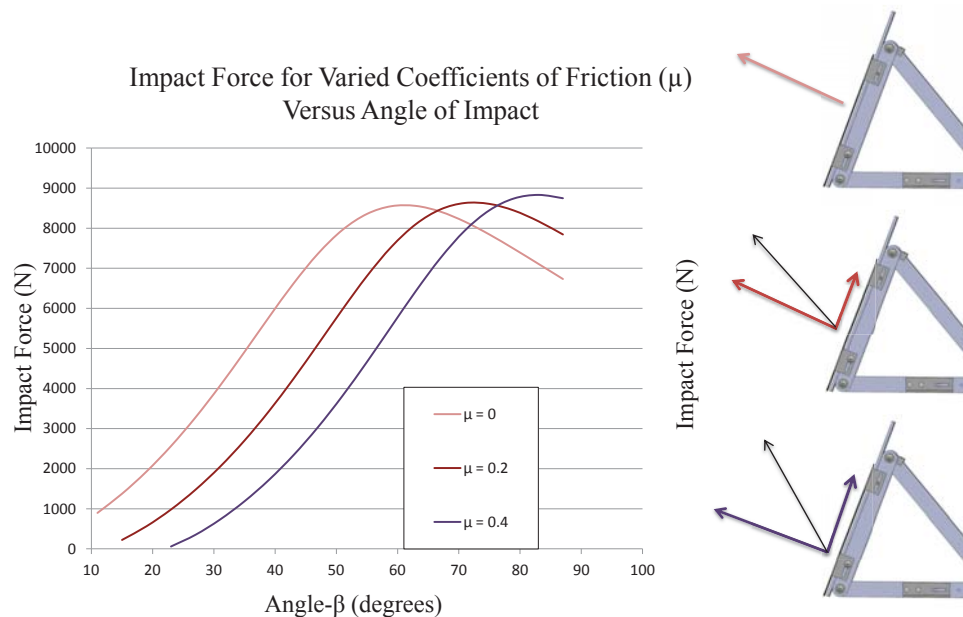


Figure 6–10: Effect of friction on the angle of the contact force.

figure depict the resultant contact force of an impact to the surface of the obstacle. On the left hand side, is the impact versus angle of impact plot displayed and discussed in Chapter 4 that the experimental results endeavour to reproduce. Each curve corresponds to a different coefficient

of friction (μ) between the obstacle and the contacting wheels, and the trend shows that a rising coefficient of friction causes the curve to shift forward. An explanation for this is displayed to the right, where it can be seen that as the tangential component to the contact force grows, the angle of the resultant contact force is shifted. This means that the behaviour of the rover at the point of contact is not purely a reaction to the forces read by the sensors (which only respond to force in the normal direction). The high friction in the grousered wheel occasionally allowed the wheel to climb up the obstacle for lower angles, so a significant presence of friction certainly exists.

6.2.6 Discussion and Considerations

Once the 51 plots were obtained with all the accompanying information, the data was processed. For each impact trial, the available data was: the force reading from the three impact sensors, camera recordings from two locations and the force and torque information from the sensors on the rover. The data for each trial was combined and reviewed.

To begin, some trials were eliminated for obvious poor quality of the trial or the readings. The most common of these were trials in which a grouser had slipped off the bottom of the impact shield when the obstacle was set at lower angles, and the shield had snapped back up and caused excessive vibration in the data. Trials in which the rover had not impacted initially inside the sensing triangle were also discarded, as they produced lob-sided plots, and often lower than average sensor readings. Out of the 51 trials, 27 were performed on hard soil and 24 were performed on soft soil. After disregarding poor trials, 17 hard soil trials and 15 soft soil trials remained. For each impact trial, the sum of the maximum peaks from all three sensor data series was evaluated, and this total maximum was averaged over all trials pertaining to the same angle. The averages were plotted for hard soil and soft soil plots separately, and compared to the simulated results. The simulated results were computed from the reduced contact force model described in section 6.4 where the Hunt and Crossley [42] contact model was used.

As results in section 5.5 illustrate, the trend of the maximum impact force values as they relate to angle of impact, will not be affected by contact model or coefficient of restitution used in the simulation. Only the magnitude of impact force changes with these variables. Consequently, the

coefficient of restitution, for which a realistic value would require a separate set of experiments to determine, was set to 0.90 to facilitate the Hunt and Crossley plots which are most accurate with coefficients of restitution close to unity. As displayed in Fig. 5–12, the model of the terrain beneath the rover will affect the relationship between impact force or effective kinetic energy and angle of impact. While the experiments were performed on concrete and sandy terrain, the flexibility of the legs of the rover (not modelled in simulation) can be expected to some extent, to emulate results of a stiff rover traversing a compliant terrain. Consequently, simulated results displayed below involve no model of the ground, or equivalently a very compliant ground beneath the rover at the instant of impact. The results are displayed below in Fig. 6–11. Error bars in the data show an

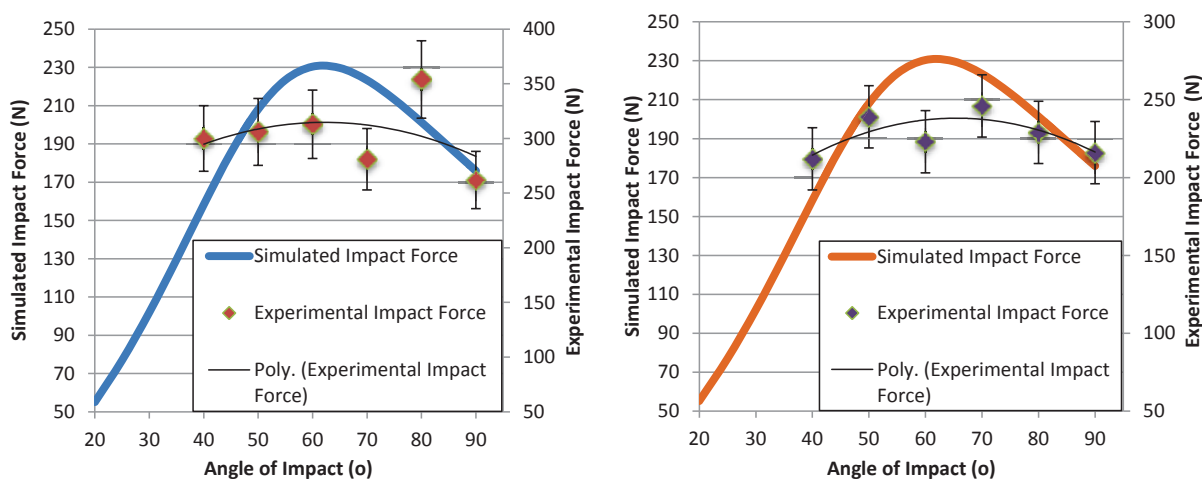


Figure 6–11: Left: hard soil experimental results. Right: soft soil experimental results.

average deviation of individual trial values from the average value for each of the six angles of about 10% for both hard and soft soil. The trend lines in both plots of processed experimental data show a promising result in that they show a similar trend to the curve in the simulated data. The individual average data points however, stray significantly from the expected values. This is especially true for angles of 80° for hard soil and 60° degrees for soft soil. Error and uncertainty due to some of the factors, especially the presence of grouzers in this experimental series is very difficult to predict and process accordingly. Two methods of dealing with the disparity in the simulation set-up and the experimental set-up were: 1) to adjust the simulations to bring them closer to the actual experimental system and set-up, and 2) to perform a second set of experiments

to try to reduce the experimental deviations in set-up, and bring the system closer to the simulated environment. Both methods are attempted and described in the following sections and appendices.

6.2.7 Modelling Grousers

The greatest deviation of the experimental results from the simulated data is most likely due to the presence of grousers in the experimental set-up. The main issue is that while a smooth wheel will ideally contact the impact surface at the same, predictable point for every trial for a given angle of impact (point C in Fig. 5–4), a wheel with grousers will not. The grousers will contact in a range of locations depending on the angle of the wheel when contact is made. From here on this wheel orientation will be referred to as the “grouser configuration”. Using images from the video recordings for each impact trial, the snapshot as the rover contacted the obstacle was used to determine the grouser configuration. Fig. 6–12 below shows two such snapshots from two different impact trials, both with an angle of impact of 90° . The CAD model of the wheel could then be rotated in the SolidWorks environment to visually match the corresponding grouser configuration. The angle the grouser made with the line drawn through the centre of the wheel that intersects the impact plane at 90° , could then be measured. This angle, denoted by α in Fig. 6–12, is termed the grouser offset angle. A grouser offset angle of zero would imply that the grouser was perpendicular to the impact plane at the instant that contact was made, and the contact point would coincide with the smooth wheel contact point, C . In Fig. 6–12 the resulting grouser offset angles are estimated to be 7° and -4° . One effect this has is the displacement of the line of action of the impact force above and below the centre of the contacting wheel. The maximum deviation that this line of action can have is dependent on the angle between the grousers. With the RCP, which has 22 grousers with 16 degrees between each grouser, the contact point can deviate to about a maximum of 2.5 cm above or below the predicted smooth wheel contact point. The displacement, resulting from these varied grouser configurations at impact, does not itself pose a very large problem. As illustrated in the left hand plot of Fig 6–13, a sensitivity analysis was performed to see how this off-centred force would affect the simulated data in a smooth wheel impact, and the deviation is small.

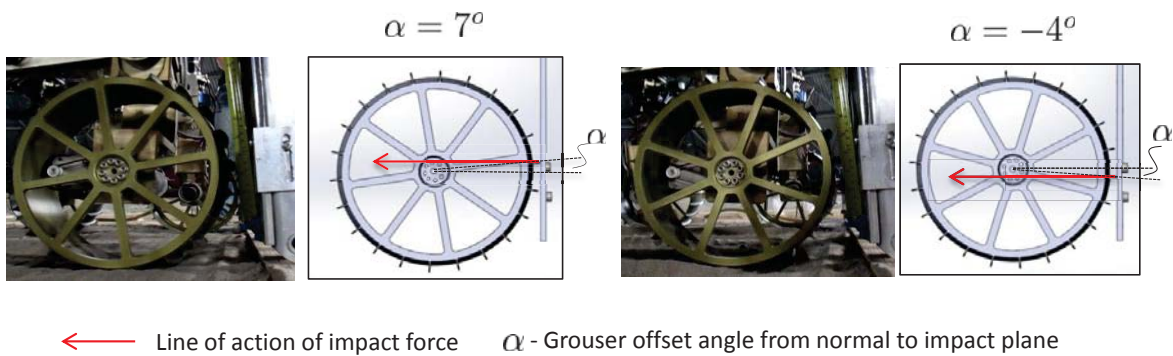


Figure 6–12: Left: 90° impact, first grouser hits above top sensor at 7° offset from normal to impact plane. Right: 90° impact, first grouser hits below top sensor at -4° offset from normal to impact plane.

The issue is however, that the orientation of the grousers as they contact the impact plane, play a role in the shape of the resulting contact force profile. This profile typically has several peaks due to the multiple grouser impacts, unlike a smooth wheel impact, which has just one. A grouser contacting the impact plane so that the associated line of action of the impact force is above the centre of the wheel, will stay in contact with the obstacle for a longer period as the spinning of the wheel rotates the grouser into the impact. Conversely, a grouser that is spinning away from the impact plane as contact is made, will remain in contact for a shorter duration. Thus the number of grouser impacts and the intensity of each impact is largely dependent on this grouser configuration. Examples of three different curves developed in impact plots for the same 90° angle is demonstrated in the right hand plot of Fig 6–13. For each impact, the associated grouser configuration is shown to the right of the plot. Vibrations of about 50 Hz and 20 Hz have been filtered out of the signals to simplify the data. A consequence of this is that the peaks are diminished from their actual values. It is still evident however that the local maxima from each of the trials can vary significantly depending on the orientation of the grousers as they rotate in and out of contact. The total maximum impact force computed from summing all peaks in each series are 181 N, 276 N and 310 N in the red, blue and green series, respectively. This variation in

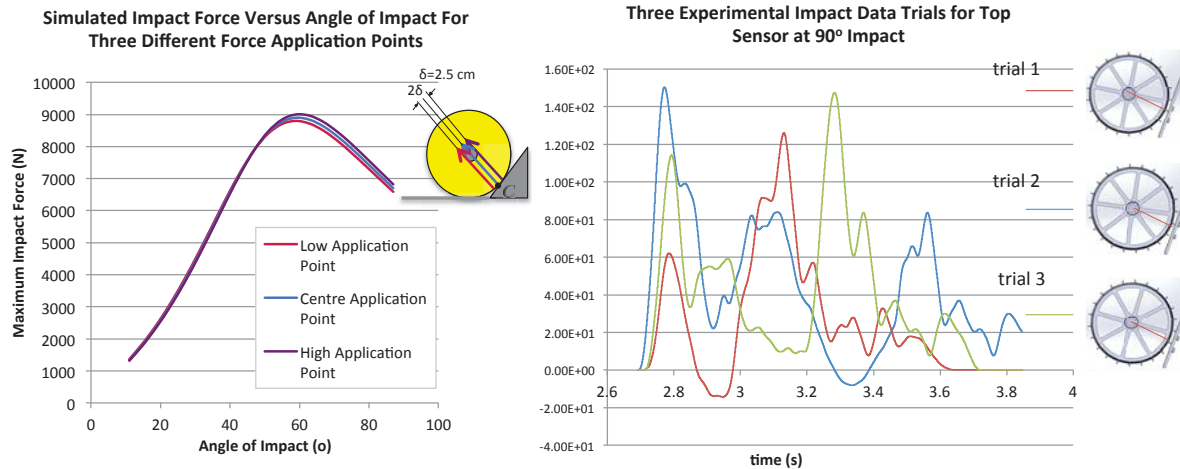


Figure 6–13: Left: sensitivity impact force to application point above and below the smooth wheel contact point “C”. Right: three impact force data series from the top sensor for different 90° impact trials. Grouser configurations upon impact for each trial are shown to the right.

maximum impact force due to grouser configuration, posed a large degree of inconsistency in the data that prompted the reworking of the simulations to accommodate this feature.

A typical reason to consider grousers in a simulation is to investigate the development of traction forces between terrain and groused wheels. The “modelling” of the grouser is often as simple as extending the wheel radius (typically measured to the rim of the wheel), so that it is measured to the tip of the grouser, [49]. This radius will be referred to as the “grouser radius” of the wheel from here on. For the purposes of developing the right impact force profiles due to the repeated grouser impacts on the obstacle surface however, simply extending the radius will not suffice. Instead the individual grousers have to be considered. Grousers were modelled in a simple, one-dimensional manner, without the presence of friction. Referring back to section 5.2, the contact detection algorithm for a smooth wheel involved a projection of the position vector of the wheel onto the line normal to the impact plane. The algorithm for detection of the grousers is very similar. In Fig. 6–14 (a), the RCP wheel with its 22 grousers, is depicted approaching the impact plane. The vector $\vec{\rho}$ (in red) originating at the centre of the wheel, is the same as in Fig. 5–4, the radius of the wheel directed normal to the impact plane. For a smooth wheel, the degree of indentation of the wheel, δ , was found with Eqs. (5.11) and (5.12) and which are rewritten for

quick reference here.

$$\vec{\mathbf{d}} = \vec{\mathbf{w}} - (\vec{\mathbf{r}} + \vec{\rho}), \quad \vec{\mathbf{d}}_n = (\vec{\mathbf{d}} \cdot \vec{\mathbf{n}})\vec{\mathbf{n}}, \quad \delta = \vec{\mathbf{d}}_n \cdot \vec{\mathbf{n}} \quad (6.1)$$

For contact with grousers, δ is now computed individually for each contacting grouser as is demon-

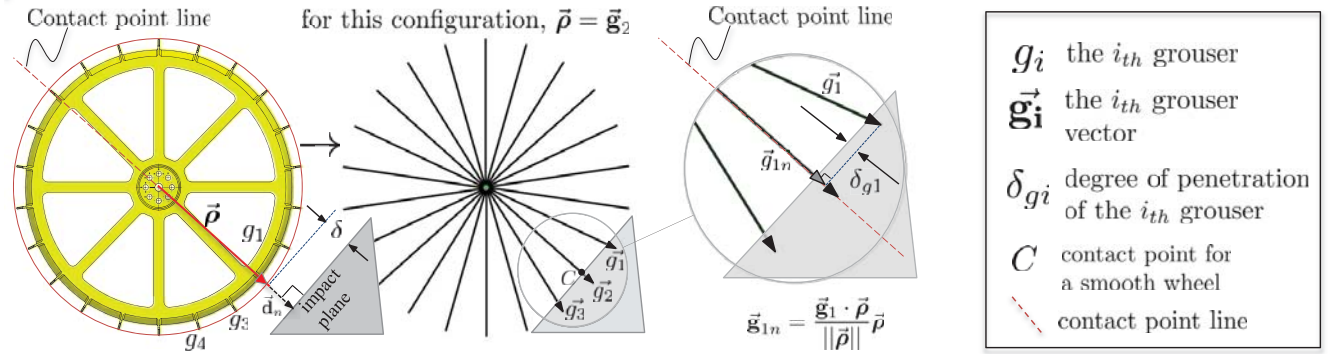


Figure 6–14: (a) Wheel with grousers, (b) grousers represented with vectors, (c) computation of degree of penetration for grouser g_1 .

strated in fig. 6–14 (c) and the equations corresponding to Eq. (5.11) and Eq. (5.12) become:

$$\vec{g}_{in} = \frac{\vec{g}_i \cdot \vec{\rho}}{\|\vec{\rho}\|} \vec{\rho}, \quad \vec{\mathbf{d}}_{gi} = \vec{\mathbf{w}} - (\vec{\mathbf{r}} + \vec{g}_{in}) \quad (6.2)$$

$$\vec{\mathbf{d}}_{gi_n} = (\vec{\mathbf{d}}_{gi} \cdot \vec{\mathbf{n}})\vec{\mathbf{n}}, \quad \delta_{gi} = \vec{\mathbf{d}}_{gi_n} \cdot \vec{\mathbf{n}} \quad (6.3)$$

$$\delta = \sum_{i=1}^j \delta_{gi} \quad (6.4)$$

Here \vec{g}_i is the i^{th} “grouser vector”; a vector with the magnitude of the grouser radius of the wheel, designating the orientation of each grouser in the global frame. The total number of grousers considered to be in contact with the plane is denoted by j . The vector \vec{g}_{in} is then the projection of grouser vector \vec{g}_i onto the “contact point line” shown in Fig. 6–14 (a) and (c). This projected vector is then used to determine the degree of indentation δ_{gi} of the i^{th} grouser. Each individual grouser indentation is input into a contact force model, and the total contact force is now evaluated as the sum of the contact forces for each grouser. The individual forces are applied at the appropriate contact points, corresponding to where each grouser contacts the impact plane. Any number of

grousers can be accommodated, however for a realistic rigid body impact, only two grousers can be in contact with the impact plane at any given time.

Once the grousers were modelled in the capacity described above, a new input to the impact simulation was to adjust the grouser offset angle, α . The incoming angle or orientation of the grouser, was a dominant feature in the shape of the impact force profile that followed. Fig. 6–15 displays two of the three profiles from the data series in Fig. 6–13. For each α corresponding to the orientation of the wheel, simulations were run such that the same grouser offset angle would occur upon impact. The goal was to see if the shapes of the simulated plots would match the experimental data, where only this grouser offset angle was varied.

The plots each display impacts from two grousers, however in the first plot, the initial grouser is moving towards the impact plane as contact is made. In the second plot the initial grouser has just started to move away from the impact plane as contact is made. The plots illustrate that the distribution of momentum, results in very different maximum peaks for each grouser impact. In the first plot with a grouser offset of 7° , the peaks go from a high value to a low value, where as in the second plot with a grouser offset of -4° , the peaks are distributed more evenly at a mid range value. Impact forces of corresponding simulated and experimental plots do not match in magnitude, however the profiles show the same trend.

The goal of modelling grousers was to see if impacts could be simulated such that an input of each of the grouser configurations into the simulation would produce a range of different impact curves for each angle of impact. Ideally experimental plots of a given angle of impact, would match (qualitatively) the profile of the simulated plot with the corresponding grouser offset angle. Then the same experimental plot could be compared to the simulated plots for the same impact angle, for the range of remaining grouser configurations. Thus the plots for each experimental trial could be scaled according to their grouser offset angle in order to eliminate this variable as an unknown from the experimental data. The addition of this grouser offset angle alone is not enough to match all experimental plot profiles to their corresponding simulated plot profiles as other differences between experimental and simulated systems are still present. One of these differences noticeable

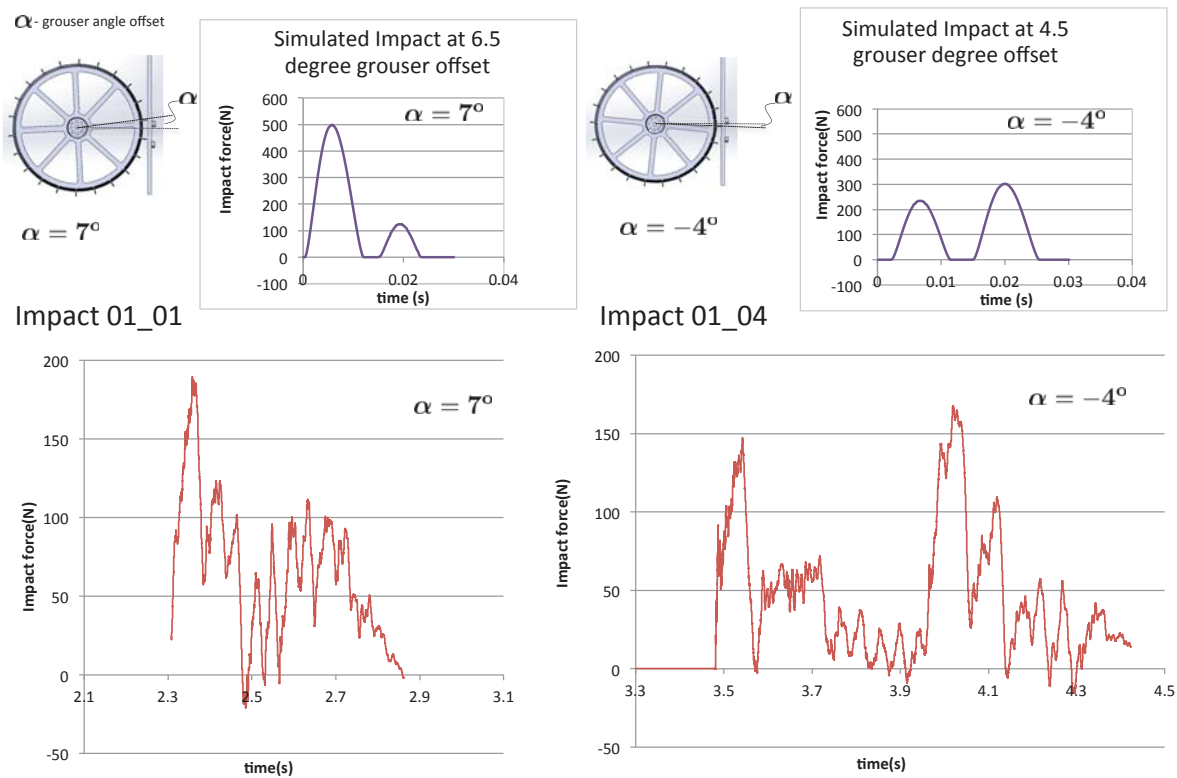


Figure 6–15: Top: Simulated impact plots at 90° with different grouser configurations. Bottom: Experimental plots with corresponding grouser configurations.

in the plots in Fig. 6–15 is the lack of flexibility in the simulated model of the rover. A result of this is that in experiment, impact with the flexible rover produces compression and restitution phases occurring over a much longer duration than would occur if the rover were rigid. This is evident by comparing the horizontal axes of the experimental and simulated plots of Fig. 6–15. With no flexibility modelled in the RCP, the only compliance in the simulation is in the obstacle, and is typically set to the stiff value in the order of 10^9 N/m , to simulate impact with steel. The effect of this is that impact occurs over an extremely short duration ($\sim 10^{-3} \text{ s}$), and is over before a second grouser has time to rotate into the impact plane. To simulate a flexible impact without remodelling the RCP, the compliance of the obstacle was reduced to the order of 10^5 N/m . As is evident from Fig 6–15 this leads to an impact that spans about 0.01 times the duration of the

actual impact. Any further reduction in obstacle stiffness however leads to the unrealistic case of three or more grousers coming into contact with the obstacle at the same instant. A stiffness of 10^5 N/m however, still left the problem that the impact was over before the rover wheels spinning at -0.4 rad/s could rotate a second grouser into the impact plane. To deal with this, the angular velocity of the wheels were increased by controlling a slip ratio that relates the linear velocity of the centre of the wheel to the angular velocity of the wheel. The slip ratio can attain values from zero, signifying that no slipping occurs, to one, signifying that only slipping and no translational motion of the wheel is occurring. The scalar relationship for slip (s) in one direction is:

$$s = \frac{r\omega - v}{r\omega} \quad (6.5)$$

where r is the radius of the rolling body, and v , and ω are the magnitudes of its linear and angular velocities. By controlling the slip, the angular velocity of the wheel could be increased without increasing the linear velocity. This slipping relationship was certainly present in the experimental trials where upon contact, the linear velocity of the wheels was almost negligible, while angular velocity remained significant as the wheels spun before coming to rest. To experimentally estimate the slip of the wheels upon contact with the obstacle during the experiments, was beyond the scope of the experimental instrumentation available at the time. It was possible however to vary the slip and see if a particular value which would allow the simulated data and the experimental data to match up, could be found. For the plots in Fig. 6–15 where two sets of experimental trials are matched with simulations fairly well, the slip was found to give this result at 0.97, which is not an unreasonably high value given that upon impact the wheels are mostly slipping and barely translating at all. This type of modelling did achieve the effect of bringing the simulated data much closer qualitatively to the experimental results, however it was not possible to find one slip value which would allow the experimental and simulated data to correspond for each angle of impact and grouser offset that occurred.

Other than the grousers, additional features of the simulations can be reconsidered and adapted to better approximate the experimental set-up. Two such features would be the modelling of flexibility in the rover, especially the rover legs, and the addition of friction into the contact models representing both the impact surface, and the terrain. While such modelling was pursued to varying degrees, with varying degrees of success, an alternative approach was to simplify the data set by running a second set of experiments to eliminate some of the confusion present in the results. For this reason, a second set of experiments was proposed, with the goal of improving the experimental system and specifically with removing the effects of the grousers from the contact. This set of experiments was constructed and executed, however the analysis is left for a separate document. A brief description of the apparatus, and some discussion of the experimental results are included in Appendix (D).

CHAPTER 7

Conclusions

In this thesis, the effective kinetic energy, a value previously proposed and tested as a performance indicator for impact analysis, was proposed for the analysis of obstacle negotiation with planetary exploration rovers. The initial step of the obstacle negotiation, initial contact, was simulated in a, MatLab based library code, the GMDL, which was developed by the Applied Dynamics Group at McGill. Simulations involved the comparison of the effective kinetic energy of the system, evaluated at the onset of impact, with the maximum impact force developed with the use of continuous force models. The simulated impact was between a rover and an obstacle with a planar surface. The angle of inclination of the surface was varied in order to observe how both force and energy values would depend on this impact configuration. A similar analysis was done where the configuration parameter varied was the position of the centre of mass of the rover. Simulation results demonstrated that force and energy values showed the same trend as the angle or the CoM configuration changed. These simulations were performed for a variety of continuous force models, and a range of coefficients of restitution, and yielded similar results, demonstrating that the validity of the effective kinetic energy as a performance indicator for contact and impact is not dependent on these factors.

A set of experiments to validate the results obtained in simulation, was designed and executed. The analysis of the experimental results posed some difficulties due to the presence of elements in the experimental set-up, such as grousers on the rover wheels and extensive compliance in the rover. Sensors with which the RCP is equipped were not reliable at the time of experimentation either, and so supporting data that gives information about the state of the rover upon impact, was also unavailable. The overall trends of the experiments however, were promising in their potential to validate simulation results that would more closely reflect the conditions of the experimental set-up. To achieve this, the simulations were modified to accommodate multiple impacts resulting

from the presence of grousers, and dependent on the orientation of the wheel upon impact. Additionally, to clarify the results, data was filtered and selected based on the quality of the impact trial. Ultimately the results could be further analyzed to better understand the complexity of the contact events occurring in each trial and the flexible nature of the system, however such an analysis is beyond the scope of this thesis.

A second set of experiments which simplified the experimental set-up was performed. This set-up, eliminated the effects of grousers, and so, more closely resembled a set of experiments with the RCP equipped with smooth wheels. This had been the original expectation, which had motivated the design of the impact measurement system, with the intelligent obstacle, and the impact sensors mounted in the chosen location. While grousers are a realistic feature on the rover, their presence complicates the process of analyzing the data acquired using this measurement system. To further understand the effects of grousers, additional experiments may be required. This could be performed as a continuation of this work.

The results produced from the second set of experiments were considerably more conclusive. These results, which do support the proposed relationship between effective kinetic energy and impact configuration, are presented in Appendix D, along with a brief description of the experimental set-up. The discussion of the procedure and analysis of this set of experiments is left for future work, to be described in a separate report.

Additional to the analysis validating the effective kinetic energy indicator, two other research projects were also included in this thesis. The first was the parametrization of the RCP to develop a parametric rover that supports a quick variation in rover dimensions. Some dimensions of the ExoMars rover were applied to the parametric rover to model an ExoMars-like rover. This rover model was also used in several impact simulations to validate the effective kinetic energy indicator. The second addition was the description of an Applied Dynamics Group collaborated design of a redundant actuator for the RCP, in order to manipulate the normal force distribution across the wheels of the rover.

7.1 Future Work

A natural direction for the continuation of this research, is to extend the impact simulations to a full obstacle negotiation. The goal would be to confirm that the information about the contact configuration-force relationship provided by the indicator would also assist optimizing the configuration best suited to surmounting an obstacle. Some developments to the simulation to more accurately model the realistic conditions of a rover moving through its environment are also suggested. Such developments include the accounting for friction by the contact models representing the impact surface, and the application of terramechanics models to represent the terrain. Modelling of compliance in the system is also recommended. Regarding the effective kinetic energy, an extension of the energy expression to include a sensitivity to the compliance of the system would increase the applicability of the indicator.

References

- [1] Adams. [Internet], [cited April 1, 2016] Available at: <http://www.mscsoftware.com/product/adams>.
- [2] Ambulating Robot for Autonomous Martian Investigation, Exploration and Science (ARAMIES). [Internet], [cited from April 1, 2016]. Available at: <http://robotik.dfki-bremen.de/en/research/projects/aramies.html>.
- [3] Mars Exploration Rovers. [Internet], [cited April 1, 2016], Available at: <http://mars.nasa.gov/mer/home/>.
- [4] Mars Pathfinder. [Internet], [cited April1, 2016]. Available at: http://www.nasa.gov/mission_pages/mars-pathfinder.
- [5] Mars Science Laboratory: Curiosity Rover. [Internet], [cited April 1, 2016]. Available at: <http://mars.nasa.gov/msl>.
- [6] Mathworks SimMechanics. [Internet], [cited April 1, 2016]. Available at: <http://www.mathworks.com/products/simmechanics/>.
- [7] PCB Piezoelectronics. [Internet], [cited April 1,2016]. Available at: <http://www.pcb.com/>.
- [8] Nasa National Space Science Data Center. Luna 17/ Lunakhod. [Internet], [cited April 1, 2016]. Available at: <http://nssdc.gsfc.nasa.gov/nmc/spacecraftDisplay.do?id=1970-095A>.
- [9] Nasa National Space Science Data Center. Luna 21/ Lunakhod2. [Internet], [cited April 1, 2016]. Available at: <http://nssdc.gsfc.nasa.gov/nmc/spacecraftDisplay.do?id=1973-001A>.
- [10] European Space Agency. [Internet], [cited April 1, 2016]. Available at: <http://exploration.esa.int/mars/45084-exomars-rover/>.
- [11] D.S. Apostolopoulos. *Analytic Configuration of Wheeled Robot Locomotion*. PhD thesis, Carnegie Mellon University, April 2001.
- [12] M. Azkarate, M. Zwick, J. Hidalgo-Carrio, R. Nelen, T. Wiese, P. Poulakis, L. Joudrier, and G. Visentin. First experimental investigations on wheel-walking for improving triple-bogie rover locomotion performances. In *Proceedings of the 13th ESA/ESTEC Symposium on Advanced Space Technologies in Robotics and Automation*, Noordwijk, The Netherlands, May 11-13 2015.
- [13] R. Bauer, W. Leung, and T. Barefoot. Development of a dynamic simulation tool for the ExoMars rover. In *Proceedings for the International Symposium for Artificial Intelligence for Robotics and Automation in Space (iSAIRAS)*, Munich, Germany, September 5-8 2005.

- [14] J. Baumgarte. Stabilization techniques of constraints and integrals of motion in dynamical systems. *Computer Methods in Applied Mechanics and Engineering*, 1(1-16), 1972.
- [15] E. Bayo, J. Garcia de Jalon, and M.A. Serna. A modified Lagrangian formulation for the dynamic analysis of constrained mechanical systems. *Computer Methods in Applied Mechanics and Engineering*, 71(2):183–195, 1988.
- [16] E. Bayo and R. Ledesma. Augmented Lagrangian and mass-orthogonal projections: Methods for constrained multibody dynamics. *Nonlinear Dynamics*, 9:113–130, 1996.
- [17] M.G. Bekker. *Introduction to Terrain-Vehicle Systems*. The University of Michigan Press, Ann Arbor, 1969.
- [18] F. Benmar and C. Grand. Quasi-static motion simulation and slip prediction of articulated planetary rovers using a kinematic approach. *ASME Journal of Mechanisms and Robotics*, 5(2):021002–021002–13, May 2013.
- [19] D.B. Bickler. A new family of planetary surface vehicles. In *Missions, Technologies, and Design of Planetary Mobile Vehicles*, pages 301–306, Toulouse, France, September 1992.
- [20] R.M. Brach. *Mechanical impact dynamics, rigid body collisions*. Wiley, New York, 1991.
- [21] R.M. Brach. Formulation of rigid body impact problems using generalized coefficients. *International Journal of Engineering Science*, 36(1):61–71, 1998.
- [22] C. Carpentier, J.M. Font-Llagunes, and J. Kövecses. Dynamics and energetics of impacts in crutch walking. *Journal of Applied Biomechanics*, 26:473–483, 2010.
- [23] J. Chottiner. Simulation of a six wheeled rover called the Rocker Bogie. Master’s thesis, Ohio State University, 1992.
- [24] J. Garcia de Jalon and E. Bayo. *Kinematic and Dynamic Simulation of Multibody Systems. The Real-Time Challenge*. Springer-Verlag, Berlin, 1994.
- [25] S. Ebrahimi. *A Contribution to Computational Contact Procedures in Flexible Multibody Systems*. PhD thesis, University of Stuttgart, 2007.
- [26] Y. Faedi. *Prediction of Tractive Response for Flexible Wheels with Application to Planetary Exploration Rovers*. PhD thesis, University of Surrey, Surrey, UK, June 2010.
- [27] E. Falcone, R. Gockley, E. Porter, and I. Nourbakhsh. The personal rover project, the comprehensive design of a personal robot. *Robotics and Autonomous Systems*, 42:245–258, 2003.
- [28] J.M. Font-Llagunes, A. Barjau, R. Palmies-Villa, and J. Kövecses. Dynamic analysis of impact in a swing through crutch gait using impulsive and continuous contact models. *Multibody System Dynamics*, 28:257–282, 2011.
- [29] B. Ghotbi. *Performance Evaluation and Dynamics of Rovers for Planetary Exploration*. PhD thesis, McGill University, 2015.

- [30] B. Ghotbi, F. González, J. Kövecses, and J. Angeles. Mobility evaluation of mobile robots on soft terrain: effect of internal force distribution. *Mechanism and Machine Theory*, 100:259–282, June 2016.
- [31] A. Gibbesch and B. Schäfer. Multibody system modelling and simulation of planetary rover mobility on soft terrain. In *Proceedings of the 8th International Symposium on Artificial Intelligence, Robotics and Automation in Space (iSAIRAS)*, Munich, Germany, September 5-8 2005.
- [32] G. Giliardi and I. Sharf. Literature survey of contact dynamics modelling. *Mechanism and Machine Theory*, 37:1213–1239, 2002.
- [33] J.H. Ginsberg. *Advanced Engineering Dynamics*. Cambridge University Press, 2nd ed. edition, 1998.
- [34] W. Goldsmith. *Impact: The Theory and Physical Behaviour of Colliding Solids*. Edward Arnold, London, 1960.
- [35] Y. Gonthier, J. McPhee, C. Lange, and J.C. Piedboeuf. A regularized contact model with asymmetric damping and dwell time dependent friction. *Multibody System Dynamics*, 11:209–233, 2004.
- [36] F. González, J.M. Font-Llagunes, and J. Kövecses. Load assessment and analysis of impact in multibody systems. *Multibody System Dynamics*, pages 1–19, 2015.
- [37] F. González and J. Kövecses. Use of penalty formulations in over constrained systems and analysis of redundantly constrained multibody systems. *Multibody System Dynamics*, 29:57–76, 2012.
- [38] E. Hale, N. Schara, J. Burdick, and P. Fiorini. A minimally actuated hopping rover for exploration of celestial bodies. In *Proceedings of the IEEE Conference on Robotics and Automation*, volume 1, pages 420–427, SanFrancisco, California, April 24-28 2000.
- [39] E.J. Haug. *Computer Aided Kinematics and Dynamics of Multibody Systems*. Allyn and Bacon, Boston, 1989.
- [40] H. Hertz. *Gessamelt Werke*, volume 1. Leipzig, Germany, 1895.
- [41] M. Hirschhorn and J. Kövecses. Operational space formulation and analysis for rovers. *ASME. Journal of Computational Nonlinear Dynamics*, 9(4):041005–041005–13, October 2014.
- [42] K.H. Hunt and F.R.E. Crossley. Coefficient of restitution interpreted as damping in vibroimpact. *Journal of Applied Mechanics*, 42:440–445, 1975.
- [43] T. Huntsberger, E. Baumgartner, H. Aghazarian, Y. Cheng, P. Schenker, P. Leger, K. Iagnemma, and S. Dubowsky. Sensor fused autonomous guidance of a mobile robot and applications to Mars sample return operations. In *Proceedings of the SPIE Symposium on*

Sensor Fusion and Decentralized Control in Robotic Systems II, volume 3839, pages 2–8, 1999.

- [44] K. Iagnemma and S. Dubowsky. *Mobile Robots in Rough Terrain*. Springer, 2004.
- [45] G. Ishigami, A. Miwa, K. Nagatani, and K. Yoshida. Terramechanics-based model for steering maneuver of planetary exploration rovers on loose soil. *Journal of Field Robotics*, 24(3):233–250, February 2007.
- [46] G. Ishigami, M. Otisuki, T. Kubota, and K. Iagnemma. Modeling of flexible and rigid wheels for exploration rover on rough terrain. In *Proceedings of the 28th International Symposium on Space Technology and Science*, Okinawa, Japan, June 5-12 2011.
- [47] C. Jarrault, B. Grand, and C. Bidaud. Large obstacle clearance using kinematic reconfigurability for a rover with active suspension. In *Proceedings of the 13th International Conference on Climbing and Walking Robots*, pages 114–121, August 31- September 3 2010.
- [48] Z. Jia, W. Smith, and H. Peng. Fast analytical methods of wheeled locomotion in deformable terrain for mobile robots. *Robotica*, 31(1):35–53, 2012.
- [49] K.L. Johnson. *Contact Mechanics*. Cambridge University Press, London, 1985.
- [50] T.R. Kane. A dynamics puzzle. *Stanford Mechanics Alumni Club Newsletter*, page 6, 1984.
- [51] J.B. Keller. Impact with friction. *ASME Journal of Applied Mechanics*, 53:1–4, 1986.
- [52] O. Khatib. A unified approach for motion and force control of robot manipulators: The operational space formulation. *IEEE Journal of Robotics and Automation*, RA-3(1):43–53, 1987.
- [53] Y.A. Khulief and A.A. Shabana. Impact mechanics of multibody systems with consistent and lumped masses. *Journal of Sound and Vibration*, 104(2):187–207, 1986.
- [54] J. Kövecses. Dynamics of mechanical systems and the generalized free body diagram: - part 1: General formulation. *ASME Journal of Applied Mechanics*, 75:061012–1, 2008.
- [55] J. Kövecses and L. Kovács. Inertia properties and representations in mechanical systems. In *Proceedings of ASME 2015, International Design Technical Conference and Computers and Information in Engineering Conference IDETC/CIE*, volume 6, Boston, MA, August 2-5 2015.
- [56] J. Kövecses and J.C Piedbouef. A novel approach for the dynamic analysis and simulation of constrained mechanical systems. In *Proceedings of ASME 2003, International Design Technical Conference and Computers and Information in Engineering Conference IDETC/CIE*, volume 5, Chicago, IL, September 2-6 2003.

- [57] V. Kucherenko, V. Gromov, I. Kashukalo, A. Bogatchev, S. Vladykin, and A. Manykjan. Engineering support on rover locomotion for the ExoMars rover phase A (ESROL A). Technical report, Science and Technology Rover Company Limited, 2004.
- [58] V. Kumar and K. Waldron. Actively coordinated vehicle systems. *ASME Journal of Mechanisms, Transmissions and Automation in Design*, 111:223–231, 1989.
- [59] H.M. Lankarani and P.E. Nikravesh. A contact model with hysteresis damping for impact analysis of multibody systems. *ASME Journal of Applied Mechanics*, 7:440–445, 1975.
- [60] M. Lauria, P.A. Mausli, M. Van Winnendael, R. Bertrand, and R. Siegart. Design and control of an innovative microrover. In *Proceedings of the 5th ESA Workshop of Advanced Space Technologies for Robotics and Automation.*, (ASTRA '98), Noordwijk, The Netherlands, December 1-3, 1998.
- [61] T.W. Lee and A.C. Wang. On the dynamics of intermittent-motion mechanisms: Part I. dynamic model and response. *ASME Journal of Mechanisms, Transmissions and Automation in Design*, 105:534–540, 1983.
- [62] R.A. Lindeman, D.B. Bickler, B.D. Harrington, G.M. Ortiz, and C.J. Voorhees. Mars exploration rover mobility development. *IEEE Robotics and Automation Magazine*, 13:19–26, June 2006.
- [63] M. Machado, P. Moreira, P. Flores, and H.M. Lankarani. Compliant contact force models in multibody dynamics: Evolution of the Hertz contact theory. *Mechanism and Machine Theory*, 53:99–122, July 2012.
- [64] S. Michaud, A. Schneider, R. Bertrand, P. Lamon, R. Siegart, M. van Winnendael, and A. Schiele. SOLERO: Solar-Powered Exploration Rover. In *Proceedings of the 7th ESA Workshop on Advanced Space Technologies for Robotics and Automation*, (ASTRA 2003), Noordwijk, The Netherlands, November 19-21, 2002. CD-ROM.
- [65] S.A. Modarres Najafabadi, J. Kövecses, and J. Angeles. A comparative study of approaches to dynamics modelling of contact transitions in multibody systems. In *Proceedings of the ASME International Design Engineering Technical Conferences and Computers and Information in Engineering Conference*, Long Beach, California, USA, September 24-28 2005.
- [66] S.A. Modarres Najafabadi, J. Kövecses, and J. Angeles. Impacts in multibody systems, modelling and experiments. *Multibody System Dynamics*, 20:163–176, September 2008.
- [67] N.M Newmark. A method for computation in structural dynamics. *Journal of Engineering Mechanics Division, ASCE*, 85:67–94, July 1959.
- [68] P.E. Nikravesh. *Computer-Aided Analysis of Mechanical Systems*. Prentice Hall, 1988.
- [69] N. Patel and A. Ellery. Performance evaluation of autonomous mars mini-rovers. Technical report, Surrey Space Center, University of Surrey, 2004.

- [70] N. Patel, A. Ellery, C. Welch, A. Curley, and M. Van Winnendael. Elastic loop mobility system: The concept and future prospects for rover mobility on mars. *7th ESA Workshop on Advanced Space Technologies for Robotics and Automation*, November 19-21 2002.
- [71] N. Patel, R. Slade, and J. Clemmet. The ExoMars rover locomotion subsystem. *Journal of Terramechanics*, 47:227–242, 2010.
- [72] G. Reina and M. Foglia. On the mobility of all terrain rovers. *Industrial Robot*, 40(2):121–131, 2013.
- [73] ROAMS. [Internet], [cited April 1, 2016]. Available at: <http://dshell.jpl.nasa.gov/ROAMS/index.php>.
- [74] E.T. Routh. *Dynamics of a System of Rigid Bodies*. MacMillan & Co., London, 1905.
- [75] NASA Future rover missions. [Internet], [cited April 1, 2016]. Available at: <http://mars.nasa.gov/mars2020/mission/rover/>.
- [76] A. Schiele, J. Romstedt, C. Lee, H. Henkel, S. Klinkner, R. Rieder, R. Gellert, G Klingelhöffer, B. Bernhardt, and H. Michaelis. The new NANOKHOD: Engineering model for extreme cold environments. In *Proceedings of the 8th International Symposium on Artificial Intelligence, Robotics and Automation in Space*, Munich, September 5-8, 2005.
- [77] SIMPACK. [Internet], [cited April 1, 2016], Available at: www.simpack.com.
- [78] K. Skonieczny and G.M.T. D’Eleutario. Improving mobile robot step climbing capabilities with centre of gravity control. In *Proceedings of the ASME International Design Engineering Technical Conferences & Computers and Information in Engineering Conference (IDETC/CIE)*, Montreal, Canada, August 15-18 2010.
- [79] C.E. Smith. Predicting rebounds using rigid-body dynamics. *ASME Journal of Applied Mechanics*, 54:754–758, September 1991.
- [80] S.V. Sreenivasa and B.H. Wilcox. Stability and traction control of an actively actuated rover. *Journal of Robotic Systems*, 11(6):487–502, March 1994.
- [81] S.V. Sreenivasan, P.K. Dutta, and K.J. Waldron. The wheel actively articulated vehicle (WAAV): An advanced off-road mobility. In *Proceedings of the 4th International Workshop on Advances in Robot Kinematics*, pages 141–150, Ljubljana, Slovenia, 1994.
- [82] W. Stronge. Unraveling paradoxical theories for rigid body collisions. *ASME Journal of Applied Mechanics*, 58:1049–1055, December 1991.
- [83] W.J. Stronge. *Impact Mechanics*. Cambridge University Press, Cambridge, 2000.
- [84] T. Thueer, A. Krebs, and R. Siegwart. Performance comparison of rough terrain robots, simulation and hardware. *Journal of Field Robotics*, 24(3):251–271, March 2007.

- [85] V.Kucherenko, A. Bogatchev, and M. van Winnendael. Chassis concepts for the exomars rover. In *Proceedings for the 8th ESA workshop on advanced space technologies for robotics and automation*, Noordwijk, The Netherlands, November 2-4 2004.
- [86] Vortex. [Internet], [cited April 1, 2016], Available at: <http://www.vxsim.com/>.
- [87] C.R. Weisbin, M. Montelmerlo, and W. Whittaker. Evolving directions in NASA's planetary rover requirements and technology. *Robotics and Autonomous Systems*, 11:3–11, January 1993.
- [88] D. Wettergreen, S. Moreland, K. Sconieczny, D. Jonak, D. Kohanbash, and J. Teza. Design and field experimentation of a prototype lunar prospector. *International Journal of Robotics Research*, 29(12):1550–1554, October 2010.
- [89] E.T. Whittaker. *A Treatise on the Analytical Dynamics of Particles*. Cambridge University Press, Cambridge, 1988. (reissue of 1904).
- [90] J. Wong and A. Reece. Prediction of rigid wheel performance based on the analysis of soil-wheel stresses part I. performance of driven rigid wheels. *Journal of Terramechanics*, 4(1):81–98, 1967.
- [91] Y. Zhang. and I. Sharf. Compliant force modelling for impact analysis. In *Proceedings of the 2004 ASME Biennial Mechanisms and Robotics Conference DETC 2004*, Salt Lake City, Utah, September 28-October 2 2004.

Appendices

APPENDIX A Two-Body Calculations

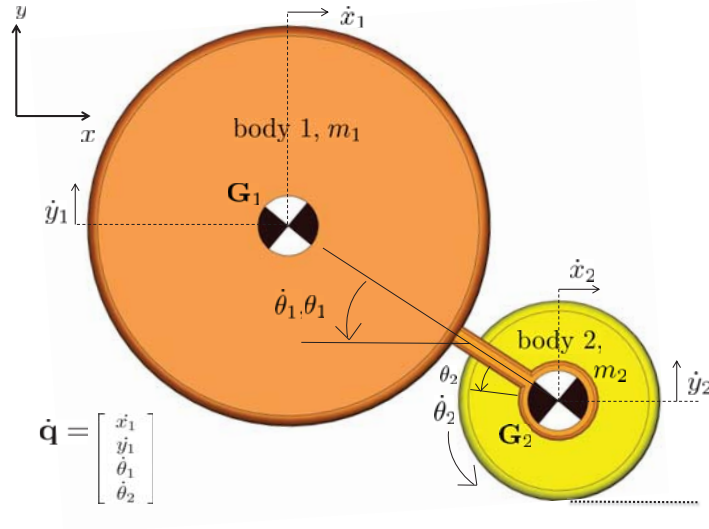


Figure A-1: Two-mass rover system in an impact with a flat surface.

The coordinates are $\mathbf{q} = [x_1, y_1, \theta_1, \theta_2]^T$, giving $\dot{\mathbf{q}} = [\dot{x}_1, \dot{y}_1, \dot{\theta}_1, \dot{\theta}_2]^T$ at the velocity level. The relationships for the centre of mass coordinates for body 2 are:

$$x_2 = x_1 + l \cos \theta_1 \qquad y_2 = y_1 + l \sin \theta_1 \qquad (\text{A.1})$$

$$\dot{x}_2 = \dot{x}_1 - l \dot{\theta}_1 \sin \theta_1 \qquad \dot{y}_2 = \dot{y}_1 + l \dot{\theta}_1 \cos \theta_1 \qquad (\text{A.2})$$

The kinetic energy of the system can be expressed as:

$$T = \frac{1}{2} m_1 (\dot{x}_1^2 + \dot{y}_1^2) + \frac{1}{2} I_1 \dot{\theta}_1^2 + \frac{1}{2} m_2 \left((\dot{x}_1 - l \dot{\theta}_1 \sin \theta_1)^2 + (\dot{y}_1 + l \dot{\theta}_1 \cos \theta_1)^2 \right) + \frac{1}{2} I_2 (\dot{\theta}_1 + \dot{\theta}_2)^2 \quad (\text{A.3})$$

With no potential energy, the Lagrange equations reduce to:

$$\frac{d}{dt} \left(\frac{\partial T}{\partial \dot{\mathbf{q}}} \right) - \frac{\partial T}{\partial \mathbf{q}} = \mathbf{f} \quad (\text{A.4})$$

where \mathbf{f} the array of generalized forces is equal to the 4×1 zero matrix. The expansion of the terms in Eq. (A.4) are:

$$\partial T / \partial x_1 = 0, \quad \partial T / \partial \dot{x}_1 = m_1 \dot{x}_1 + m_2 (\dot{x}_1 - l \dot{\theta} \sin \theta_1)$$

$$\partial T / \partial y_1 = 0, \quad \partial T / \partial \dot{y}_1 = m_1 \dot{y}_1 + m_2 (\dot{y}_1 + l \dot{\theta} \cos \theta_1)$$

$$\partial T / \partial \theta_1 = -m_2 l \dot{\theta}_1 (\dot{x}_1 \cos \theta_1 + \dot{y}_1 \sin \theta_1)$$

$$\partial T / \partial \dot{\theta}_1 = I_1 \dot{\theta}_1 + I_2 (\dot{\theta}_1 + \dot{\theta}_2) + m_2 l (\dot{y}_1 \cos \theta_1 - \dot{x}_1 \sin \theta_1 + l \dot{\theta}_1)$$

$$\partial T / \partial \theta_2 = 0, \quad \partial T / \partial \dot{\theta}_2 = I_2 (\dot{\theta}_1 + \dot{\theta}_2)$$

$$\frac{d}{dt} (\partial T / \partial \dot{x}_1) = m_1 \ddot{x}_1 + m_2 (\ddot{x}_1 - l \ddot{\theta}_1 \sin \theta_1 - l \dot{\theta}_1^2 \cos \theta_1)$$

$$\frac{d}{dt} (\partial T / \partial \dot{y}_1) = m_1 \ddot{y}_1 + m_2 (\ddot{y}_1 + l \ddot{\theta}_1 \cos \theta_1 - l \dot{\theta}_1^2 \sin \theta_1)$$

$$\frac{d}{dt} (\partial T / \partial \dot{\theta}_1) = (I_1 + I_2 + m_2 l^2) \ddot{\theta}_1 + I_2 \ddot{\theta}_2 + m_2 l (\ddot{y}_1 \cos \theta_1 - \ddot{x}_1 \sin \theta_1) - m_2 l \dot{\theta}_1 (\dot{x}_1 \cos \theta_1 + \dot{y}_1 \sin \theta_1)$$

$$\frac{d}{dt} (\partial T / \partial \dot{\theta}_2) = I_2 (\ddot{\theta}_1 + \ddot{\theta}_2)$$

This gives the equations of motion of the two-body system as:

$$(m_1 + m_2) \ddot{x}_1 - m_2 l \ddot{\theta}_1 \sin \theta_1 - m_2 l \dot{\theta}_1^2 \cos \theta_1 = 0 \quad (\text{A.5})$$

$$(m_1 + m_2) \ddot{y}_1 + m_2 l \ddot{\theta}_1 \cos \theta_1 - m_2 l \dot{\theta}_1^2 \sin \theta_1 = 0 \quad (\text{A.6})$$

$$(I_1 + I_2 + m_2 l^2) \ddot{\theta}_1 + I_2 \ddot{\theta}_2 + m_2 l (\ddot{y}_1 \cos \theta_1 - \ddot{x}_1 \sin \theta_1) = 0 \quad (\text{A.7})$$

$$I_2 (\ddot{\theta}_1 + \ddot{\theta}_2) = 0 \quad (\text{A.8})$$

If the dynamic equations are written in compact matrix form as:

$$\mathbf{M} \ddot{\mathbf{q}} + \mathbf{c} = \mathbf{f} \quad (\text{A.9})$$

where \mathbf{M} is the 4×4 generalized mass matrix of the system, \mathbf{c} represents the 4×1 centrifugal and Coriolis term, and \mathbf{f} is the 4×1 generalized force term, then Eqs. (A.5-A.9) give the mass matrix, and centrifugal and Coriolis terms as:

$$\mathbf{M} = \begin{bmatrix} m_1 + m_2 & 0 & -m_2 l \sin \theta_1 & 0 \\ 0 & m_1 + m_2 & m_2 l \cos \theta_1 & 0 \\ -m_2 l \sin \theta_1 & m_2 l \cos \theta_1 & I_1 + I_2 + m_2 l^2 & I_2 \\ 0 & 0 & I_2 & I_2 \end{bmatrix} \quad \mathbf{c} = \begin{bmatrix} -m_2 l \dot{\theta}_1^2 \cos \theta_1 \\ -m_2 l \dot{\theta}_1^2 \sin \theta_1 \\ 0 \\ 0 \end{bmatrix}$$

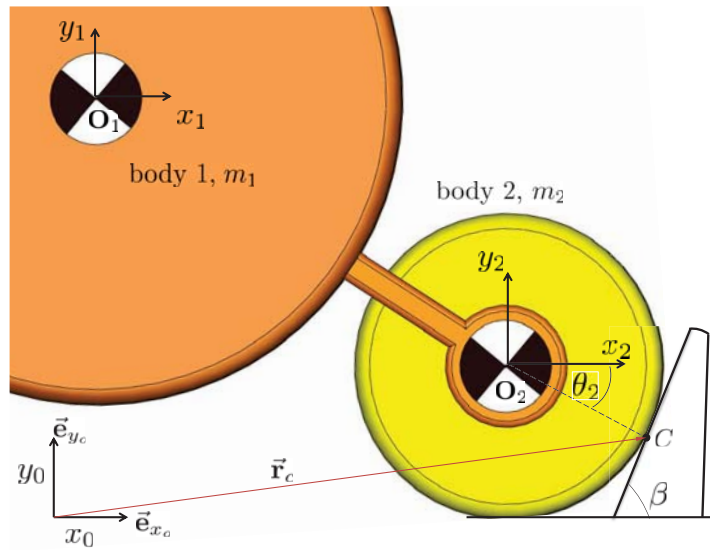


Figure A-2: Evaluating the position of the contact point C

The position and velocity vectors for point C can be found as

$$\vec{\mathbf{r}}_c = x_2 \vec{\mathbf{e}}_{x_0} + y_2 \vec{\mathbf{e}}_{y_0} + R \cos \theta_2 \vec{\mathbf{e}}_{x_0} + R \sin \theta_2 \vec{\mathbf{e}}_{y_0} \quad (\text{A.10})$$

$$\vec{\mathbf{v}}_c = \dot{x}_2 \vec{\mathbf{e}}_{x_0} + \dot{y}_2 \vec{\mathbf{e}}_{y_0} - R \dot{\theta}_2 \sin \theta_2 \vec{\mathbf{e}}_{x_0} + R \dot{\theta}_2 \cos \theta_2 \vec{\mathbf{e}}_{y_0} \quad (\text{A.11})$$

where $\vec{\mathbf{v}}_c$ is the time derivative of $\vec{\mathbf{r}}_c$. At the onset of contact, point C coincides with the angle:

$$\theta_2 = -(90 - \beta)^\circ \quad (\text{A.12})$$

Substituting Eq. (A.12) and Eq. (3.2) into Eqs. (A.10) and (A.11) gives:

$$\vec{\mathbf{r}}_c = x_2 \vec{\mathbf{e}}_{x_0} + y_2 \vec{\mathbf{e}}_{y_0} + R \sin \beta \vec{\mathbf{e}}_{x_0} - R \cos \beta \vec{\mathbf{e}}_{y_0} \quad (\text{A.13})$$

$$\vec{\mathbf{v}}_c = (\dot{x}_1 - l\dot{\theta}_1 \sin \theta_1) \vec{\mathbf{e}}_{x_0} + (\dot{y}_1 + l\dot{\theta}_1 \cos \theta_1) \vec{\mathbf{e}}_{y_0} + R\dot{\theta}_2 \cos \beta \vec{\mathbf{e}}_{x_0} + R\dot{\theta}_2 \sin \beta \vec{\mathbf{e}}_{y_0} \quad (\text{A.14})$$

Taking the x_o and y_o components of $\vec{\mathbf{r}}_c$ and $\vec{\mathbf{v}}_c$ in Eqs. (A.13) and (A.14), then yields the terms for x_c and y_c in Eq. (3.7), and for \dot{x}_c and \dot{y}_c in Eq. (3.8), Chapter 3.

APPENDIX B
Parametrizations For Effective Kinetic Energy

To demonstrate the equivalence of the expressions in Eq. (5.13) used with independent coordinates and Eq.(5.25) used with dependent coordinates, introduced in Chapter 5, let the independent velocities of a system with n degrees of freedom, be represented as the $n \times 1$ array $\boldsymbol{\pi}$, and the dependent velocities be represented as the $(n + m) \times 1$ array $\dot{\mathbf{q}}$. A transformation between $\boldsymbol{\pi}$ and $\dot{\mathbf{q}}$ is given as:

$$\mathbf{B}\dot{\mathbf{q}} = \boldsymbol{\pi} \quad (\text{B.1})$$

where \mathbf{B} is an $(n + m) \times n$ matrix that is not unique. As in Chapter 5, the SCM and SAM are parametrized by the coordinates \mathbf{v}_c and \mathbf{v}_a respectively, which will now have the dimensions of $1 \times r$ and $1 \times s$ respectively, where $r + s = n$. The following relationships between the SCM and SAM coordinates \mathbf{v} and the independent set of coordinates $\boldsymbol{\pi}$ are:

$$\mathbf{J}_i \boldsymbol{\pi} = \begin{bmatrix} \mathbf{J}_{ic} \\ \mathbf{J}_{ia} \end{bmatrix} \boldsymbol{\pi} = \begin{bmatrix} \mathbf{v}_c \\ \mathbf{v}_a \end{bmatrix} = \mathbf{v} \quad (\text{B.2})$$

where the $r \times n$ matrix \mathbf{J}_{ic} transforms $\boldsymbol{\pi}$ into the parametrization of the SCM, and the $s \times n$ matrix \mathbf{J}_{ia} transforms $\boldsymbol{\pi}$ into the parametrization of the SAM. Additionally the equivalent relationship between the dependent velocities and \mathbf{v} is

$$\mathbf{J}_d \dot{\mathbf{q}} = \begin{bmatrix} \mathbf{J}_{dc} \\ \mathbf{J}_{da} \end{bmatrix} \dot{\mathbf{q}} = \begin{bmatrix} \mathbf{v}_c \\ \mathbf{v}_a \end{bmatrix} = \mathbf{v} \quad (\text{B.3})$$

where \mathbf{J}_{dc} and \mathbf{J}_{da} of size $r \times (n + m)$ and $s \times (n + m)$ transform $\dot{\mathbf{q}}$ into parametrizations for the SCM and SAM respectively. Using Eq. (B.1), \mathbf{J}_{dc} can be related to \mathbf{J}_{ic} by:

$$\mathbf{J}_{dc} = \mathbf{J}_{ic} \mathbf{B} \quad (\text{B.4})$$

Also the constraint Jacobian containing the relationships for the m kinematic constraints that are related to the dependent coordinates has the following relationship:

$$\mathbf{\Gamma}\dot{\mathbf{q}} = \mathbf{0}_{m \times 1} \quad (\text{B.5})$$

Here, the constraint Jacobian $\mathbf{\Gamma}$, is of size $m \times (n + m)$. With these relationships, following the general equation for effective kinetic energy of impact outlined in Chapter 3, Eq. (3.27), the expressions for the effective kinetic energy of impact for the independent coordinates are then expressed as:

$$T_c = \frac{1}{2} \boldsymbol{\pi}^T \mathbf{J}_{ic}^T \left(\mathbf{J}_{ic} \mathbf{W}^{-1} \mathbf{J}_{ic}^T \right)^{-1} \mathbf{J}_{ic} \boldsymbol{\pi} \quad (\text{B.6})$$

Where \mathbf{W} is now the $n \times n$ mass matrix associated with the coordinates $\boldsymbol{\pi}$. For the same system parametrized with the dependent coordinates the expression becomes:

$$T_c = \frac{1}{2} \dot{\mathbf{q}}^T \begin{bmatrix} \mathbf{\Gamma}^T & \mathbf{J}_c^T \end{bmatrix} \left(\begin{bmatrix} \mathbf{\Gamma} \\ \mathbf{J}_c \end{bmatrix} \mathbf{M}^{-1} \begin{bmatrix} \mathbf{\Gamma}^T & \mathbf{J}_c^T \end{bmatrix} \right)^{-1} \begin{bmatrix} \mathbf{\Gamma} \\ \mathbf{J}_c \end{bmatrix} \dot{\mathbf{q}} \quad (\text{B.7})$$

In this case \mathbf{M} is a $(n + m) \times (n + m)$ mass matrix associated with the dependent coordinates. We would like to show that Eq.(B.6) and Eq.(B.7) are equivalent in the case that Eq. (B.5) is true, and will give the same value for T_c . Considering Eqs.(B.3) and (B.5), Eq.(B.7) can be expressed as:

$$T_c = \frac{1}{2} \begin{bmatrix} \mathbf{0}_{1 \times m} & \mathbf{v}_c \end{bmatrix} \underbrace{\left(\begin{bmatrix} \mathbf{\Gamma} \\ \mathbf{J}_{dc} \end{bmatrix} \mathbf{M}^{-1} \begin{bmatrix} \mathbf{\Gamma}^T & \mathbf{J}_{dc}^T \end{bmatrix} \right)^{-1}}_{\mathbf{X}} \begin{bmatrix} \mathbf{0}_{1 \times m} \\ \mathbf{v}_c \end{bmatrix} \quad (\text{B.8})$$

where \mathbf{X} is the effective mass associated with the constrained coordinates using Eq. (B.7). If \mathbf{X} is broken down such that:

$$\mathbf{X} = \begin{bmatrix} (\mathbf{X}_a)_{m \times m} & (\mathbf{X}_b)_{m \times r} \\ (\mathbf{X}_c)_{r \times m} & (\mathbf{X}_d)_{r \times r} \end{bmatrix} \quad (\text{B.9})$$

then Eq. (B.8) reduces to:

$$T_c = \frac{1}{2} \mathbf{v}_c^T \mathbf{X}_d \mathbf{v}_c \quad (\text{B.10})$$

Expanding \mathbf{X} to get \mathbf{X}_d gives:

$$\mathbf{X} = \left(\begin{bmatrix} \mathbf{\Gamma} \\ \mathbf{J}_{dc} \end{bmatrix} \mathbf{M}^{-1} \begin{bmatrix} \mathbf{\Gamma}^T & \mathbf{J}_{dc}^T \end{bmatrix} \right)^{-1} = \left(\begin{bmatrix} \mathbf{\Gamma} \mathbf{M}^{-1} \mathbf{\Gamma}^T & \mathbf{\Gamma} \mathbf{M}^{-1} \mathbf{J}_{dc}^T \\ \mathbf{J}_{dc} \mathbf{M}^{-1} \mathbf{\Gamma}^T & \mathbf{J}_{dc} \mathbf{M}^{-1} \mathbf{J}_{dc}^T \end{bmatrix} \right)^{-1} \quad (\text{B.11})$$

which using the formula for an inverse of a generic block matrix gives \mathbf{X}_d as:

$$\mathbf{X}_d = \left[\mathbf{J}_{dc} \mathbf{M}^{-1} \mathbf{J}_{dc}^T - \mathbf{J}_{dc} \mathbf{M}^{-1} \mathbf{\Gamma}^T (\mathbf{\Gamma} \mathbf{M}^{-1} \mathbf{\Gamma}^T)^{-1} \mathbf{\Gamma} \mathbf{M}^{-1} \mathbf{J}_{dc}^T \right]^{-1} \quad (\text{B.12})$$

Substituting Eq. (B.12) back into Eq. (B.10) gives:

$$T_c = \frac{1}{2} v_c^T \left[\mathbf{J}_{dc} \mathbf{M}^{-1} \mathbf{J}_{dc}^T - \mathbf{J}_{dc} \mathbf{M}^{-1} \mathbf{\Gamma}^T (\mathbf{\Gamma} \mathbf{M}^{-1} \mathbf{\Gamma}^T)^{-1} \mathbf{\Gamma} \mathbf{M}^{-1} \mathbf{J}_{dc}^T \right]^{-1} v_c \quad (\text{B.13})$$

One final substitution of Eq. (B.4), $\mathbf{J}_{dc} = \mathbf{J}_{ic} \mathbf{B}$ into Eq. (B.13), and factoring out \mathbf{J}_{ic} gives:

$$T_c = \frac{1}{2} v_c^T \left[\mathbf{J}_{ic} (\mathbf{B} \mathbf{M}^{-1} \mathbf{B}^T - \mathbf{B} \mathbf{M}^{-1} \mathbf{\Gamma}^T (\mathbf{\Gamma} \mathbf{M}^{-1} \mathbf{\Gamma}^T)^{-1} \mathbf{\Gamma} \mathbf{M}^{-1} \mathbf{B}^T) \mathbf{J}_{ic}^T \right]^{-1} v_c \quad (\text{B.14})$$

Referring now to independent coordinates, for the purposes of comparing them to the dependent coordinates $\dot{\mathbf{q}}$ which are of different dimension, let an intermediate set of coordinates $\hat{\boldsymbol{\pi}}$ be considered, where $\hat{\boldsymbol{\pi}}$ is just the space parametrized by $\boldsymbol{\pi}$ embedded into a space of the same dimension as $\dot{\mathbf{q}}$ which is an $(n + m) \times 1$ space. This gives:

$$\hat{\boldsymbol{\pi}} = \begin{bmatrix} \mathbf{0}_{m \times 1} \\ \boldsymbol{\pi} \end{bmatrix} \quad (\text{B.15})$$

Since the total kinetic energy of the system will remain the same regardless of the parametrization used, the total kinetic energy associated with the system parametrized by $\boldsymbol{\pi}$ will be equal to the total kinetic energy associated with the system parametrized by $\hat{\boldsymbol{\pi}}$. That is to say:

$$T = \frac{1}{2} \boldsymbol{\pi}^T \mathbf{W} \boldsymbol{\pi} = \frac{1}{2} \hat{\boldsymbol{\pi}}^T \hat{\mathbf{W}} \hat{\boldsymbol{\pi}} = \frac{1}{2} \begin{bmatrix} \mathbf{0} & \boldsymbol{\pi}^T \end{bmatrix} \hat{\mathbf{W}} \begin{bmatrix} \mathbf{0} \\ \boldsymbol{\pi} \end{bmatrix} \quad (\text{B.16})$$

where $\hat{\mathbf{W}}$ is now the generalized mass matrix associated with $\hat{\boldsymbol{\pi}}$. As with Eq. (B.9), we symbolically expand $\hat{\mathbf{W}}$ to give:

$$\hat{\mathbf{W}} = \begin{bmatrix} \hat{\mathbf{W}}_{a(m \times m)} & \hat{\mathbf{W}}_{b(m \times n)} \\ \hat{\mathbf{W}}_{c(n \times m)} & \hat{\mathbf{W}}_{d(n \times n)} \end{bmatrix} \quad (\text{B.17})$$

Then the Eq.(B.16) can be rewritten as:

$$\frac{1}{2} \boldsymbol{\pi}^T \mathbf{W} \boldsymbol{\pi} = \frac{1}{2} \begin{bmatrix} \mathbf{0} & \boldsymbol{\pi}^T \end{bmatrix} \hat{\mathbf{W}} \begin{bmatrix} \mathbf{0} \\ \boldsymbol{\pi} \end{bmatrix} = \frac{1}{2} \boldsymbol{\pi}^T \hat{\mathbf{W}}_d \boldsymbol{\pi} \quad (\text{B.18})$$

Since $\boldsymbol{\pi}$ are a set of independent coordinates, the mass matrix \mathbf{W} is unique which means that:

$$\mathbf{W} = \hat{\mathbf{W}}_d \quad (\text{B.19})$$

To determine $\hat{\mathbf{W}}$ we can use Eqn.s (B.1) and (B.5) to give the relationship between $\dot{\mathbf{q}}$ and $\hat{\boldsymbol{\pi}}$.

$$\begin{bmatrix} \boldsymbol{\Gamma} \\ \mathbf{B} \end{bmatrix} \dot{\mathbf{q}} = \begin{bmatrix} \mathbf{0}_{m \times 1} \\ \boldsymbol{\pi} \end{bmatrix} = \hat{\boldsymbol{\pi}} \quad (\text{B.20})$$

Let the matrix $\begin{bmatrix} \boldsymbol{\Gamma}^T & \mathbf{B}^T \end{bmatrix}^T$ be referred to as \mathbf{G} . Then from the fundamental variational equation at the velocity level of \mathbf{q} :

$$\delta \dot{\mathbf{q}}^T (\mathbf{M} \dot{\mathbf{q}} + \mathbf{c} - \mathbf{f}) = 0 \quad (\text{B.21})$$

The term $\delta \dot{\mathbf{q}}^T$ can be replaced with $\delta \hat{\boldsymbol{\pi}}^T \mathbf{G}^{-T}$ giving:

$$\delta \hat{\boldsymbol{\pi}}^T \mathbf{G}^{-T} (\mathbf{M} \mathbf{G}^{-1} \dot{\hat{\boldsymbol{\pi}}} + \dot{\mathbf{G}}^{-1} \hat{\boldsymbol{\pi}} + \mathbf{c} - \mathbf{f}) = 0 \quad (\text{B.22})$$

$$\underbrace{\mathbf{G}^{-T} \mathbf{M} \mathbf{G}^{-1}}_{\hat{\mathbf{W}}} \dot{\hat{\boldsymbol{\pi}}} + \underbrace{\mathbf{G}^{-T} \dot{\mathbf{M}} \mathbf{G}^{-1}}_{\dot{\hat{\mathbf{W}}}} \hat{\boldsymbol{\pi}} + \underbrace{\mathbf{G}^{-T} \mathbf{c} - \mathbf{G}^{-T} \mathbf{f}}_{\hat{\boldsymbol{\tau}}} = 0 \quad (\text{B.23})$$

which gives $\hat{\mathbf{W}}$ as:

$$\hat{\mathbf{W}} = \mathbf{G}^{-T} \mathbf{M} \mathbf{G}^{-1} = \begin{bmatrix} \boldsymbol{\Gamma} \\ \mathbf{B} \end{bmatrix}^{-T} \mathbf{M} \begin{bmatrix} \boldsymbol{\Gamma} \\ \mathbf{B} \end{bmatrix}^{-1} = \left(\begin{bmatrix} \boldsymbol{\Gamma} \\ \mathbf{B} \end{bmatrix} \mathbf{M}^{-1} \begin{bmatrix} \boldsymbol{\Gamma}^T & \mathbf{B}^T \end{bmatrix} \right)^{-1} \quad (\text{B.24})$$

$$\hat{\mathbf{W}} = \begin{bmatrix} \boldsymbol{\Gamma} \mathbf{M}^{-1} \boldsymbol{\Gamma}^T & \boldsymbol{\Gamma} \mathbf{M}^{-1} \mathbf{B}^T \\ \mathbf{B} \mathbf{M}^{-1} \boldsymbol{\Gamma}^T & \mathbf{B} \mathbf{M}^{-1} \mathbf{B}^T \end{bmatrix}^{-1} \quad (\text{B.25})$$

Referring back to Eq. (B.17), $\hat{\mathbf{W}}_d$ can now be developed from Eq. (??) using the formula for the inverse of a generic block matrix, to be :

$$\hat{\mathbf{W}}_d = [\mathbf{B}\mathbf{M}^{-1}\mathbf{B}^T - \mathbf{B}\mathbf{M}^{-1}\mathbf{\Gamma}^T(\mathbf{\Gamma}\mathbf{M}^{-1}\mathbf{\Gamma}^T)^{-1}\mathbf{\Gamma}\mathbf{M}^{-1}\mathbf{B}^T]^{-1} \quad (\text{B.26})$$

It can be seen now that the inverse of the right-hand side of Eq. (B.26) is the term in round brackets in Eq. (B.14). Subbing in $\hat{\mathbf{W}}_d$ for the equivalent term in Eq. (B.14), this gives the effective kinetic energy using the dependent coordinates as:

$$T_c = \frac{1}{2}v_c^T(\mathbf{J}_{ic}\hat{\mathbf{W}}_d^{-1}\mathbf{J}_{ic}^T)^{-1}v_c \quad (\text{B.27})$$

which considering from Eq. (B.19) that $\mathbf{W} = \hat{\mathbf{W}}_d$, this gives:

$$T_c = \frac{1}{2}v_c^T(\mathbf{J}_{ic}\mathbf{W}^{-1}\mathbf{J}_{ic}^T)^{-1}v_c \quad (\text{B.28})$$

which is the equation given for effective kinetic energy computed with independent coordinates in Eq. (B.6). Thus T_c can be evaluated using an equation of the form Eq (B.6) when a set of independent coordinates are used to parametrize the system, or an equation of the form Eq. (B.7) when a set of dependent coordinates are used to parametrize the system, as long as Eq. (B.5) holds true.

APPENDIX C
CAD Drawings and Force Calculations for Experimental Equipment

C.1 Proposed Modifications for Mounting the RCP Redundant Actuators

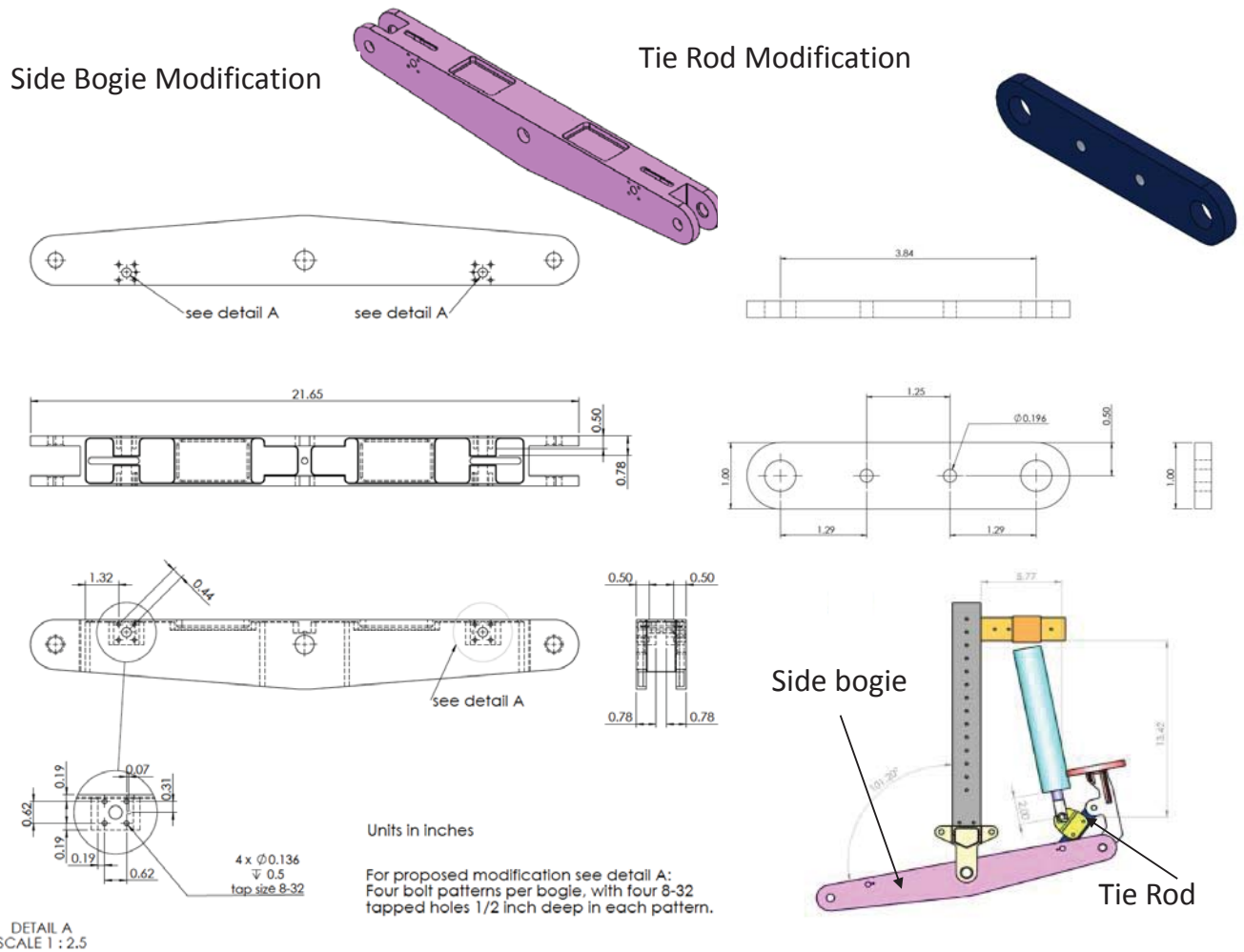


Figure C–1: Two sets of proposed modifications to the RCP side bogies and tie rods, to accommodate the attachment of the redundant actuators.

C.2 Force Analysis of Rear Mounted Sensors

For analysis of the distribution of forces throughout the obstacle to determine how well a rear mounting location will accommodate impact sensors, the impact force is modelled as a static,

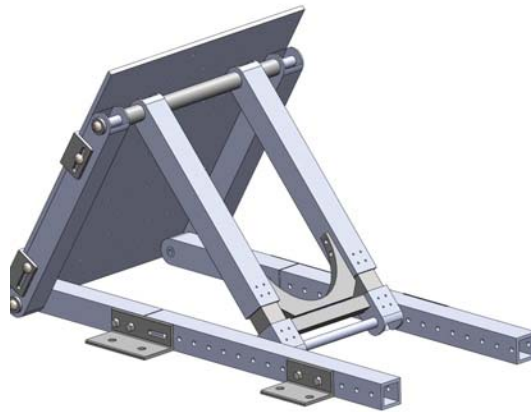


Figure C-2: Obstacle with rear mounted sensors.

constant force and the equations of static equilibrium are developed. For the purpose of simplifying

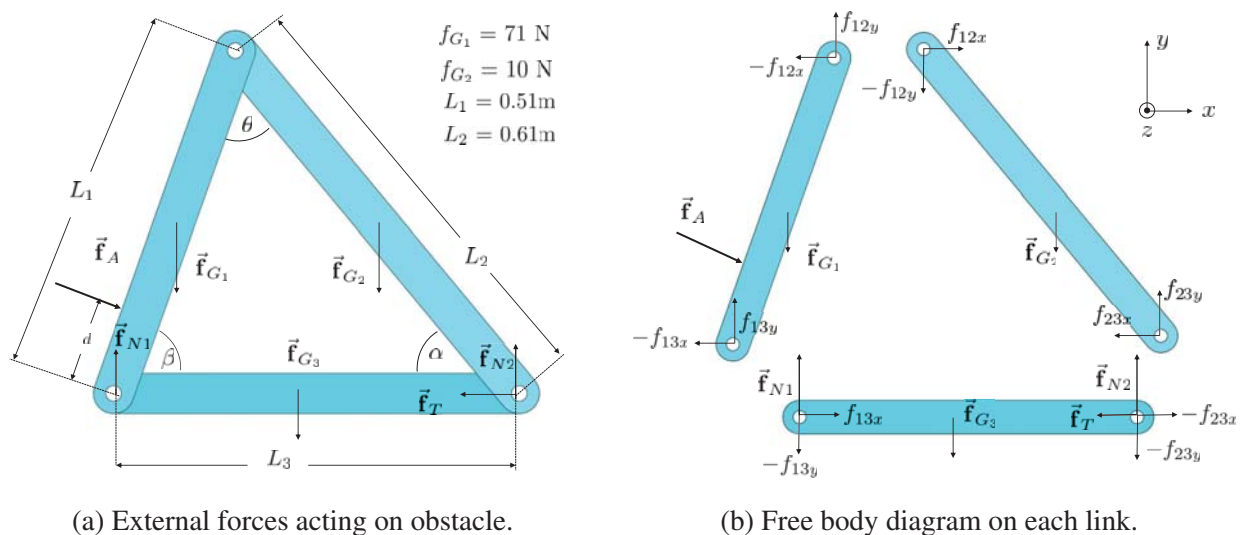


Figure C-3

the analysis, each side of the obstacle is modelled as the same three-link rigid body with the applied force \vec{f}_A representing half of the impact load applied by the rover. The front facing link represents one of the front frame links of the obstacle and half of the impact plate that rests on top. The rear link is aluminum tube that has been modified to allow for rear mounting of the sensors as shown in Fig. C-2. The bottom link, a steel member, alters in length with the angle of impact β along with angles θ and α . Table C-1 gives values for these parameters corresponding to the range of impact angles for the experiments. In table C-1, the value d , which also depends on the angle

Table C-1: Values shown in Fig. C-3 which alter with the impact angle.

β	α	θ	L_3	d
40°	32°	107°	0.91 m	0.041m
50°	39°	90°	0.79 m	0.062m
60°	46°	74°	0.67 m	0.086m
70°	51°	59°	0.55 m	0.115m
80°	55°	45°	0.44 m	0.144m
90°	56°	34°	0.34 m	0.175m

of impact, relates to the contact point between the rover wheels and the impact plane, which is the application point for the impact force. The resulting forces all act within the $x - y$ plane. In Fig C-3a the external forces acting on the obstacle are shown. The symbols \vec{f}_A , \vec{f}_G , \vec{f}_F , \vec{f}_N , represent the geometric vectors of applied, gravitational, frictional, and normal forces respectively. Their magnitudes are represented by f_A , f_G , f_F and f_N . Fig. C-3b illustrates the free body diagram of the three links composing the obstacle. The values f_{ijx} and f_{ijy} represent the x and y scalar components of the internal forces developed in the obstacle as a result of the external forces, where i and j, having values from 1 to 3, are the indices of the corresponding link. The equations of static equilibrium for each link are:

$$\begin{aligned}
 \Sigma \mathbf{f}_x & & \Sigma \mathbf{f}_y \\
 f_A \sin \beta - f_{12x} - f_{13x} &= 0 & f_{12y} + f_{13y} - f_A \cos \beta - f_G = 0 \\
 f_{12x} - f_{23x} &= 0 & f_{23y} - f_{12y} = 0 \\
 f_{13x} + f_{23x} - f_t &= 0 & f_{N1} + f_{N2} - f_{13y} - f_{23y} - f_G = 0 \\
 \Sigma \mathbf{M}_z & & \\
 f_{12x} L_1 \sin \beta + f_{12y} L_1 \cos \beta - f_A \frac{L_1}{a} - f_G \frac{L_1}{2} \cos \beta &= 0 \\
 f_{12y} L_2 \cos \alpha + f_G \frac{L_2}{2} \cos \alpha - f_{12x} L_2 \sin \alpha & \\
 f_{N2} L_3 - f_{12y} L_3 - f_G \frac{L_3}{2} &= 0
 \end{aligned} \tag{C.1}$$

The magnitude, f_c , of the force that would be applied in the rear located sensor would correspond to the compression of link two, which can be evaluated as:

$$f_c = f_{23x} \cos \alpha + f_{23y} \sin \alpha \tag{C.2}$$

The value for this compressive force depends on the angle β of the impact plane. For the range of β from 40° to 90° , the resulting compression in the rear link ranges between $0.079 f_a$ and $0.74 f_a$ plus an angle dependent constant due to the weight of the linkage. Hence for lower angles, the rear mounted sensors will read only a small fraction of the total applied force, and so information about the differences between impact force as the angle shifts will be small, and in some cases below sensor resolution. The design of the obstacle could be altered to better accommodate this mounting, with an increase of dimension d with respect to L_1 for example, or potentially also mounting of the sensors in the bottom link would improve the capture of force information. Such designs are left for future work.

C.3 Intelligent Obstacle Design and Future Use

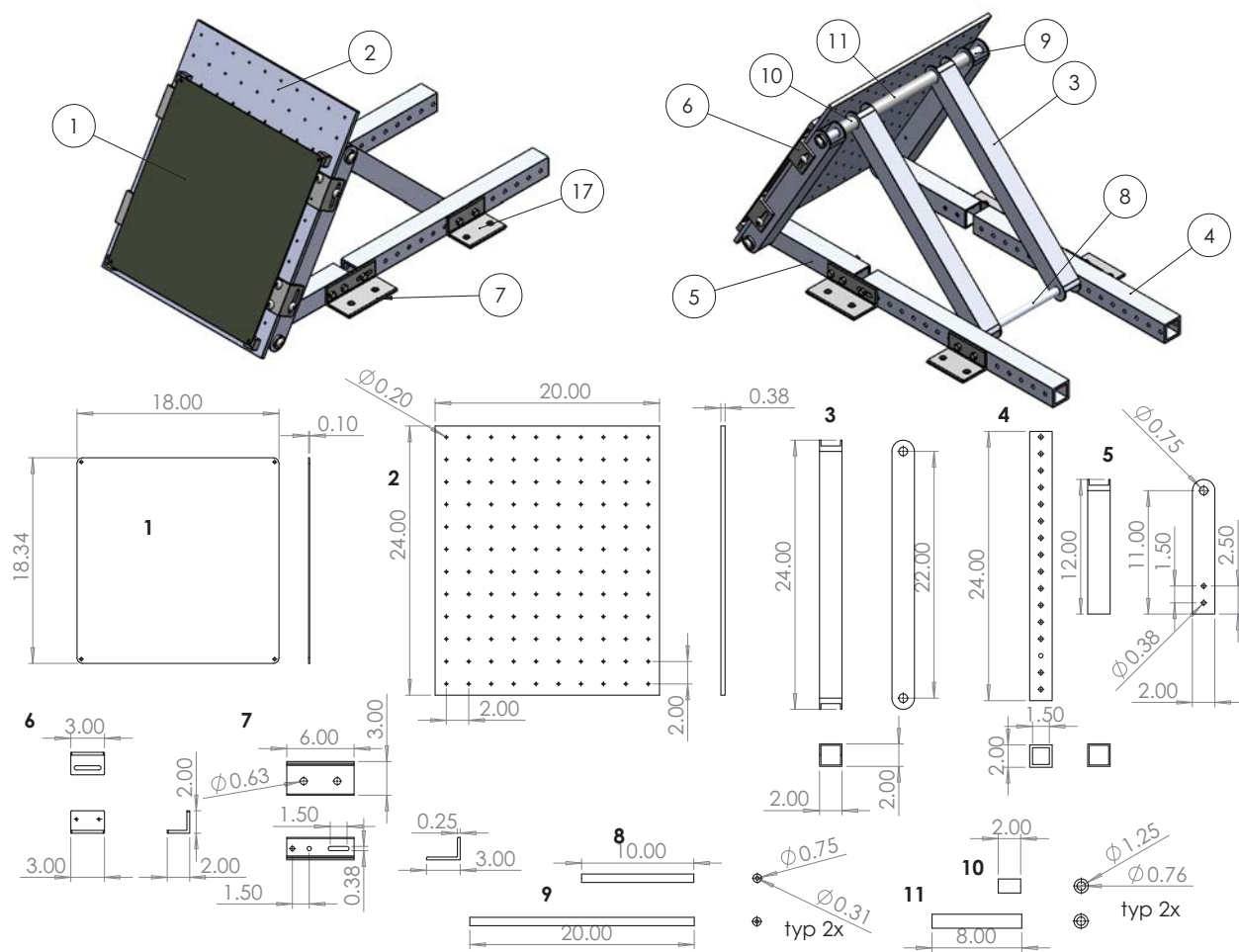


Figure C-4: Intelligent Obstacle CAD drawings

Horizontal and
step down configurations

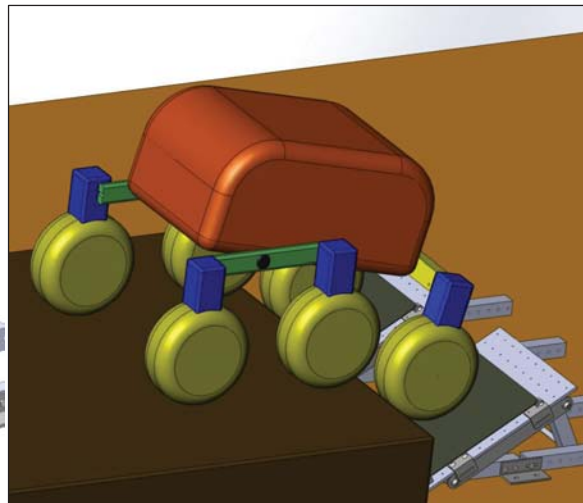
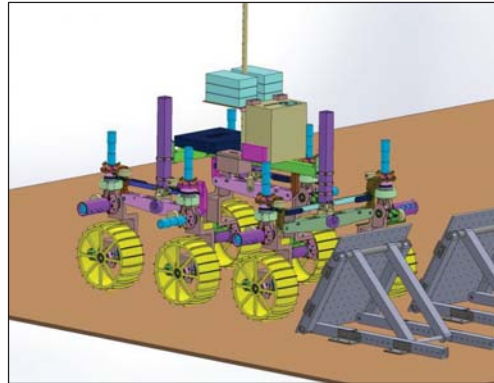
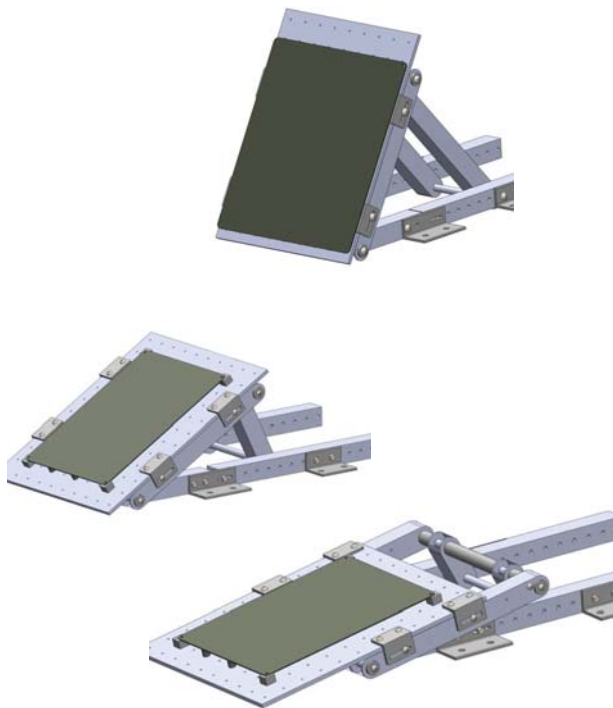


Figure C-5: Possible intelligent obstacle configurations for future analysis: horizontal and step down.

Slope climbing with compound
Obstacle assembly

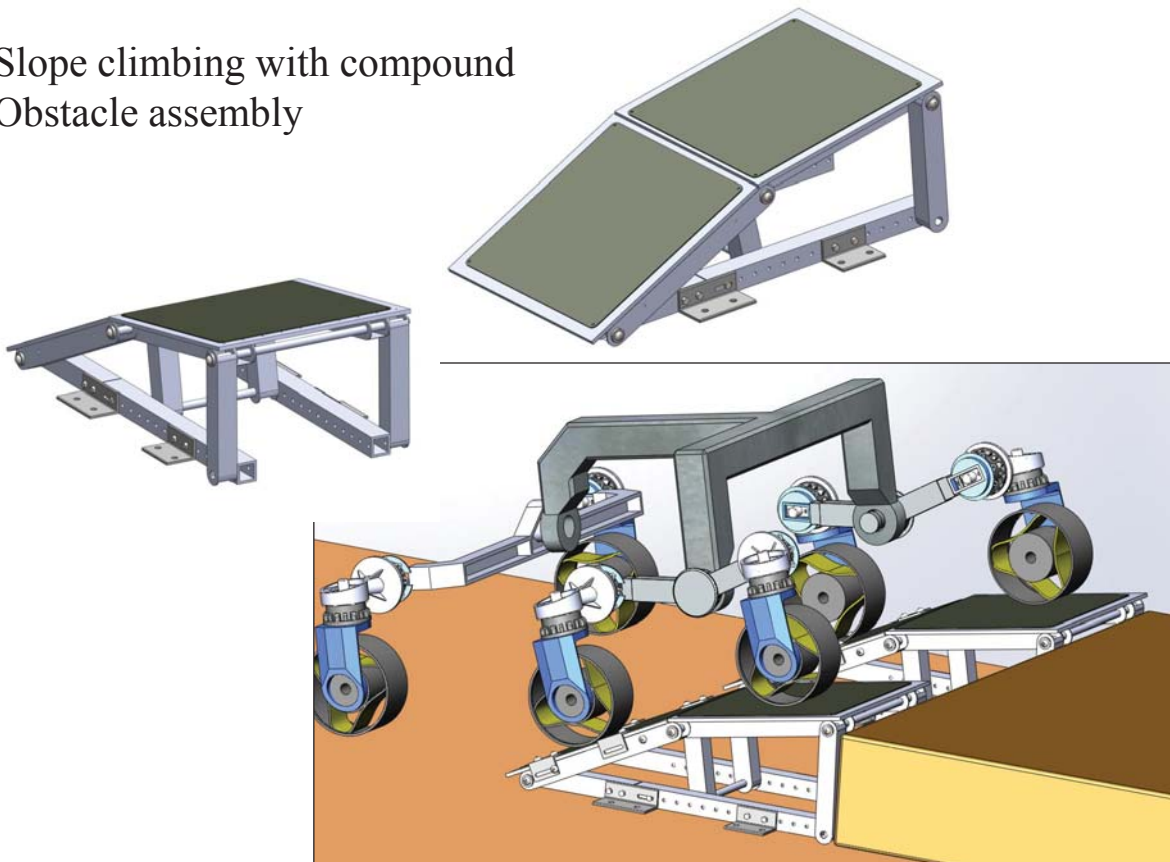


Figure C-6: Possible intelligent obstacle configurations for future analysis: climbing.

APPENDIX D

Impact Experiments with an RCP bumper

D.1 Construction of the Bumper

To remove the effect of the grousers from the experimental data, an obvious solution was to replace the wheels on the RCP with smooth ones. This however was not an option, as no such smooth wheels were available or easily manufactured. Alternative treatment of the wheels such as wrapping them, or filling in the gaps between the grousers to effectively enlarge the wheel radius to the grouser radius was a possibility. The logistics of these tasks however posed some problems. Wrapping the wheels in a soft tape would create discontinuities in the density of the wheels where the tape would compress over grousers and fall loosely in the gaps in between. Filling in the gaps between grousers with a molded attachment was an option, but moldmaking of the wheel would require the removal of a wheel to a molding work station for the purposes of making a principle mold, which was not a desirable option. Epoxies or spray foam could have been applied to the wheels in between the grousers, but the ability to fully remove these substances and return the wheels to their original state after the experiments were finished, was in question. Finally, options involving CNC or 3-D printing were beyond the budget of the second round of experiments. As an alternative to these possibilities, a mechanical attachment resembling an individual bumper on



Figure D-1: CAD model of bumper assembled on RCP wheel

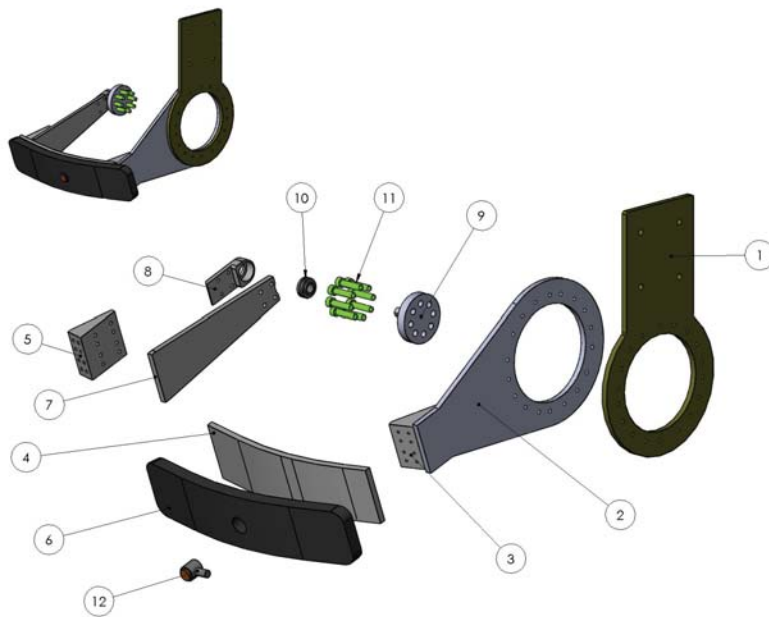


Figure D-2: Exploded view and part list of bumper model

each wheel was proposed. The bumper bolted onto the leg of the rover on the inner side of each of

Table D-1: List of parts displayed in Fig. D-2.

#	Part Description	#	Part Description
1)	RCP leg bolt plate	2)	inner bolt plate
3)	inner corner bracket	4)	bumper face
5)	outer corner bracket	6)	bumper foam
7)	bumper arm	8)	bearing tab
9)	outer wheel face bolt plate	10)	spherical bearing
11)	25mm M6 bolts	12)	PCB impact sensor

the front wheels, and attached to the outside of each wheel making use of a pre-existing bolt hole pattern for bolting the wheel hub to the harmonic drive housed inside the wheel. This attachment would naturally require the use of a bearing to separate the rotating wheel surface from the static connecting arm of the bumper. Figs. D-1 and D-2 show the solid model of the bumper attached to the RCP wheel, and the exploded view of the bumpers component parts that are listed in Table D-1. An issue with the bearings on each of the two bumpers was that each one had to withstand the expected impact load of a maximum of about 300 N with a safety factor of three to meet the

requirements of MDA engineers. Static and dynamics load ratings of this degree were too high for an initially chosen stream lined needle roller bearing which has a low profile so as not to interfere with the assembly of the machine screws distributed about the bearing perimeter. More robust deep groove ball bearings however were typically too large in diameter to fit within in the required space. Also their slender width would not withstand any moment about the wheel caused by the bloating of the bumper arms due to pressure on the curved bumper surface. Consequently, spherical roller bearings which came in low profiles, with high static and dynamic load ratings and would allow for some movement about the radial axis of the wheel. This extra degree of freedom in the bearing proved to be an asset in the assembly of the bumper at MDA where matching hole patterns for bolting purposes was tricky with the curved surface of the bumper face.

D.2 Experimental Set-up

Other factors to improve upon in this round of the experiments were 1) the noise vibration of the apparatus, 2) the error due to operator reflex 3) the confusion due to sensor location. The first of these would be alleviated to some degree with the application of two sheets of ultra high molecular weight polyethylene displayed in the top left corner of Fig. D-3 (UHMW) that was placed on each of the obstacle impact surfaces. This material was chosen for its resistance to impact and abrasion, and very low coefficient of friction. The Operator error as previously discussed produced a time delay between the impact of the of the RCP and the cutting of power to its wheels giving a variation in the impact force based purely on this delay. Ideally connecting the impact sensors to the rover power would be the correct solution, but this type of interaction with the RCP software was not available. The solution was to drive the rover with its control interface (instead of with the joystick), which permit the exact power to each wheel to be specified for a given duration. Thus at the beginning of each impact the rover started at the same position and was powered for the same time duration for each experiment. This added some consistency to the results. Finally the location of the sensors in the set-up was on the bumper itself. Each bumper could be adjusted to angles from 90° to 40° so that its front face matched the angle of the obstacle. One sensor was then mounted on the front face of each bumper with a small rubber washer in between to again

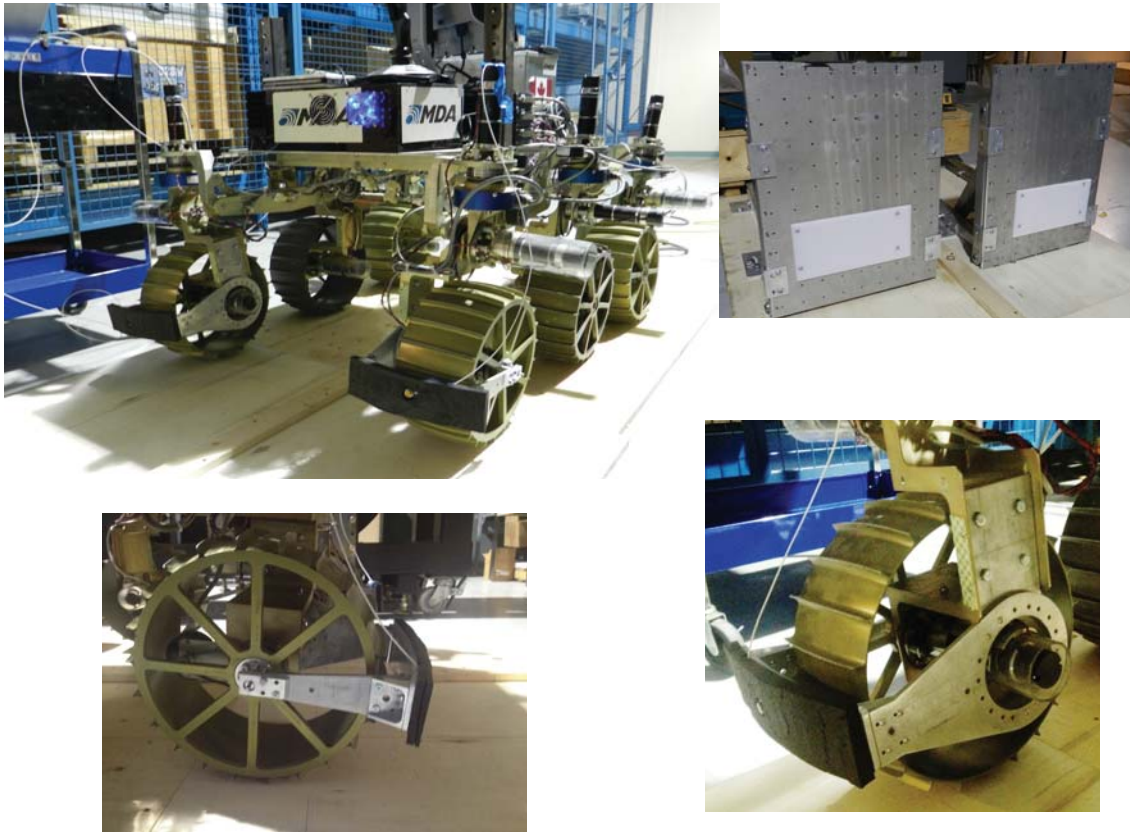


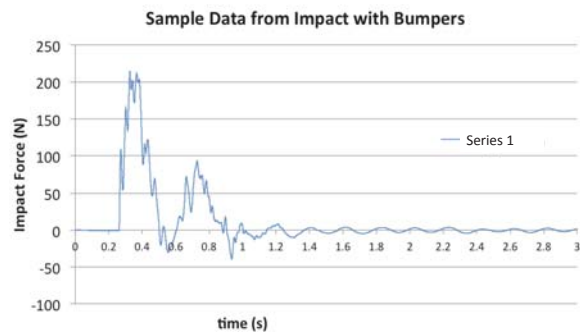
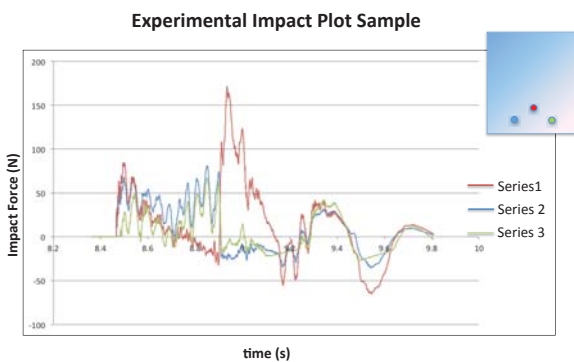
Figure D-3: Photographs of the bumpers constructed and assembled on the RCP wheel.

assist with vibration. A layer of dense impact foam was placed over the sensors to protect from side loading and to shield the stem. Consequently, impact on both front wheels of the rover would be recorded this time gathering all the necessary information available in a simple manner. The method of simply adding the signals to find the over all maximum of the total impact was now clearly the correct way to go about determining the maximum impact from the data. Each sensor was capable of recording up to 440 N. So in the event that one side of the rover took the full impact, the expected value was still within the range of the sensor.

D.3 Experimental Results

Data from the experimental results was similar to that of the initial set of hard and soft soil impact experiments discussed in Chapter 6. There were two main differences however, that made the second set of data much easier to analyze. The first difference was that instead of three data

series from three different sensors recording information about the impact on one side of the RCP, in the second set of data, there was only one sensor for impact on each side of the RCP. This cleared up any confusion about how to add the signals together, especially since the signals were sensitive to the location of the impact. For the second set of data, the sensor reading was not nearly so sensitive to this due to the fact that the sensor was mounted on the bumper rather than on the obstacle. The second difference was that out of that one data series, while the data did involve multiple peaks, these peaks were caused by aftershocks from the impact, and diminished steadily after the first impact. This meant the the first peak was in most cases the maximum peak, and the maximum impact force. This is unlike the data produced from the first set of experiments, where the multiple peaks were the result of multiple grouser impacts throughout the experimental setup, and all contributed to the maximum impact force in a complex manner. Vibration in both sets of data is still prevalent but reduced in the second set of data. Finally another asset to the data produced in the second set of experiments is that impact from both sides of the RCP were recorded, and so much more information about the impact has been recorded.



(a) Sample experimental data of RCP impact: first set of experiments. (b) Sample experimental data of RCP impact: second set of experiments.